



# The controlling factors and prediction model of pore structure in global shale sediments based on random forest machine learning

Fujie Jiang<sup>a,b,\*</sup>, Lina Huo<sup>a,b</sup>, Di Chen<sup>a,b</sup>, Liu Cao<sup>a,b</sup>, Renjie Zhao<sup>a,b</sup>, Yuan Li<sup>a,b</sup>, Tingwei Guo<sup>a,b</sup>

<sup>a</sup> State Key Laboratory of Petroleum Resources and Prospecting, China University of Petroleum, Beijing 102249, China

<sup>b</sup> College of Geosciences, China University of Petroleum, Beijing 102249, China

## ARTICLE INFO

### Keywords:

Shale oil/gas  
Shale sediments  
Shale pore structure  
Random forest machine learning  
Prediction model

## ABSTRACT

The rapid development of shale oil and gas promotes the plentiful research and characterization of micro-nano pore structure, and accumulates massive data, which is vital for fluid flow and storage. Although many interpretations based on various experimental methods and numerous shale specimens have been published, rare relatively complete compilation of shale pore structure has yet been made. Here, we report a new compilation of shale pore structure, comprising >350 marine, marine-terrestrial transitional and continental shale specimens of nearly all key formations and ages, of which collected samples were screened for effective analysis. This systematic review shows that shale sediments with different geological characteristics have obvious heterogeneity, multifarious micro-nano pores and complex pore size distribution (PSD). The shale PSD is divided into six types based on the morphological characteristics, and the compositions and thermal maturity of different PSD types of shale show obvious differences. Random forest (RF) machine learning (ML) further reveals that thermal maturity has the greatest effect on PSD classification, followed by organic matter (OM) abundance and mineral composition.

Thermal maturation affects pore type and PSD. The high thermal maturation facilitates organic pores generation and micro-nano micropores connection. Additionally, the diagenesis related to thermal maturation will also affect the pore types, especially the organic acids formed during hydrocarbon generation, which will promote dissolution pores. OM and mineral affect the pore shape and type. OM abundance has positive and negative effects on the shale pore structure. The high OM abundance avails to the formation of more micro-nano micropores. However, the strong plasticity of OM will cause pore space collapse. Mineral composition mainly affects the pore structure via pore type. Quartz and feldspar mainly develop intergranular pores with a few fractures. Carbonate minerals are mainly dominated by dissolution pores. Interlayer pores are frequently formed in clay minerals. Based on the evaluation from RF ML, we suggest that the sedimentary environment and OM type have little influence on shale pore structure.

A model based on RF ML is proposed to predict the PSD type of shale sediments from geological features. This model provides effective prediction for the six types of shale PSD. The limitation of valid data and the difference in data set size among different shale types constrain the accuracy of the prediction model. Supplementation of data and improvement of the RF model optimization algorithm in further studies will beneficially enhance the model accuracy. This study is a bold attempt, and provides a new time-saving and cost-saving method for the rapid prediction of shale pore structure based on geological analysis and ML. This work is instructive for understanding pore structure in shale sediments from basic geological information, and is valuable for further conserving resources and improving research efficiency.

## 1. Introduction

The pore structure greatly affects the properties and percolation capacity of oil and gas in shale reservoirs (Lai et al., 2018; Zheng et al.,

2018; Nikolaev and Kazak, 2019; Hu et al., 2021b). Therefore, the evaluation of the pore structure of unconventional oil and gas reservoirs has been a focus of the petroleum industry in recent years (Cnudde and Boone, 2013; Li et al., 2015; Lai et al., 2018; Chandra and Vishal, 2021).

\* Corresponding author at: State Key Laboratory of Petroleum Resources and Prospecting, China University of Petroleum, Beijing 102249, China.

E-mail address: [jfjhtb@163.com](mailto:jfjhtb@163.com) (F. Jiang).

<https://doi.org/10.1016/j.earscirev.2023.104442>

Received 21 January 2023; Received in revised form 28 April 2023; Accepted 1 May 2023

Available online 4 May 2023

0012-8252/© 2023 Elsevier B.V. All rights reserved.

The in-depth exploration of unconventional oil and gas resources within smaller pore spaces facilitates scientific research on the micro and nano meter scale. Currently, considerable amount of work has been performed on various shale sediments with various expensive experimental techniques, and plentiful understanding of the micro-nano pore structure has been obtained (Clarkson et al., 2013; Hosseini et al., 2021; Wang et al., 2021b). The results show that the pore structure in shale sediments is closely related to geological conditions (Yang et al., 2021), while the relations lack systematic sorting and summary currently. It is meaningful to summarize and sort out the relationship between shale pore structure and geological features including lithofacies, organic geochemical features, composition, etc., and to establish a corresponding geological evaluation and prediction model of shale pore structure.

The shale pore structure presents a complex and polytype micro-nano pore system, with the pore-throat diameters  $<1\ \mu\text{m}$  (Zou et al., 2012; Clarkson et al., 2013). The pore size distribution (PSD) varies in different sedimentary settings (Zou et al., 2012; Zhu et al., 2013). The main pore size in tight sandstone reservoirs mainly ranges from 40 to 700 nm, and that in tight limestone reservoirs generally ranges from 40 to 500 nm (Chilingar et al., 1972; Skalinski et al., 2013). Comparatively, shale contains smaller pore system with a PSD of mainly 30–400 nm in shale oil reservoirs and 5–200 nm in shale gas reservoirs (Fig. 1) (Zou et al., 2012). These pore structures have been characterized by various methods with different principles and applicable scopes, including image analysis technology, fluid injection and non-fluid injection method (Fig. 1) (Anovitz and Cole, 2015).

Image analysis technology can qualitatively observe the pore shape and particle contact, and pore size and PSD can be obtained through image analysis techniques. Image analysis techniques include electron microscope, transmission electron microscope (TEM), scanning electron microscope (SEM), atomic force microscope (AFM) and other micro-area observation techniques (Chandra and Vishal, 2021; Wang et al., 2021b; Liu et al., 2022). The advantage of these methods is that it can be intuitively characterized in terms of pore morphology and genesis research. However, the pure qualitative research of imaging can no

longer meet the needs of dense micro-nano materials, and quantitative characterization is further needed to study the micro-nano pore structure.

Fluid injection and non-fluid injection methods can realize quantitative analysis of pore structure (Anovitz and Cole, 2015). The fluid injection methods, e.g., mercury injection and gas isothermal adsorption etc., use non-wetting fluids such as mercury, nitrogen ( $\text{N}_2$ ), carbon dioxide ( $\text{CO}_2$ ) and methane ( $\text{CH}_4$ ) to inject samples under different pressures. Then, the PSD, specific surface area (SSA), pore volume (PV) and other information can be obtained by various theoretical models (Thommes, 2004; Thommes et al., 2012a). Currently, non-fluid injection methods are also ubiquitous, including small-angle and ultra-small-angle scattering techniques (SAS and USAS), computed tomography (CT) techniques, and so on. These methods have their own advantages and limitations, and it is difficult to fully reveal pore structure by using only a single method (Zhang et al., 2020a). The mercury injection method can obtain the pore porosity, PSD, and connectivity for majority rocks. However, the limitation of experimental pressure imposes restrictions on mercury entering nanoscale pores in dense shale sediments with low permeability. Therefore, mercury injection can generally accurately characterize the meso-macro pore space, and it needs to ally other technologies to characterize micro-nano pore system (Iqbal et al., 2021). The small angle X-ray Scattering (SAXS) technique is characterized by fast, non-destructive and simple sample pretreatment process (Cavelan et al., 2020; Hosseini et al., 2021). However, due to the scarcity of light sources at present, its application is not widespread. SAXS can provide more effective detect for mesopores, and it is not easy to realize the test on the full aperture. Nuclear magnetic resonance (NMR) is another widely used non-destructive technique to acquire the porosity and PSD characteristics of pore structure (Nikolaev and Kazak, 2019; Lawal et al., 2020). While, the widespread organic matter (OM) and its lipophilicity in the low-maturity shale restrict its interpretation for the hydrocarbon filling shale sediments. Three-dimensional (3D) reconstruction techniques, such as micro-nano CT, are burgeoning method to show the 3D pore space, and can also be used to analyze the number and

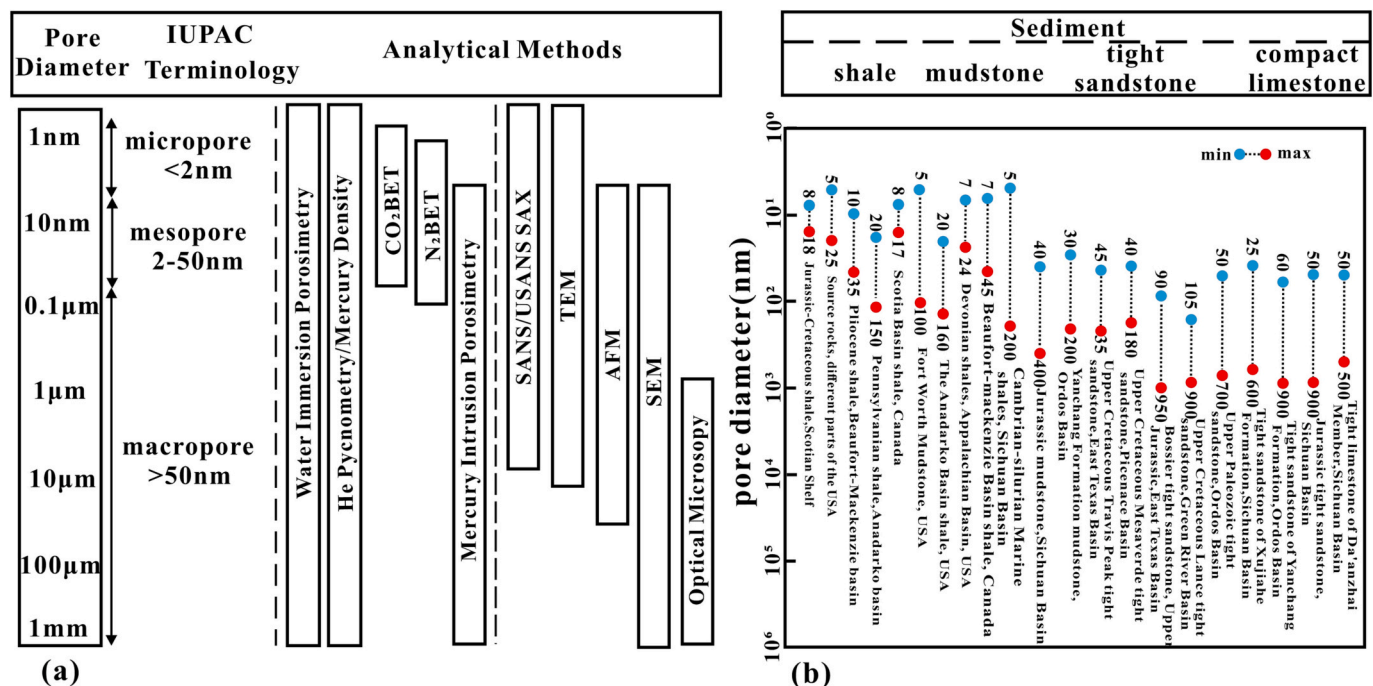


Fig. 1. (a) shows the common methods to characterize pore structure in rock. IUPAC is International Union of Pure and Applied Chemistry (Sing et al., 1985); BET is Brunauer–Emmett–Teller method; AFM presents atomic force microscope; (U)SANS is (ultra) small-angle X-ray scattering; SAXS presents small-angle neutron scattering; TEM is transmission electron microscope; SEM is scanning electron microscope. (b) presents the pore size distribution in different sediments (Zou et al., 2012; Anovitz and Cole, 2015).

connectivity of reservoir pore throats. It has been widely used for numerical simulation and characterization of carbonate rock, shale and tight sandstone reservoirs (Cnudde and Boone, 2013). Nonetheless, CT is an image recognition technology in essence, and its interpretation depends on the resolution and artificial operation, which also need verification by other tests. Therefore, it is necessary to improve the accuracy of instruments and the improvement of the data interpretation method in order to play a greater role in the study of the pore structure.

Although diversiform methods can be executed to the characterization of pore structure, the limitations are ubiquitous as: (1) It is difficult to achieve both accuracy and study scale (Clarkson et al., 2013; Anovitz and Cole, 2015). The current techniques have high resolution, but the higher the resolution, the smaller the scale. For shale sediments with strong heterogeneity, it is difficult to fully describe the entire pore structure through small-scale measurements only. Therefore, how to extend small-scale to full scale using various technologies needs to be considered. (2) Full-aperture joint characterization. Although there are different full-aperture joint characterization methods, they are mainly based on mechanical splicing of different experimental results, and contradictions often appear in the overlap (Zhang et al., 2020a). (3) The digital core image analysis technology is greatly influenced by man-made factors. For dense shale sediments with complex and irregular pore-throat characteristics, when relying on digital core technology for 3D reconstruction of pore structure, image processing and algorithm selection are largely influenced by human factors (Jiao et al., 2014b; Comerio et al., 2020).

The complex pore structure of shale deposits is the result of the comprehensive action of various geological factors (Yang et al., 2013; Pommer and Milliken, 2015; Li et al., 2016a; Zheng et al., 2018; Dong et al., 2019; Cavelan et al., 2020; Knapp et al., 2020; Gu et al., 2021; Liu et al., 2022; Wang et al., 2022c), and the main geological factors affecting the pore structure in shale sediments include sedimentary environment, mineral composition and organic geochemical features, like total organic carbon (TOC) content, kerogen type and thermal maturity. (1) The types of pore in different depositional environments are quite different. Marine shale has very well-developed organic pores, while continental shale and marine-continental transitional shale are dominated by pores related to inorganic minerals, and organic pores are relatively rare (Yang et al., 2013; Pommer and Milliken, 2015; Xue et al., 2020). (2) Mineral composition affects the pore structure of shale. First, it affects the inorganic pore type. Felsic minerals and clay minerals develop intergranular pores and intragranular pores, while carbonate minerals develop intercrystalline pores and intracrystalline pores, and the intergranular pores are generally larger. Dissolution pores usually exist in only some specific minerals. In general, shale with a high content of brittle minerals has strong compaction resistance and more easily preserves intergranular pores than clay-rich shale, but is prone to micro-cracks (Berger et al., 1997; Knapp et al., 2020). Second, the organic-inorganic interaction seriously affects the characteristics of the organic pore structure, which is mainly reflected in two aspects: On the one hand, the pores are reduced due to the filling of the mineral-related intergranular pores and intragranular pores by the OM particles, or the structural composite formed by the OM and the mineral affecting pores positively/negatively. On the other hand, clay minerals and inorganic minerals catalyze/inhibit the thermal evolution of OM, leading to a more complex evolution process of OM pores (Curtis et al., 2012a; Kennedy et al., 2014; Liu et al., 2022). (3) Kerogen type, TOC content and the process of thermal evolution affect the formation of organic pores and the development of inorganic pores (Milliken et al., 2013a; Pommer and Milliken, 2015; Li et al., 2016a; Zheng et al., 2018; Dong et al., 2019; Liu et al., 2022). Type I and II kerogens have higher hydrocarbon generation potential than type III kerogen, so they usually have a relatively higher potential to develop OM pores (Mao and Guo, 2018; Gu et al., 2021). When the degree of thermal evolution is low, the kerogen type and maceral play a leading role in the development of organic pores. When the degree of evolution reaches a certain level, OM

with high hydrocarbon generation potential will generate a large number of hydrocarbons, which will result in the formation of organic pores. As hydrocarbon generation proceeds, the pore structure will change. Due to strong compaction and diagenesis, the intergranular pores basically disappear in the middle stage of diagenesis. Moreover, when the hydrocarbon generation peak is reached, hydrocarbon expulsion will reduce the internal pressure of the organic pores, thereby affecting the evolution of the pore structure (Curtis et al., 2012a; Dong et al., 2019; Zhou et al., 2020b). Milliken et al. (2013a) believed that the TOC content has a more obvious control effect on OM pores than thermal maturity. Mao and Guo et al. (2018) demonstrated that for immature shale, the PSD is mainly affected by the degree of compaction. For over-mature shale, the PSD is mainly affected by the kerogen type and TOC content. In general, the evolution of the shale pore structure is controlled by various geological factors, and the effects of different factors are not independent. The PSD of shale affects its fluid mobility and storage capacity.

The PSD is the result of a combination of many geological factors. Thus, evaluating the shale PSD by a single factor may lead to one-sided conclusion. Likewise, it is also difficult to accurately describe the relationship between multiple geological factors and pore structure by using traditional analysis methods. At present, there is still a lack of multi-factor comprehensive evaluation methods for shale PSD. However, machine learning (ML) algorithms can establish a more complex and accurate mapping relationship between sample features and results, which provides a new method for relatively complex geological evaluation (Bangert et al., 2021; Sircar et al., 2021; Von Rueden et al., 2021; Ma et al., 2022). ML methods based on mathematical statistics have received increasing attention, and have been widely used in geology in recent years (Min et al., 2020; Ma et al., 2022), including Gaussian process regression (Rui et al., 2020), support vector machines (Tan et al., 2013), K-nearest neighbors (Handhal et al., 2020), gradient boosting (Ma et al., 2022), and random forest (RF) (Gordon et al., 2022) etc. RF algorithm is a popular ML method for developing regression or classification models in many research settings. It is a method of integrating many decision trees into a forest and using it to predict the final result. As a result, RF generally provides higher accuracy than single decision tree models, with high model interpretability (Speiser et al., 2015). In addition, the RF algorithm can handle high-dimensional data, has good generalization ability and anti-overfitting ability, and is very suitable for classification and regression research with small data sets and many eigenvalues in geology (He and Garcia, 2009; Seiffert et al., 2010; Fernández-Delgado et al., 2014). Therefore, based on the characteristics of the small scale and many eigenvalues of the current data set, we selected the RF algorithm to build a predictive model, and evaluated the importance of geological factors on the pore structure.

In view of the above research status, we carried out the following research. This study collected and analyzed >350 researches about the pore structure characterization of shale sediments, and classified the PSDs of different shale sediments. The purpose of this work is to reveal the influencing factors on shale PSD, and further establish a geological evaluation model for shale pore structure. This study summarizes the characterization methods of shale pore structure and the factors affecting the shale PSD, and proposes a shale PSD geological prediction model based on RF algorithm to predict shale PSD under different geological conditions. This model may reduce the cost and time required for pore structure characterization, and has certain reference significance for the understanding of shale pore structure in different geological settings.

## 2. Pore structure characterization methods

### 2.1. Mercury intrusion

Mercury injection experimental technology was first introduced into the oil and gas industry by Purcell in 1949, and has become an important

experimental method with which to characterize the pore structure of rock (Purcell, 1949; Dorsch, 1995). The mercury intrusion method obtains data such as PSD and PV based on the Washburn model according to the amount of mercury injected and the corresponding pressure (Jiang et al., 2016b). At present, the mercury intrusion method has been widely used to characterize the shale pore structure in marine shale sediments such as the Devonian to Mississippian Bakken shale, Cretaceous Eagle Ford shale and Permian Wolfcamp shale in North America and the Silurian Longmaxi shale in the Sichuan Basin (Ghanbarian and Javadpour, 2017; Hu et al., 2017; Zheng et al., 2018; Cavelan et al., 2019; Liu et al., 2019a; Hu et al., 2020; Gao et al., 2020), marine-terrestrial transitional shale including Upper Carboniferous-Lower Permian Shanxi-Taiyuan shale in the Ordos Basin (Yang et al., 2017a), and lacustrine shale involving Triassic Yanchang shale, Permian Lucaogou shale, Cretaceous Qingshankou shale and Paleogene Shahejie shale in Asian and so on (Li et al., 2015; Jiang et al., 2016a; Zhang et al., 2019a; Li et al., 2020; Zhang et al., 2020a; Zhou et al., 2020b; Shen et al., 2021).

Mercury is a non-wetting phase for most solid interfaces. Under the external pressure, mercury enters the micro-nano porous material and induces the capillarity. The strength of mercury's effect on the surface attraction of the porous medium is equal to the circumference (assuming the pore throat is circular). The balance state where the external force (P) is equal to the resistance can be expressed as (Fig. 2a) (Washburn, 1921; Chilingar et al., 1972).

$$-\pi D \gamma \cos \theta = \frac{\pi D^2 P}{4} \quad (1)$$

simplifying as:

$$D = -\frac{4 \gamma \cos \theta}{P} \quad (2)$$

The pore diameter D is inversely proportional to the external pressure P. Assuming that the contact angle  $\theta$  is  $130^\circ$  and the surface tension  $\gamma$  is  $485 \text{ dyne cm}^{-1}$ , the pressure required for mercury to enter the pores of approximately  $360 \text{ }\mu\text{m}$  is only 0.5 psi. For the micro-nano pores in shale, mercury can enter pores smaller than 3 nm in diameter when the pressure is 60,000 psi. The above formula assumes an oversimplified equivalent spherical pore. For layered silicates with slit-like pores, the expression can be modified to.

$$W = -\frac{2 \gamma \cos \theta}{P} \quad (3)$$

where W is the width between plates. Therefore, the relationship between mercury injection pressure and mercury saturation can be transformed into the PSD of shale pores by the mercury intrusion method (Figs. 2b and c).

For the characterization of shale pore structure, mercury intrusion has the followings limitations: (1) The shale has complex pore structure with micro-nano pore, and injecting at high-pressure damages the pore structure (Kuila and Prasad, 2013b; Yang et al., 2017b; Jiang et al., 2022). Different from tight sandstone, coal and tight limestone, etc., the high clay mineral and TOC contents in shale sediments result in a large number of nanoscale pores and strong heterogeneity (Toda and Toyoda, 1972; Spitzer, 1981; Friesen and Mikula, 1988; Ju et al., 2018; Lu and Liu, 2021; Guo et al., 2022; Hu et al., 2022). The strong capillarity makes it difficult for mercury to enter micropores and mesopores. The high external pressure will cause pore deformation and compression, and there will be loss in the measurement of large pores (Tian et al., 2012; Chen et al., 2015a; Cao et al., 2016; Zhu et al., 2016b; Sun et al., 2017a; Zhao et al., 2017; Wang et al., 2019b; Zhang et al., 2019c). In addition, the shale plug sample will have a significant fracture-making effect, which will affect the accuracy of the experiment. (2) The mercury injection volume and the minimum pore throat radius are limited by the maximum pressure of the experimental apparatus. For most instruments, the maximum mercury injection pressure is 60,000 psi. Assuming a contact angle of  $130^\circ$  and a surface tension of  $485 \text{ dyne cm}^{-1}$ , mercury can't enter pores with a diameter  $<3 \text{ nm}$ , which limits the detection accuracy. (3) The complex pore structures and strong heterogeneity of shale will affect mercury injection and the characterization of the all scale pore space. Previous study showed that the maximum mercury injection saturation is lower than 60% for most shale with porosity  $<5\%$  (Zhu et al., 2016a). Thus, there is reason to believe that high-pressure mercury injection is suitable for rock with porosity higher than 5%. (4) Mercury can only enter connected pores and cannot measure isolated pores. Therefore, the detected pore space may be smaller than the real pore space. The SEM results showed a large difference with mercury intrusion, which may be caused by the open and closed pores and the particle size (Rouquerol et al., 1994). Additionally, particle size affects the openness of pore space. The closed pores likely transformed into open pores for the smaller particle, resulting in an increase in porosity and SSA (Fig. 3a) (Jiao et al., 2014c). (5) Serious loss of core samples. The expensive and precious core is the most intuitive reflection of the underground situation. The high mercury injection pressure easily generates artificial cracks. Moreover, mercury is a toxic reagent, and the cores cannot be used for other experimental analysis after mercury injection. (6) The interfacial tension and the wetting angle involved in the mercury intrusion method are not fixed due to the nanoscale effect. They are strongly associated with the pore radius and present a more pronounced nanoscale effect below 8 nm (Fig. 3b) (Zhang and Meng, 2006; Wang et al., 2007; Yan et al., 2008; He, 2014). Therefore, it is necessary to correct these parameters, especially for the test of shale with micro-nano pore structure. (7) Preceding studies show complex and diverse pore types in shale sediments, including plate-

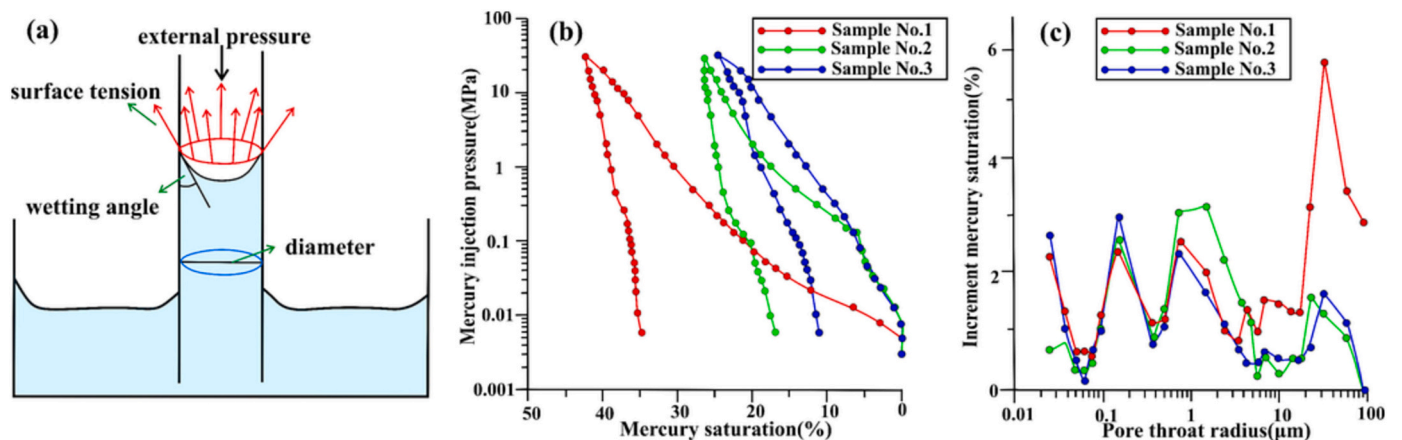
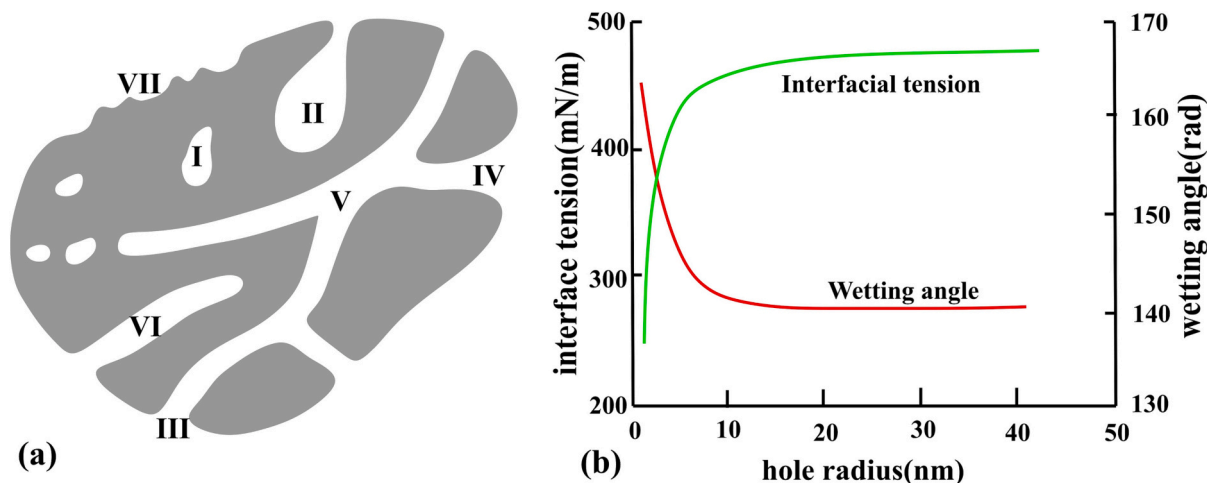


Fig. 2. Principle of mercury intrusion experiment (a), the test results (b) and the corresponding PSD (c) (Wang et al., 2019a).





**Fig. 3.** (a) shows the diagram of pore type and connectivity (I represents the closed pore; II-VI reflect the open pores, II and VI show blind pores; III-IV present throughpores; VII shows the roughness of the external surface). (b) presents the variation of interfacial tension and wetting angle with the pore radius (Jiao et al., 2014c).

shaped pores, spherical pores, and slit-shaped pores. The Washburn equation assumes that the pore in the sample is smooth cylindrical, which cannot reflect the real pore space. (8) The mercury intrusion method detects the maximum opening size of pores, so the existence of throats will make the PSD deviate from the reality (Giesche, 2006).

## 2.2. Gas adsorption

Gas adsorption technology utilizes a common phenomenon of physical adsorption. When the adsorbable gas (the adsorbate) contacts the surface of a solid (the adsorbent), a weak van der Waals force arises between them (Thommes et al., 2015). At present, supercritical gases commonly used for gas adsorption include  $N_2$  at 77 K, argon at 87.3 K and  $CO_2$  at 273.1 K. The selection of a suitable adsorbent is crucial for the characterization of the pore structure (Thommes, 2004; Thommes et al., 2012a). Nitrogen (77 K) gas adsorption is best suited for materials with pores in the range of 2–300 nm, similar to those ubiquitous in mudstone and coal (Anovitz and Cole, 2015). It is most sensitive to pores in the range of 2–100 nm and is currently the most widely used technology for mesopore (2–50 nm) characterization in sediments (Sing and Williams, 2004; Clarkson et al., 2013). The quadrupole of nitrogen molecules interacts specifically with various surface functional groups and exposed ions, which will affect the orientation of surface nitrogen molecules and the filling pressure in micropores (<2 nm). Thus, it is basically not used for micropore characterization. Argon (87 K) has advantages in the analysis of micropore, but it is difficult for nitrogen and argon to enter pores smaller than 0.45 nm due to the limitations of low temperature and active kinetics (Thommes et al., 2012b; Thommes et al., 2015). Therefore,  $CO_2$  (273 K) has been widely used for micropore characterization (Garrido et al., 1987; Cazorla-Amorós et al., 1996; Garcia-Martinez et al., 2000). Compared with nitrogen and argon at low temperature,  $CO_2$  has a relatively high absolute temperature and pressure, which makes it easier to enter the ultra-micropores. Moreover, the molecular dynamics diameter of  $CO_2$  (0.33 nm) is slightly smaller than those of nitrogen molecules (0.36 nm) and argon molecules (0.34 nm) (Sing and Williams, 2004), which avail it easier to enter micropores. In addition, the  $CO_2$  micropore analysis device is much simpler than the experimental device for argon or nitrogen adsorption (Bustin et al., 2008; Chalmers et al., 2012; Mastalerz et al., 2013; Wang et al., 2014; Chen et al., 2015b).

Before the adsorption experiment, the sample is generally degassed by heating and vacuumizing to remove the impurity gas adsorbed on the surface of the adsorbent. Then, probe gases such as  $N_2$  and  $CO_2$  are injected into the sample under isothermal conditions, and the adsorbed

amount is recorded under different pressures. Since the temperature and pressure during the experiment are lower than those at the critical point of gas liquefaction, the capillary condensation of adsorbed gas during this process can provide information such as sample pore shape, PV, SSA and PSD. The physical adsorption process of porous materials is affected by fluid-wall, fluid-fluid interactions and the fluid state in narrow pores, so the shape of the isotherm adsorption curve depends on the fluid-fluid and fluid-wall interaction strengths, as well as confined geometry effects coupled with the state of the pore and bulk fluid (Rathousky and Thommes, 2007). The capillary condensation phenomenon in the adsorption process of porous media will produce a hysteresis loop. Specifically, during desorption, since the radius of curvature of the liquid surface after capillary condensation is smaller than that before capillary condensation, the desorption pressure is always lower than the adsorption pressure for the same adsorption amount, resulting in a hysteresis loop. The shape of the hysteresis loop can reflect the pore shape. The International Union of Pure and Applied Chemistry (IUPAC) (Sing, 1982; Thommes et al., 2015) updated the classification of isotherm adsorption curves and hysteresis types. The hysteresis loop type can reflect different mesopore shapes (Fig. 4). H1 type reflects cylindrical holes with uniform diameter distribution of openings at both ends, and H2 type shows ink bottle holes, and H3 type holes represent flat slit structure, cracks and wedge-shaped structure holes. H4 type reflects layered slit holes, and often occurs in mixed microporous and mesoporous porous media or solids with narrow fractured pores (Broekhoff, 1967; Valiullin et al., 2006; Monson, 2012; Landers et al., 2013; Prisk et al., 2013; Olaremu, 2015; Thommes et al., 2015).

Moreover, PV, SSA, and PSD can be quantitatively characterized by using gas adsorption experiments (Fig. 5). The PV can be acquired from the quantity of gas adsorbed, which is expressed as moles or volume in  $cm^3 \cdot g^{-1}$  per mass and as a function of relative equilibrium pressure ( $P/P_0$ ). The SSA can be quantified by using the Brunauer-Emmett-Teller (BET) model with data from  $N_2$  adsorption under the relative pressures ( $P/P_0$ ) ranging from 0.05 to 0.35 (Anovitz and Cole, 2015).

Multiple models can be used to calculate the PSD, and it is necessary to optimize a suitable theoretical model (Li et al., 2015; Ko et al., 2017; Dong et al., 2019; Chandra et al., 2022). At present, density functional theory (DFT) and Barrett-Joyner-Halenda (BJH) models are commonly used models to calculate shale PSD using the gas adsorption method (Chalmers and Bustin, 2008; Chalmers et al., 2012; Milliken et al., 2013a). Previous studies have revealed that the DFT and BJH models usually produce similar PSD results (Li et al., 2015). The PSD calculated by the DFT model has multiple peaks, but the multi-peak phenomenon gradually disappears as the small pores gradually decreases. Therefore,

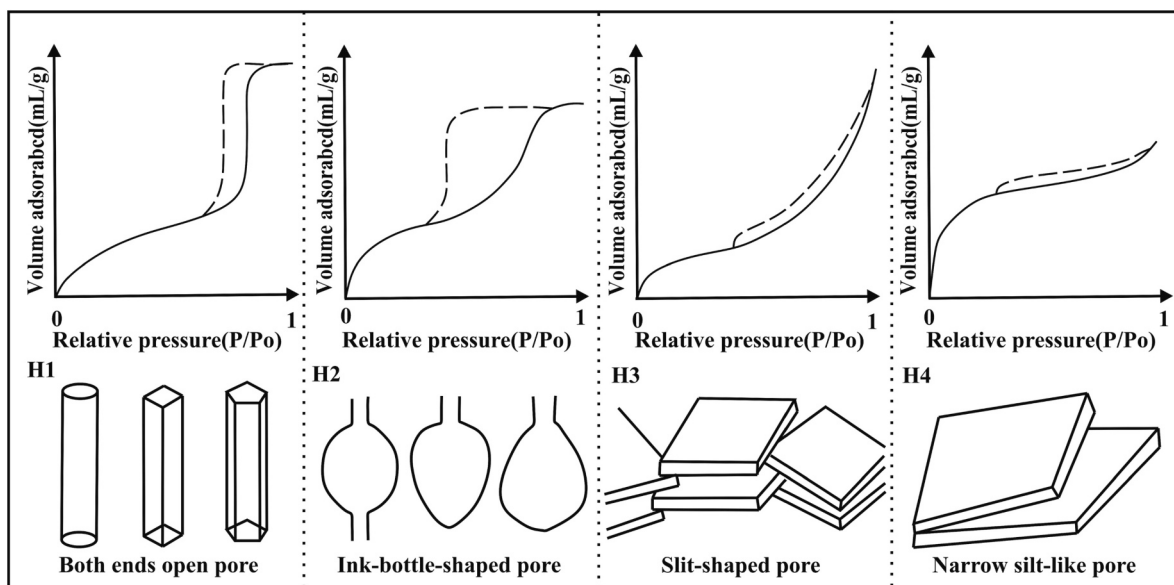


Fig. 4. Hysteresis loop characteristics and types of gas adsorption experiments (Thommes et al., 2015).

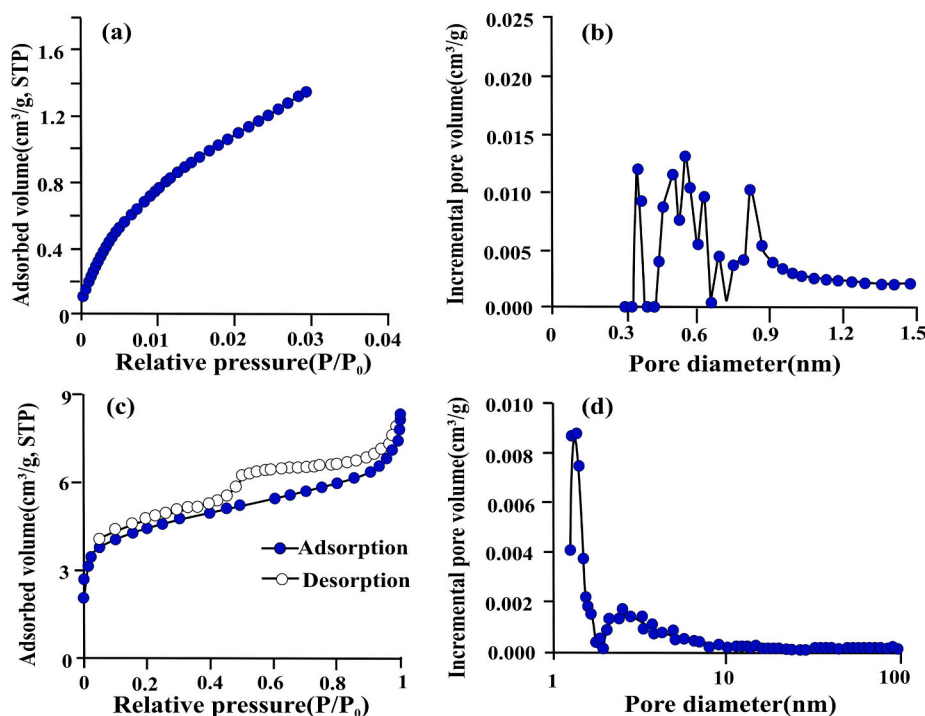


Fig. 5. The adsorption isotherm  $\text{CO}_2$  (a) and  $\text{N}_2$  (c) adsorption experiments and their PSD curves (b and d) (Han et al., 2016).

it is considered that the DFT model is more inclined to describe the PSD of micropores or narrow mesopores (Fig. 6) (Li et al., 2015). However, these multiple peaks may be generated by noise (Kuila and Prasad, 2013a). To date, little direct evidence has been provided to prove that the multiple peaks are caused by the real pore system. In addition, the Gurvich rule, Dubinin–Radushkevich (DR) method, comparison plot methods (e.g., t-method, alpha-s method), and Horvath and Kawazoe (HK) method have wrongly assumed that the adsorbate phase is bulk liquid-like, neglecting the inhomogeneity of molecular adsorption in the micropores (Dubinin, 1947; Dubinin and Timofeev, 1948; Sing, 1982; Horváth and Kawazoe, 1983; Rouquerol and Rouquerol, 2014). Thus, these approaches cannot truly characterize the actual micropore filling

of the material, which will lead to errors in the micropore size distribution.

Based on macroscopic thermodynamic assumptions, the proposed modified Kelvin equation is a classic mesoporous analysis method, including BJH and other methods (Sing, 1982). However, the Kelvin equation model is not applicable to narrow mesopores smaller than 10 nm, which will lead to an underestimate of the pore size by as much as 20–30% (Kruk et al., 1997; Neimark et al., 2003; Thommes, 2004; Jaranić and Solov'yov, 2006; Thommes et al., 2012b). Therefore, classical macroscopic theory and semi-empirical methods cannot truly characterize the filling of micropores and narrow mesopores, and cannot accurately characterize the full PSD. Based on the grand canonical

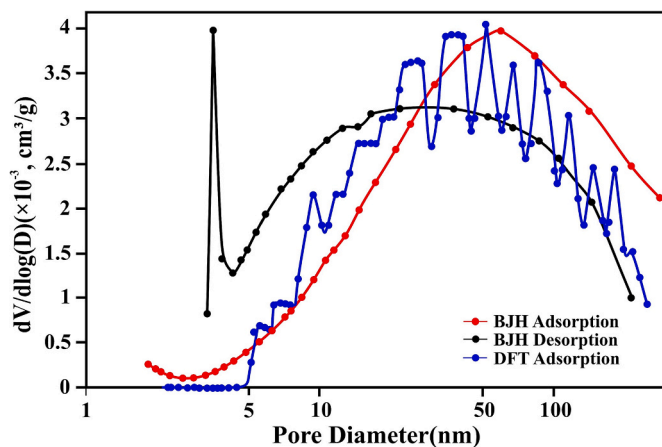


Fig. 6. Comparison of PSD calculated by BJH and DFT models (Li et al., 2015).

Monte Carlo (GCMC) and DFT methods of microscopic molecular simulation, the adsorption and phase behavior of fluids in narrow channels and micropores are described at the molecular level, solving the related problems of the above macroscopic thermodynamic methods. Compared with classical methods, with GCMC and DFT methods, more reliable PSD can be obtained in the micropore and mesopore ranges (Monson, 2008; Monson, 2012).

Local density functional theory (LDFT) was first used for pore size analysis in 1989 (Seaton and Walton, 1989), but its error is large in the micropore range. Nonlocal density functional theory (NLDF) was first proposed in 1993 (Lastoskie et al., 1993), significantly improving the characterization accuracy and more truly reflecting the thermodynamic properties of pore fluids in porous media (Ravikovitch and Neimark, 2006a; Thommes et al., 2012a; Zhang and Yang, 2013). Compared with classical macroscopic theories such as BJH, t-plot and DFT, NLDF is more suitable for characterizing organic-rich shale with a wide distribution of pore sizes (0.33–100 nm) and complex pore structures (Wei et al., 2016). However, its disadvantage is that the solid surface is assumed to be smooth (Olivier et al., 1994; Neimark, 1995). Molecular simulation studies show that solid surface roughness as well as heterogeneity can affect the shape of the adsorption isotherm and thus the PSD accuracy (Lucena et al., 2010). Quenched solid density functional theory (QSDFT) can quantitatively explain the heterogeneity of solid surfaces and is suitable for the characterization of micropores and mesoporous pores, especially for micropores (Ravikovitch and Neimark, 2006b). The application of QSDFT significantly improves the PSD of nanoscale porous media (Thommes et al., 2012a).

Although gas adsorption has gradually been widely used in shale sediments, it is still necessary to pay attention when using it due to the influence of experimental conditions and model development: (1) Gas adsorption can non-destructive and easier to characterize micropore (<2 nm) and mesopore (2–50 nm) by CO<sub>2</sub> and N<sub>2</sub> adsorption respectively, but these technologies are costly and ineffective for the characterization of macropore (>300 nm) (Neimark et al., 2023; Thommes, 2004; Thommes, 2010; Rouquerol and Rouquerol, 2014). (2) The results of gas adsorption experiments are greatly affected by the sample particle size and experimental conditions, such as the boosting rate (Jiao et al., 2014c; Han et al., 2016). In addition, the pre-treatment and key parameters of CO<sub>2</sub> adsorption experiment have not yet been unified (Chalmers et al., 2012; Tian et al., 2012; Mastalerz et al., 2013; Luo et al., 2015; Zhu et al., 2016b; Ko et al., 2017; Dong et al., 2019; Wang et al., 2020). (3) This method is expensive and time consuming and provides fewer data points. In addition, due to the complex characteristics of nitrogen molecules in pores with the same diameter as the nitrogen molecules, the adsorption amount cannot fully represent the pore space, resulting in low measurement accuracy. (4) Similar to mercury intrusion, gas adsorption can measure only interconnected pores and is

invalid for isolated pores. (5) Theoretical model optimization is crucial to the accuracy of PSD analysis, but systematic studies on the applicability of different PSD models are still rare.

### 2.3. Nuclear magnetic resonance

NMR technology is a method of analyzing pore structure based on the distribution of the NMR signal intensity. It has the advantages of rapid, non-destructive and multi-parameter measurement and is widely used in pore structure and fluid characterization of rock (Menger and Prammer, 1998; Xiao, 1998; Daigle and Dugan, 2011; Saidian and Prasad, 2015; Adeyilola et al., 2020; Knapp et al., 2020). NMR is a physical phenomenon produced by the weak interaction between the nucleus and surrounding ions caused by the spin characteristic generated by the internal angular momentum of the nucleus (Bloch, 1946). Therefore, only spinning nuclei, such as <sup>1</sup>H, <sup>19</sup>F, <sup>31</sup>P, <sup>23</sup>Na, <sup>13</sup>C, are the object of NMR research, and the most commonly used is the hydrogen nucleus <sup>1</sup>H (Xiao et al., 2001; Wang et al., 2005; Li et al., 2017).

In NMR, relaxation refers to the phenomenon that when the nucleus resonates and is in a high-energy state, it quickly returns to the original low-energy state after the radio frequency pulse stops. The recovery process is called the relaxation process, which is a process of energy conversion. The speed of the relaxation process is expressed by the relaxation time, which reflects the interaction between the total protons of the proton system and the environment surrounding the protons. The relaxation process is divided into two steps, including the restoration of the longitudinal magnetization  $M_z$  to the initial equilibrium state of  $M_0$  and the decay of the transverse magnetization  $M_{xy}$  to 0 (Fig. 7).

Three relaxation mechanisms occur for the fluids in rocks (Coates et al., 1999): (1) bulk relaxation in connection with the intrinsic fluid properties, (2) surface relaxation reflecting the characteristics of the interaction between fluids and the solid grain interfaces, and (3) diffusion relaxation induced by the gradient field. The relaxation processes mentioned above act in parallel, and their rates are additive. The NMR response to the fluids confined in the pore space can be described as (Coates et al., 1999):

$$\frac{1}{T_2} = \frac{1}{T_{2B}} + \frac{1}{T_{2S}} + \frac{1}{T_{2D}} \quad (4)$$

where  $T_2$  is the transverse relaxation time of the pore fluid,  $1/T_{2B}$  is the bulk contribution,  $1/T_{2S}$  is the surface contribution, and  $1/T_{2D}$  is the diffusion in the field gradient contribution.

For a water-wet rock, the relaxation of water is dominated by the surface relaxation mechanism, while the relaxation of oil is dominated by bulk relaxation (Coates et al., 1999). Any water present will be in contact with pores or occur as pendular drops in pores. In contrast, the occurrences of oil and water will be reversed in a strongly oil-wet rock. Fine grains are significant barriers to diffusion, and diffusion relaxation would decrease under a low and uniform magnetic field (Kleinberg and Horsfield, 1990; Coates et al., 1999; Yao et al., 2010). Therefore, for the water in water-wet rock under a homogenous magnetic field, only surface relaxation should be considered.

For the surface relaxation mechanism, the relaxation time observed in NMR experiments is the average relaxation time for all the nuclei in the pores (Coates et al., 1999; Hodgkins et al., 1999). The nuclei in small pores more easily interact with the grain surface than those in larger pores. Therefore, a shorter relaxation time could reflect the smaller pores (Coates et al., 1999; Hodgkins et al., 1999). The rates of relaxation are generally related to surface relaxation and pore surface-to-volume ratio, and this relationship can be described as (Coates et al., 1999; Hodgkins et al., 1999):

$$\frac{1}{T_2} = \rho \frac{S}{V} \quad (5)$$

where  $T_2$  is the transverse relaxation time resulting from surface

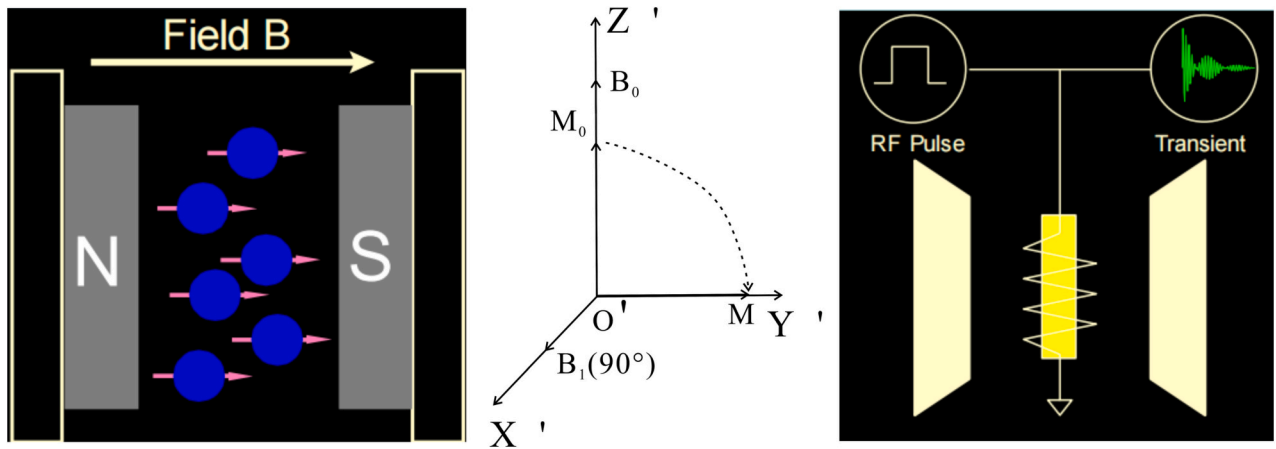


**Fig. 7.** Relaxation process and relaxation time (Z-axis direction-equilibrium state, the magnetic induction  $M_0$  is proportional to the fluid volume; a  $90^\circ$  pulse is applied to  $M_0$ , and  $M_0$  deviates from the equilibrium state to the non-equilibrium XY plane; after the  $90^\circ$  pulse disappears,  $M_0$  recovers to the equilibrium state, and this recovery process is called relaxation time).

relaxation (in seconds) and  $\rho$  is the surface relaxivity (in microns/s), which is related to the concentration of paramagnetic sites on pore walls and reflects the ability of pore walls to promote proton relaxation.  $S/V$  is the surface area-to-volume ratio (per micron) reflecting the pore size. For simple shapes, the surface-to-volume ratio is  $3/r$ , where  $r$  is the radius of the sphere (Coates et al., 1999). For complex shapes, a shape factor  $F_p$  will be used to describe the surface-to-volume ratio as (Liu et al., 2008):

$$r = \rho F_p T_2 \quad (6)$$

If the surface relaxivity can be determined, the NMR  $T_2$  spectrum can be used to quantitatively characterize the PSD. The surface relaxivity varies with the mineralogy (Kleinberg, 1996; Coates et al., 1999). Carbonate surfaces exhibit a lower surface relaxivity than that of quartz surfaces, and high-iron rocks have a higher surface relaxivity (Coates et al., 1999). Moreover, due to the influence of paramagnetic substances on the relaxation time of atomic nuclei, the surface relaxation rate of rocks cannot be calculated by theoretical models (Hurlimann et al., 1994; Kleinberg et al., 1994a; Dunn et al., 2002; Fleury, 2007). Currently, there are three methods to obtain the surface relaxation rate: (1) matching the PSD curve obtained by nitrogen adsorption or high-pressure mercury intrusion with the  $T_2$  curve (Fig. 8) (Li et al., 2008; Yao and Liu, 2012). (2) based on the core SSA obtained by cation

exchange, nitrogen adsorption, image analysis, etc.; and (3) only considering the combination of NMR measurement methods (Jia, 2018). These three methods are subjective and empirical, which will reduce the accuracy of PSD conversion.

The NMR technique to characterize the shale pore structure also has some limitations: (1) NMR can reflect only the distribution trend of the pore size and cannot reflect the absolute value of the pore volume. However, the key parameters of pore size conversion, surface relaxation rate and shape factor are highly subjective and have not yet been unified (Loucks et al., 2009). Therefore, there may be problems in the conversion of  $T_2$  and pore size. (2) NMR is affected by the nature of the sample itself, the nature of the fluid, and the content and type of ions in the fluid, etc. The fluids in shale are complex, especially for the shale with low thermal maturity, which is mostly filled with high-viscosity and high-density macromolecular hydrocarbons. The high-viscosity fluids have weak free diffusion; thus, the bulk relaxation cannot be ignored. In addition, when there are many paramagnetic substances such as iron and manganese in shale sediments, the NMR signal will be distorted (Kleinberg et al., 1994b). (3) Since the shale is very dense, the centrifugation efficiency is low. The maximum rotational speed for NMR experiments is generally 12,000 rpm (approximately 5.68 MPa, corresponding to a radius of 25.4 nm). Smaller pores will bear more pressure, which will lead artificial risk of crushing and inaccurate

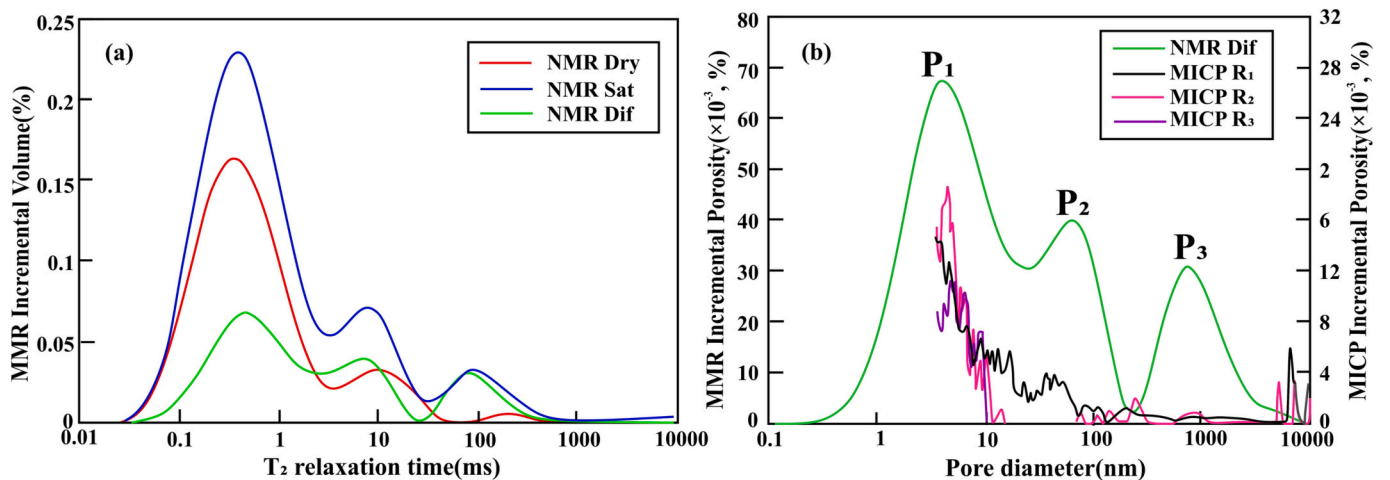


**Fig. 8.** NMR  $T_2$  spectrum distribution (a) and its transform to PSD (b). The green curve represents connected porosity accessible to lab brine.  $T_2$  distribution converted to PSD by alignment with the PSD obtained by mercury intrusion (Knapp et al., 2020). (For interpretation of the references to color in this figure legend, the reader is referred to the web version of this article.)



results. (4) When using NMR to characterize the shale pore structure, it is necessary to saturate the sample with water. However, shale contains abundant clay minerals. Minerals such as montmorillonite will expand when exposed to water and block the original pores, resulting in inaccurate characterization results. In addition, since bound water always exists in rock pores, the NMR signal includes the signal of bound water, which may easily lead to contradiction on the result with other methods. (5) NMR can only measure the characteristics of interconnected pores and is not reflective of isolated pores.

#### 2.4. Small-angle scattering

The SAS technique obtains microstructure information by detecting scattering in a small angle range after the ray beam passes through the sample, mainly including small-angle X-ray scattering (SAXS) and small-angle neutron scattering (SANS). USAS is consistent with the principle of small-angle scattering technology, mainly including ultra-small-angle neutron scattering (USANS) and ultra-small-angle X-ray scattering (USAXS) (Radlinski et al., 2004). The SAS technique is mainly used to study the submicroscopic structure and morphological characteristics of materials. The most suitable research object is the particle with a rotation radius of 1–5 nm and volume of approximately 200–800 nm<sup>3</sup>, which is equivalent to a particle mass of  $(1-50) \times 10^{-20}$  g, a density of 1–2 g/cm<sup>3</sup>, and a relative molecular mass 5000–250,000 (Zhu, 2008). SAS technology can quickly and non-destructively analyze pore structure under different temperature and pressure conditions. Therefore, it is an effective method to characterize the pore structure of porous materials, and its measurement range is wide (0.5 nm to 20  $\mu$ m) (Fig. 9) (Melnichenko et al., 2012).

In recent years, some scholars have introduced this technology to characterize the pore structure of unconventional reservoirs such as coal (Radlinski et al., 2004), carbonate rock (Skalinski and Kenter, 2013), and shale (Clarkson et al., 2013; Liu et al., 2017b; Zhang et al., 2017; Liu et al., 2019b; Zhang et al., 2019c; Zhang et al., 2020b). The analysis results of the pore structure of shale in North America by mercury intrusion, N<sub>2</sub>/CO<sub>2</sub> gas adsorption and SANS/USANS show good agreement (Clarkson et al., 2013). The SAS technique can also be used to discuss the closed pore by comparison with gas adsorption (Sun et al., 2017b). The accuracy of converting SAS results to PSD is closely dependent on the interpretation model. A variety of models for calculating the aperture have been proposed, including the smooth surface approach (Anovitz et al., 2013), the polydisperse hard sphere model (Hinde, 2004; Radlinski, 2006), regularization or maximum smoothness (Glatter, 1977; Glatter, 1979; Svergun, 1991), and total non-negative least squares (Ilavsky and Jemian, 2009) etc. The different models used for simulation would induce large differences (Ilavsky and Jemian, 2009; Anovitz et al., 2013; Anovitz et al., 2015). For single material with

relatively simple pore structure, the mature relationship model between diffraction intensity and pore size could facilitate high accuracy and repeatability of SAS technology (Li, 1995; Qin et al., 2001; Xu and Li, 2003). However, it is problematic to calculate pore radii based on pore volume for media with complex pore shapes (Anovitz et al., 2009; Anovitz et al., 2013). At presently, the SAS technique is still in its infancy in the field of the pore structure characterization. Currently, no convincing interpretation of the diffraction intensity and data model has been made in the literature. Therefore, the SAS interpretation model is not applicable for describing the complex pore structure of shale sediments.

Therefore, the SAS technique has some limitations in analyzing the pore structure of shale sediments: (1) The SAS technique is based on the synchrotron radiation platform, which is expensive and time-consuming to operate. (2) The existing interpretation model is suitable for materials with single-component and simple-structure, which is not appropriate for the shale sediments with complex and diverse pore structures. Moreover, it cannot provide accurate pore structure information. (3) The particle sizes of shale sediments are mainly between 30 nm and 30  $\mu$ m, and the density of shale is mostly >2 g/cm<sup>3</sup>, which is beyond the most effective range of SAS technology (Zhu, 2008). (4) For shale sediments, SAS technology lacks a unified analysis process, including sample preparation and blank extraction (Zhu et al., 2016a).

#### 2.5. Electron microscopy

Optical microscope is difficult and ineffectual to use to describe the pore structure of shale sediments, the main particle size of which is <0.03 mm. Electron microscope observation is the widely used and most intuitive method to characterize the pore structure of shale sediments recently. Various microscopic observation techniques have been extensively developed, including transmission electron microscope (TEM), scanning electron microscope (SEM), and atomic force microscope (AFM) (Fig. 10). Moreover, combined with statistics and image analysis, quantitative information such as porosity and PSD can be obtained (Fredrich et al., 1995; Klaver et al., 2012; Giffin et al., 2013; Jiao et al., 2014a).

The basic principle of TEM is to transmit an accelerated and focused electron beam onto a very thin sample; the electrons collide with the atoms in the sample and change their direction, which will cause solid angle scattering, resulting in different light and dark effects (Fig. 11a). Scholars have tried to use TEM to study the micro-nano pore structure of shale sediments with different maturities (Anderson, 2014; Bernard and Horsfield, 2014) and to analyze the effect of the tortuosity of marine fine-grained sediments on clay-OM systems (Douglas et al., 2013). The two-dimensional (2D) TEM image would mix the surface and inside information of sample. This shortcoming has also been confirmed in

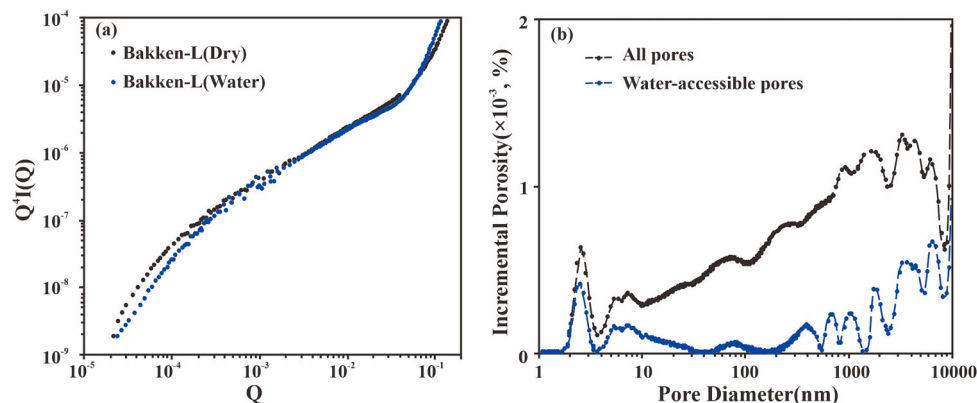
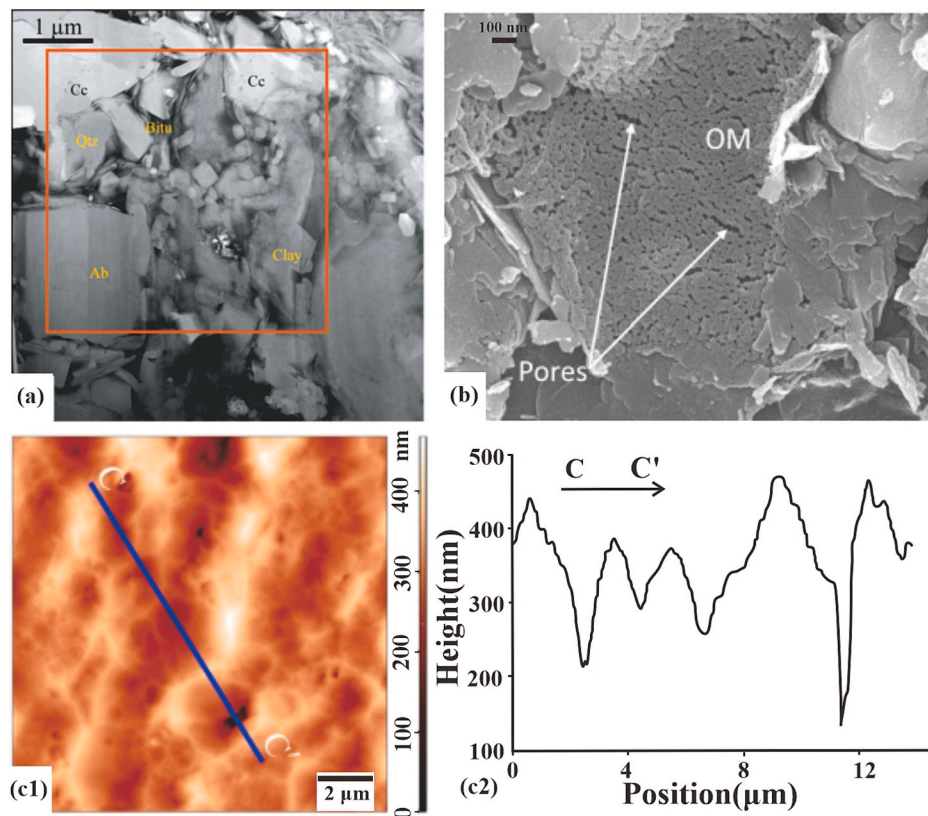
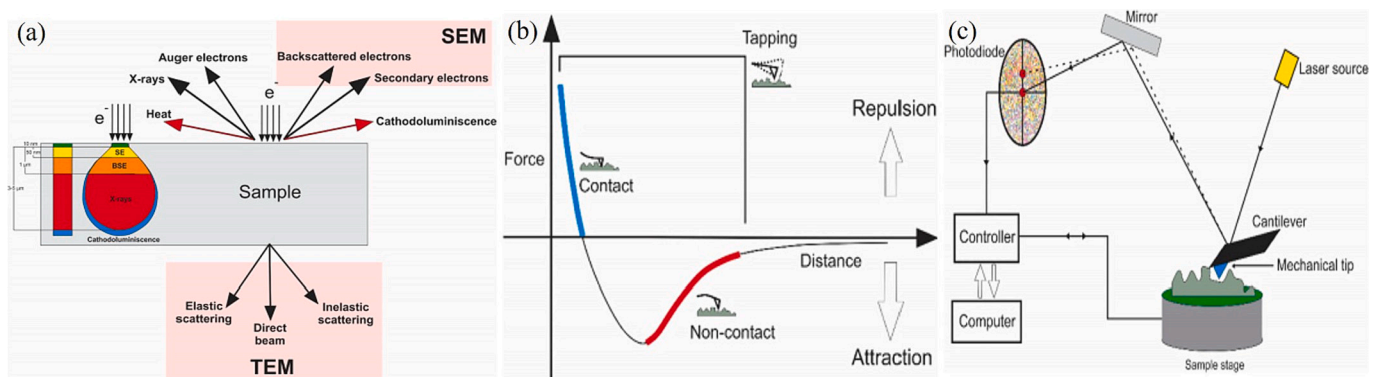


Fig. 9. (a) shows the relation of scattering intensities ( $Q^4 I(Q)$ ) and the scattering vector ( $Q$ ); acquired by (U)SANS. (b) represents the PSD curves (Zhang et al., 2020b).



**Fig. 10.** Electron micrograph obtained by TEM (a), SEM (b) and AFM (c1). The relative height at different positions of the scanning surface can be displayed by AFM (c2) (Zhao et al., 2019; Chandra and Vishal, 2021).



**Fig. 11.** (a) shows the different modes of beams emerging from the sample surface due to electron bombardment and their corresponding penetration depth (Bernard et al., 2013). (b) shows the force vs. distance between the tip and sample surface plot during different imaging methods in AFM; (c) shows the schematic of the imaging process in AFM (Li et al., 2018).

previous researches (Douglas et al., 2013; Anderson, 2014).

Based on the light lever principle, AFM analyzes the surface structure and morphology of the sample by detecting the weak interaction between the sample surface and the force-sensitive original (Ding et al., 2012). The force-distance curve can reflect the pore characteristics and surface topography of the sample (Fig. 11b and c) (Yang et al., 2019b). The high resolution and advanced analysis methods such as cross-section analysis, phase analysis and particle size analysis, make AFM widely used in materials science, biology, geology and other fields (Bruening and Cohen, 2005; Yao et al., 2011). The major advantage of AFM is the ability to perform imaging and mechanical measurements nondestructively with a spatial resolution down to the atomic scale in any desired environment (air, vacuum, liquid), thus allowing observation of in-situ heating or in-situ chemical reactions at the micro-nano

scale, which cannot be achieved by other imaging techniques at such a high resolution (Wang et al., 2021a). AFM technology has recently been used in the study of pore structure in shale sediments (Yang et al., 2016a; Liu et al., 2019c; Xu et al., 2019).

SEM is currently the most commonly used observation and analysis tool under the microscope (Fig. 11a). The high-resolution field emission scanning electron microscope (FE-SEM) and wide ion beam combined with field emission scanning electron microscope (FESEM-BIB), polyion beam etching and field emission scanning electron microscope dual beam system (FESEM-FIB) are the current mainstream methods to study the micro-nano pore structure in shale sediments (Loucks et al., 2009; Bernard et al., 2012; Fishman et al., 2012; Milliken et al., 2013b; Ma et al., 2016). At present, FE-SEM research mainly focuses on the qualitative describing the morphology of nanoscale pores. Some scholars

have applied the BIB-SEM to the quantitative characterization of the PSD of shale sediments (Desbois et al., 2011; Klaver et al., 2012; Giffin et al., 2013). FESEM-FIB could realize the synchronization of sample cutting and scanning. Combined with image reconstruction and energy spectrum analysis, it can realize 3D reconstruction and in-situ observation of shale storage space. FESEM-FIB technology has been widely used in the qualitative analysis of nanoscale pores (Chalmers et al., 2012; Loucks et al., 2012). The pore structure of Barnett shale in North America has been quantitatively characterized in 3D by FESEM-FIB technology (Curtis et al., 2012b; Dewers et al., 2012; Bai et al., 2013a).

Although various electron microscopy techniques have been developed to characterize pore structures, some drawbacks are unavoidable. (1) The sample pretreatment is very important to the image presentation effect, which will affect the resolution and quality of the original information for the sample. (2) The instrument restricts the lower limit of the pore size, and parameter settings can also affect the quality of image analysis. (3) Micro-area analysis and artificial interesting regional selection will inevitably lead to a reduction in representativeness of the overall characteristics of the sample. For example, TEM technology needs very thin sample in view of the absorption and scattering of the electron beam, which increases the difficulty of sample preparation and reduced the representative. (4) FIB technology requires injecting gallium ions for etching of the sample by the gallium ion beam, which will lead to different degrees of amorphization on the sample surface (Mayer et al., 2007). In addition, the thermal energy generated by the bombardment of the ion beam during the polishing process will significantly increase the random reflectivity of the OMs. Meanwhile, light organic volatiles will volatilize rapidly, resulting in a larger surface porosity of the OMs (Sanei and Ardakani, 2016).

## 2.6. Computed tomography

X-ray computed tomography (X-CT) is a technology developed in recent years that uses X-rays to perform comprehensive and fast non-destructive scanning imaging of rock samples (Fig. 12) (Dong et al., 2020). It can present the distribution of microscopic pores and throats in three-dimensional (3D) space as well as other special shape pores (Tomutsa and Radmilovic, 2003; Lame et al., 2004; Tomutsa et al., 2007). Since X-rays will present exponential attenuation when encountering particles, the degree of attenuation depends on the particle densities. Therefore, the density of the substance can be determined by comparing the attenuation of X-rays. When X-rays penetrate an object,

its energy change can be expressed as:

$$I = I_0 \exp(-\alpha \rho \chi) \quad (7)$$

where  $I_0$  and  $I$  are the light intensities before and after the X-ray penetrates the object, respectively.  $\alpha$  is the absorption coefficient of the X-ray by the substance, which is generally related to the wavelength of the X-ray.  $\rho$  is the density of the substance;  $\chi$  is the transmission length of the incident X-ray (Yu et al., 2012). In the CT scan image, the gray value reflects the material density. The change from black to white represents the change in density from small to large. The denser the substance, the higher its brightness in the CT image. Pores and cracks have the lowest density and appear almost black or with high gray values. Thus, the shape and distribution of pores can be analyzed through the color changes on the reconstructed image, and the characteristics of different minerals and pores can be semi-quantitatively characterized through the analysis of the gray value of each pixel (Fig. 13).

Combined with the rock composition revealed by energy spectrum analysis, CT technology can display 3D spatial structure and material composition of the sample. The precise positions of pore throats and composition in the sample will also be presented. Thus, CT technology can reflect the heterogeneity of the microscopic pore-throat distribution in shale, which is difficult to achieve by mercury intrusion and gas adsorption (Bryant et al., 1993; Bakke and Øren, 1997). The resolution is a key parameter for CT technology. Industrial CT scans can reveal the internal microscopic features of rock samples in the range of 0.1  $\mu\text{m}$  to 1 mm, and this range is 0.01–100  $\mu\text{m}$  for synchrotron radiation micro-nano CT, and 10 nm–100 nm for nano-CT (Yao et al., 2009; Bai et al., 2013b).

Although CT technology is advanced and convenient for studying the pore structure of shale sediments, the limitations still remains: (1) The resolution limits CT technology effectively distinguish nanoscale particles and pores. (2) Sample processing is difficult. To acquire higher resolution, the sample size should be very smaller, which leads to lower representativeness of the interpretation result for full sample. (3) Similar to FIB-SEM, CT technology has the problem of high testing cost, so it is not widely promoted. (4) The accuracy of different-scale characterization and 3D reconstruction of CT technology depends on the improvement of reconstruction algorithms and the development of micro-nano processing technology. (5) The key to the characterization of the pore structure of the sample by CT technology is the extraction of the pore space. In this process, human subjective factor has a great influence on the pore extraction. Therefore, CT processing result need other experiments to verify its reliability, which brings about the money and time consuming.

## 3. Methodology

### 3.1. Data compilation

In order to study the characteristics and differences of shale pore structure, this study collected >350 sets of data about the pore structure of shale sediments. The data contain the information about the pore structure and the geological features, which were used to summarize the difference of pore structure for shale sediments with different geological conditions as well as their main controlling factors. The collected shale samples cover the main shale areas developing shale oil/gas in the world (Fig. 14). Marine shale is the most developed shale sediments around the world, and the collected marine shale data include data from the Eagle Ford Shale in the western Gulf of Mexico, the Bakken Shale in the Williston Basin, the Vaca Muerta Shale in the Neuquén Basin, the Marcellus Shale in the Appalachian Basin, the Kimmeridge Clay Formation Shale in the Cleveland Basin, the Duvernay Shale in the Alberta Basin, the Wolfcamp Shale in the Midland Basin, the Carynginia Shale in the Perth Basin, and the Dalong Shale, Niutitang Shale, Wufeng Shale and Longmaxi Shale in the Sichuan Basin, etc. Marine-terrestrial transitional shale is infrequent, including that in the Shanxi Formation, Taiyuan

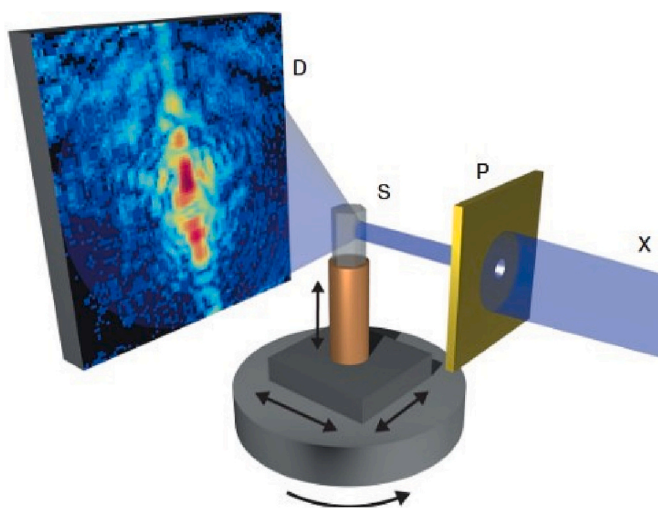


**Fig. 12.** Schematic diagram of computed tomography (Dierolf et al., 2010). The X-ray beam (X) irradiates the sample (S) through a pinhole (P), and then the X-ray diffraction image could be received by a 2D pixel detector (D). The sample could move and rotate 360° on the stage.



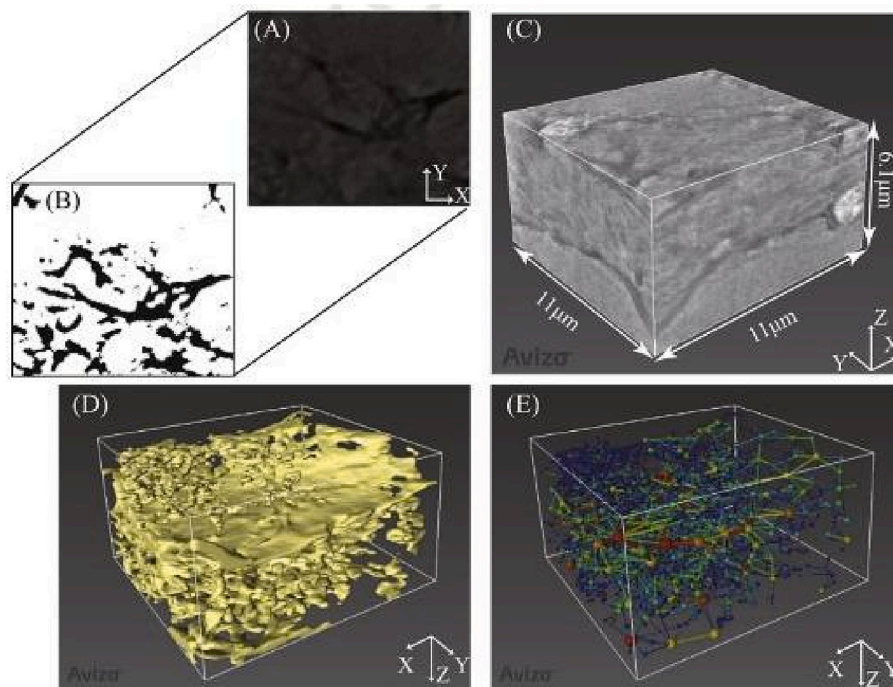


**Fig. 13.** Application of CT technology for pore structure characterization (Wang et al., 2016). (A) reconstructed 2D images in the XY-plane. (B) segmentation of the slice into pore (black) and non-pores (white). (C) reconstructed 3D microstructures. (D) the 3D pore network reconstruction. (E) the 3D pore-throat model skeletal structure.



**Fig. 14.** Sampling data sites. ① Permian Lucaogou Shale of Junggar Basin; ② Triassic Yanchang Shale, Upper Carboniferous-Lower Permian Benxi Shale, Shanxi Shale and Taiyuan Shale of Ordos Basin; ③ Paleogene Shahejie Shale of Bohai Bay Basin; ④ Cretaceous Qingshankou Shale of Songliao Basin; ⑤ Upper Ordovician Wufeng shale, Lower Silurian Longmaxi Shale, Permian Longtan Shale and Dalong Shale, Cambrian Shuijingtuo Shale of Upper Yangtze; ⑥ Lower Cambrian Niutitang Shale, Jurassic Dongyuemiao Shale, Permian Dalong Shale of Middle Yangtze; ⑦ Jurassic Dameigou Shale of Qaidam Basin; ⑧ Devonian Duvernay Shale, Cretaceous Milk River Shale of Alberta Basin; ⑨ Cretaceous Eagle Ford Shale of Eagle Ford Basin; ⑩ Mississippian Barnett shale of Fort Worth Basin; ⑪ Devonian Muskwa shale of Horn River Basin; ⑫ Devonian Woodford shale of

Oklahoma; ⑬ Jurassic Haynesville shale of North Louisiana Salt Basin; ⑭ Devonian Marcellus shale, Upper Ordovician Utica shale of Appalachian Basin; ⑮ Cretaceous Niobrara Shale of Denver Basin; ⑯ Permian Wolfcamp Shale of Midland Basin; ⑰ Permian Caryngina Shale of Perth Basin; ⑱ Permian Roseneath and Murteree Shale of Canning Basin; ⑲ Permian Roseneath and Murteree Shale of Cooper Basin; ⑳ Jurassic Vaca Muerta Shale of Neuquén Basin; ㉑ Jurassic Kimmeridge Clay Shale of Cleveland Basin; ㉒ Devonian to Mississippian Bakken Shale of Williston Basin.

Formation, and Benxi Formation in the Ordos Basin. Continental shale mainly develops in the lacustrine facies, which has been well explored in China. The collected lacustrine shale includes the Lucaogou shale in the Junggar Basin, the Shahejie shale in the Bohai Bay Basin, the Yanchang shale in the Ordos Basin, the Qingshankou shale in the Songliao Basin, and the Murteree Formation shale in the Cooper Basin, etc. The gas adsorption is the most common method used to study the shale pore structure, and total 240 sets of available nitrogen adsorption data were

collected. The mercury injection method follows, and this study collects 71 sets of available mercury injection data. Moreover, dozens of data from SAS, NMR and SEM were also collected. In addition, the depth, thermal maturity, kerogen type, TOC content, sedimentary facies, mineral composition and petrographic information of these samples were also statistically compiled.



### 3.2. Data screening and model

#### 3.2.1. Data screening

As mentioned above, many methods can currently be used to characterize pore structure with various advantages and disadvantages. This study mainly selects nitrogen adsorption data to summarize and sort out the characteristics of shale pore structure and obtains the main geological factors affecting shale pore structure. The nitrogen adsorption method and related data were selected in this study in view of (1) though the complex shale pore structure spans nanometer to millimeter scale, many studies show that the mesopores (2–50 nm) dominate the pore structure in shale sediments (Zou et al., 2012; Zhu et al., 2016a). The gas adsorption method is sensitive to pores in the range of 2–100 nm, and has the highest detection accuracy for mesopores at this scale (Clarkson et al., 2013). (2) Nitrogen adsorption technology is the most mature technology compared with other methods for pore structure characterization, which has abundant calculation models and relatively reliable calculation results. (3) The nitrogen adsorption method is currently the most widely used method for pore structure characterization. The mainstream shale formations worldwide were performed with pore structure analysis by nitrogen adsorption, thus the database of nitrogen adsorption is abundant. Therefore, the nitrogen adsorption data are extensively representative. (4) Nitrogen adsorption technology can not only qualitatively evaluate pore type, but also quantitatively analyze the pore structure. (5) The nitrogen adsorption method is nondestructive and comprehensive. Other methods have more or less limitations, especially the human influence, sample unnatural damage, unrepresentative local analysis, etc.

#### 3.2.2. Standardization

The PSD acquired by the nitrogen adsorption method is the representation of the volume occupied by pores with different diameters. The occupied space at different pore size was presented as cumulative pore volume, incremental volume, or differential ( $dV/dD$ ) distribution curves with respect to pore volume by numerous studies (Fig. 15) (Clarkson et al., 2013; Tian et al., 2013; Wei et al., 2018). Therefore, to compare the PSDs of different shales, it is necessary to unify the format. The cumulative pore volume could show the difference of overall space among different samples, while it cannot reflect the variation among different scale of pore sizes for one sample. The  $dV/d(D)$  vs.  $D$  curve can reflect the variation of pore space among different pore sizes especially for mesopores. The  $dV/d\log(D)$  vs.  $D$  curve can magnify the tiny difference for full scale pore sizes, and has good visual perception (Fig. 15) (Meyer and Klobes, 1999; Wei et al., 2018). Therefore, this study unifies the nitrogen adsorption data via  $dV/d\log(D)$  vs.  $D$  presentation. It should be noted that the obvious noise in the PSDs may be caused by small fluctuations due to the experimental temperature, and the noise caused will be amplified when taking the derivative (Clarkson et al., 2013). The PSD curves derived from the desorption branch of the isotherm show a strong artificial pore peak at approximately 4 nm as the result of the tensile strength effect phenomenon (Groen et al., 2003).

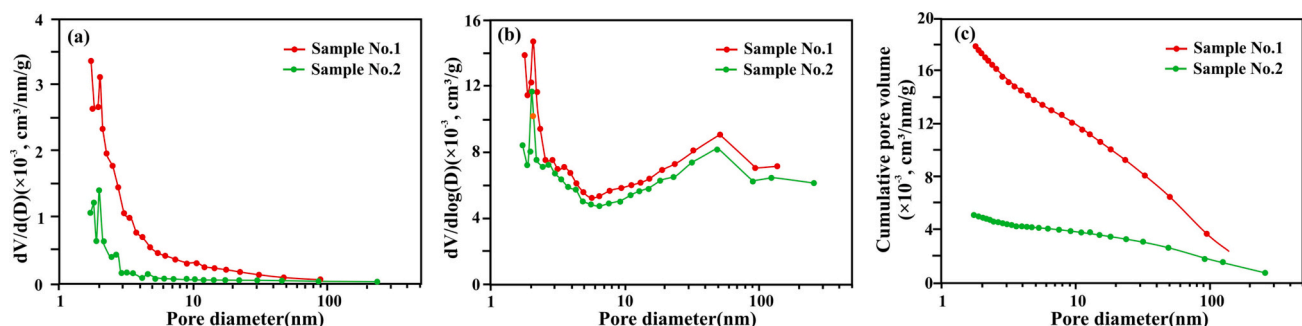


Fig. 15. Different presentation of the PSD derived from the  $N_2$  desorption branch of isotherms for shale samples (Wei et al., 2018).

Therefore, the anomaly of the peak at 4 nm needs to be ignored when discussing the characteristics of the PSD produced by the desorption curve (Fig. 16) (Ji et al., 2017; Wei et al., 2018).

#### 3.2.3. Random forest prediction model

As an integrated learning model with a complex structure and simple implementation, RF is a method that integrates many decision trees into forest for classification and regression (Breiman, 2001). The working principle of the RF algorithm is shown in Fig. 17. There is no correlation between RF decision trees, which were used as a model in bagging. The bagging is the presentation of the integration idea, and the RF method actually samples both specimens and their features, which can avoid overfitting. The bagging strategy is the main method in the prediction phase, and includes classified voting and mean value regression. The RF method has high tolerance for noise and outliers in data and can effectively address complex nonlinear interactions and evaluate the importance of each feature in classification problems. RF models show strong robustness and accuracy in dealing with complex data (Stumpf and Kerle, 2011). Based on the above advantages, this study used the RF model to evaluate and predict the PSDs of shale sediments. Geological factors including vitrinite reflectance ( $R_o$ ), TOC content, clay content, carbonate content, detrital content (sum of quartz and feldspar), sedimentary facies and kerogen type, were used as characteristic indicators to build the model in this study.

## 4. Results

### 4.1. Pore types in shale

The complex pore space in shale sediments contains various pores, generally dominated by organic pores inside OM and mineral-related pores (Chen et al., 2021; Hu et al., 2021a). According to their position, mineral matrix pores can be divided into interparticle pores and

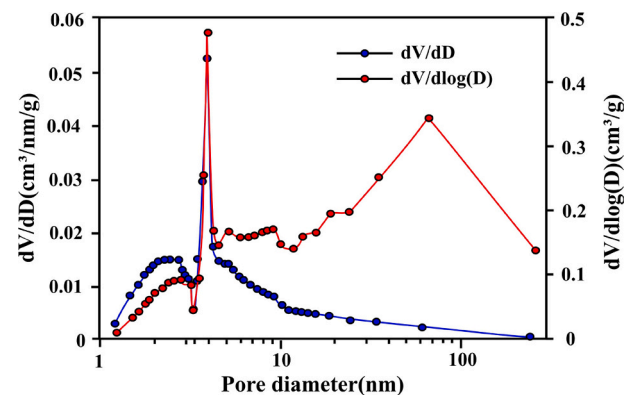


Fig. 16. Presentation of the artificial pores peak at approximately 4 nm at the PSD derived from  $N_2$  desorption branch of isotherms (Ji et al., 2017).

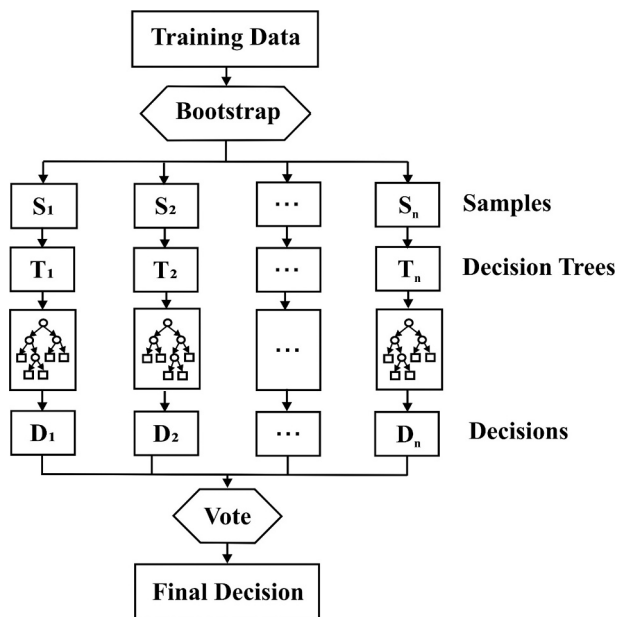


Fig. 17. Schematic diagram of the random forest process (Zhou et al., 2021).

intraparticle pores. Mineral-associated interparticle pores are classified as (1) inter-mineral pores between mineral particles (Fig. 18a and g); (2) OM-mineral interface pores between mineral particles and OM (Fig. 18b and h); and (3) clay-hosted pores between or within clay particles (Fig. 18c), including pores within clay-clasts. OM-mineral interface pores are considered as interparticle pores. However, intra-OM is appropriate where secondary pores within OM nucleate on mineral surfaces. Mineral-associated intraparticle pores within mineral grains are classified as following: (1) inclusion pores of equant shape are probably related to fluid inclusions (Fig. 18d); (2) intraskeletal pores (Fig. 18e); or (3) moldic pores where grains have been partially to fully dissolved (Fig. 18f). OM pores are secondary pores formed by the thermal evolution and hydrocarbon generation of the OM in the shale (Curtis et al., 2012a). OM pores can be divided into internal pores and marginal pores based on their location, which is dependent on the difference in their pathways of thermal evolution during hydrocarbon generation of various types of kerogen. Besides, the OM-hosted pores are abundant in all high-maturity shale (Ro of 1.2–1.3%), and are present in only minor volumes at low maturity (Ro about 0.5%).

#### 4.2. PSD characteristics and classification

The shale PSD obtained by the nitrogen adsorption method presents the volume occupied by pores with different diameters. The collected

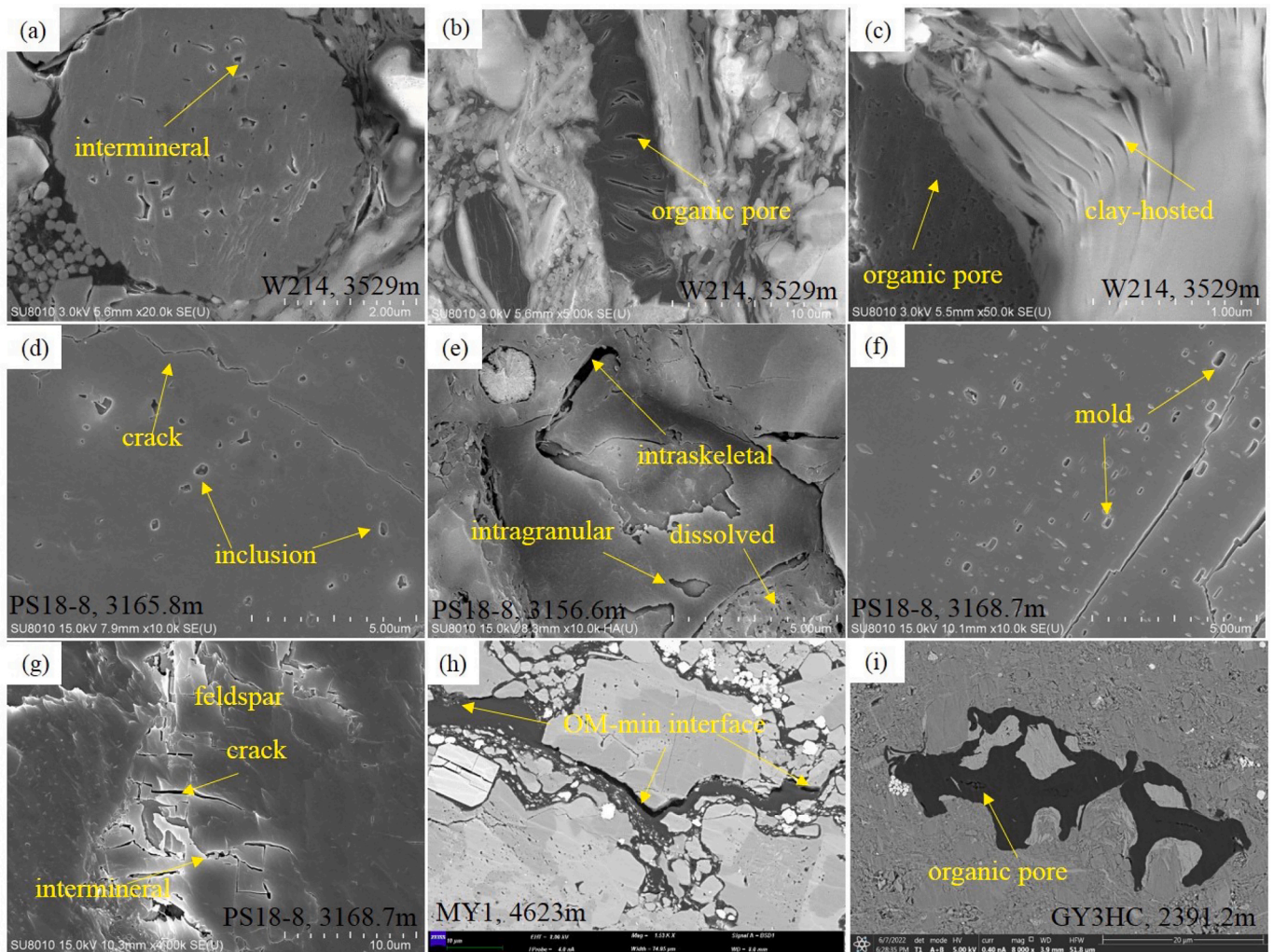


Fig. 18. Various pore space observed from SEM images in this study. (a–c) show the intermineral, organic, and clay related pores in lower Silurian Longmaxi shale of Sichuan Basin. (d–f) present the inclusion and mold pore space in the Eocene Shahejie shale of Bohai Bay Basin. (h) and (i) show the OM related pores in the Permian Fengcheng shale in the Junggar Basin and Cretaceous Gulung shale in the Songliao Basin.



PSDs of 240 shale samples are shown in Fig. 19. The shale pores are obviously dominated by micro-nanopores with the PSDs ranging from 2 to 100 nm. The variability of PSD reflects the great heterogeneity of the shale pore structure. However, the shale has own unique one or more major PSD intervals, showing a unimodal or multimodal distribution. The peak represents the pores of corresponding pore size interval taking the dominant proportion in the shale pore space.

The peak shape of PSD reflects the dominant pore size range, and the amplitude of the peak presets the amount of the pore space in the corresponding pore size. Based on the morphology, the PSDs of collected shales were divided into six types in this study (Fig. 20): Type I PSD is bimodal with the higher front peak, and the  $dV/d\log(D)$  ranges in 0–0.04 cc/g. The rear peak is relatively flat, mainly distributed at 100–200 nm. The dominate peak of type I is in the range of 1–5 nm, indicating that this type shale is dominated by micropores. Type II PSD mainly shows a unimodal distribution with a dominant pore size range of 50–100 nm, and the range of  $dV/d\log(D)$  varies in 0–0.018 cc/g. These features hint the macropores dominate the pore space in type II shale. Type III PSD is also mainly unimodal. The main pore size ranges from 2 to 8 nm, and the  $dV/d\log(D)$  is mainly in the range of 0–0.055 cc/g. The shale pore structure with type III PSD is relatively single and uniform, mainly composed of fine mesopores (Sing et al., 1985). The PSD of type IV is mainly bimodal, and its pore sizes are mainly distributed in the ranges of 2–5 nm and 20–80 nm. The  $dV/d\log(D)$  is distributed in the range of 0–0.12 cc/g, and the 20–80 nm pore space has a relatively larger  $dV/d\log(D)$  value than the 2–5 nm pore space. Type IV PSD is characterized by a low front peak and high back peak. These features indicate the shale with type IV PSD dominated by coarse mesopores to macropores. Type V PSD also presents an approximately bimodal morphology with major ranges of 2–5 nm and 20–50 nm. These two peaks are considerable and proportionable, and the  $dV/d\log(D)$  is in the range of 0–0.08 cc/g. It could be regarded as unimodal with broad distribution to a certain extent. And the pore structure of Type V PSD shale is complex, with high heterogeneity, mainly composed of mesopores. Type VI PSD is relatively scattered, with and low  $dV/d\log(D)$  value generally <0.01 cc/g, indicating that the pore structure of this type of shale is relatively heterogeneous. The pore diameters span different scales with small pore volume. The shale with type VI PSD has no obvious dominant pore space, meaning that it cannot provide preferential migration passage for fluid flow, which is disadvantageous for

shale oil and gas.

#### 4.3. Geological characteristics of different PSD types shale

Furthermore, the geological characteristics of different PSD types of shales are presented and contrasted in this study (Table. 1 and Fig. 21). The six types shales are developed in marine, marine-terrestrial transitional or continental sedimentary environments. Under the influence of the sedimentary environment, the composition exists considerable gulf among the six types of shales. A lot of previous studies show that the quartz, feldspar, carbonate and clay minerals, as well as the OM are the main composition in shale sediments (Mao and Guo, 2018; Xue et al., 2020; Hu et al., 2021b; Wang et al., 2022b).

As shown in Table 1 and Fig. 21, the type I shale has the highest quartz and feldspar contents with the average values of 32.72% and 16.14%, respectively, among these shales. The carbonate content in type I shale is the lowest (average of 12.17%). Type VI shale has the lowest quartz content (average of 21.47%), and a relatively high carbonate content (average of 28.24%). Clay is the most developed in type III shale, ranging from 15.00% to 87.00%, while feldspar is scarce, with the average value of 4.04%. Meanwhile, the clay content in type II shale varies from 3.00% to 62.90% with an average of 29.88%, which is lower than that in other shales. There is little difference in the content of quartz and carbonate minerals between type III and V shales. The content of clay minerals in type III shale is higher than that in type V shale, while its feldspar content is relatively low. Although these mineral compositions show obvious differences among these shales, the range of feldspar content is relatively concentrated in contrast to the scattered carbonate and clay.

The six types shales show distinct differences in TOC content. The type IV shale has the highest TOC content (average of 4.54%), followed by type I and II shales with semblable TOC contents with means of 3.44% and 3.40%. The TOC content in type III shale ranges from 0.20% to 7.00%, lower than that in type V (0.38–12.87%/2.60%) and VI (0.23–11.44%/3.27%) shales. In addition, the  $R_o$  values of the six types of shales show obvious differences. The  $R_o$  values of type I and IV shales are approximate, with average of 1.49% and 1.51%, respectively, higher than that in type III shale (average of 1.18%). Type V shale has the lowest  $R_o$  value (average of 0.75%), lower than that in type II and VI shales with average  $R_o$  values of 0.97% and 0.87%, respectively. Type I,

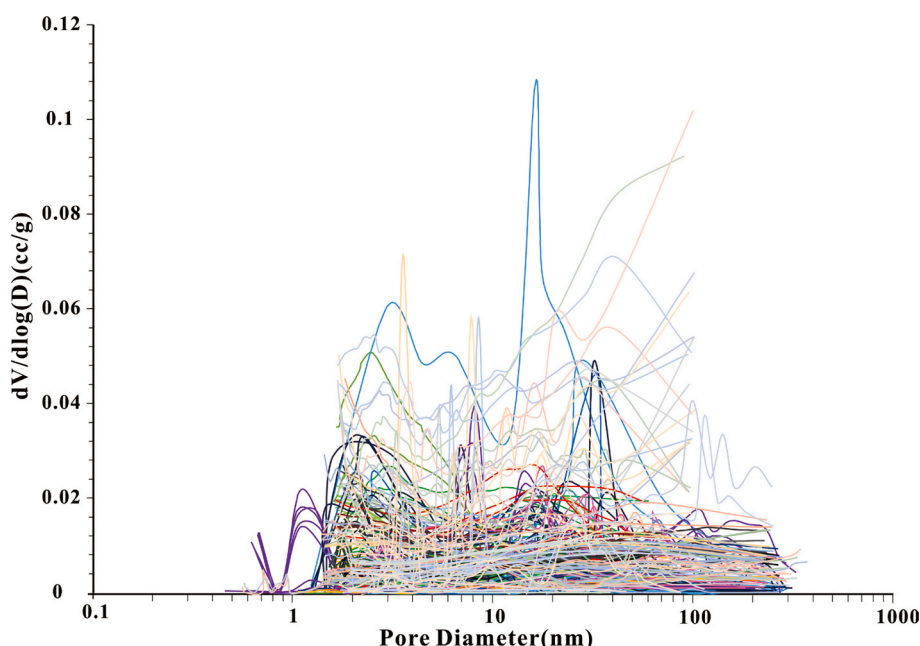


Fig. 19. Compilation diagram of shale pore size distribution.

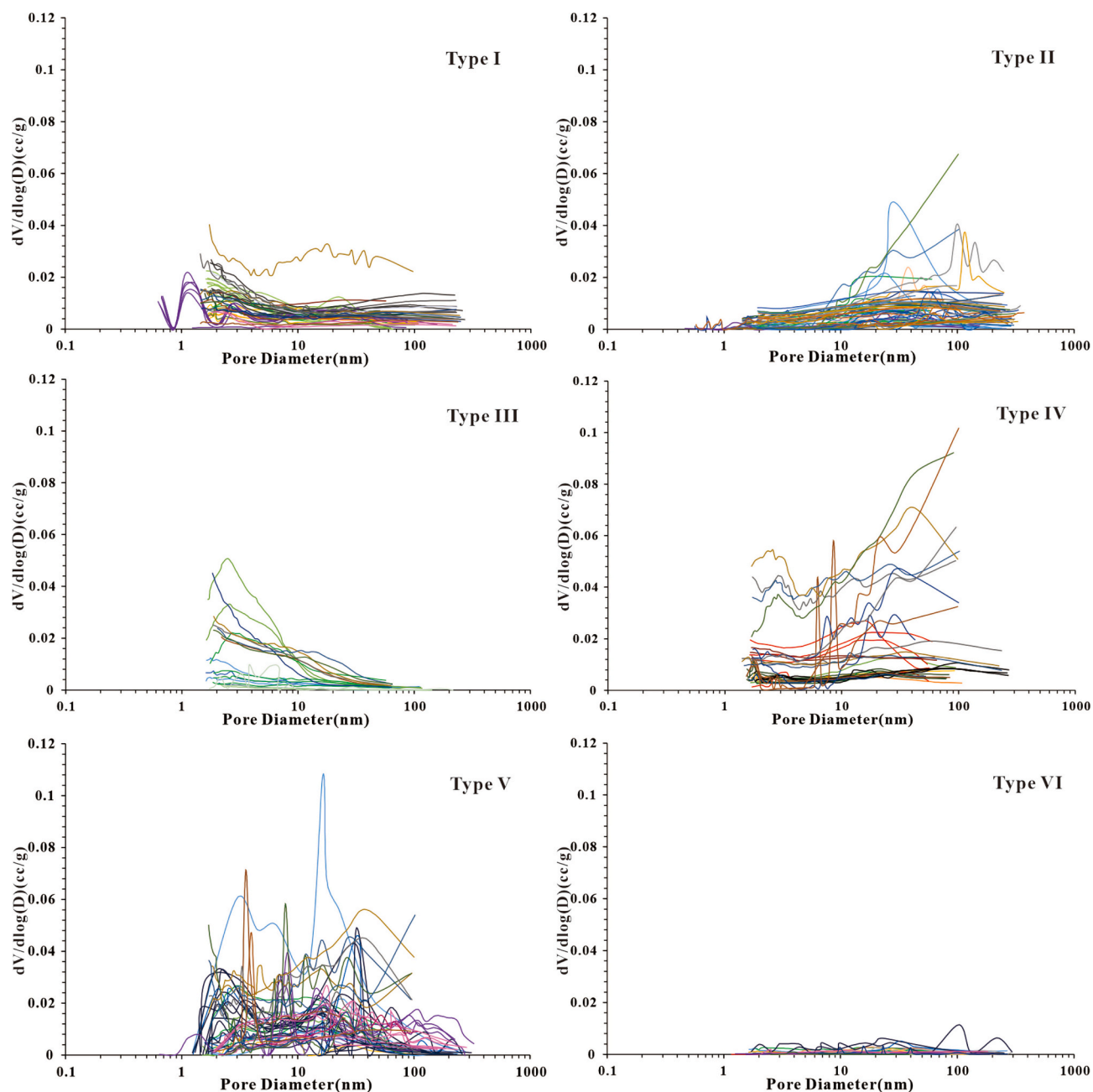


Fig. 20. The six classifications of shale sediments based on PSD features.

**Table 1**  
Geological characteristics of different shales.

	I	II	III	IV	V	VI
Sedimentary environment	Marine, marine-terrestrial transitional, lacustrine	Marine, lacustrine	Marine, marine-terrestrial transitional, lacustrine	Marine, marine-terrestrial transitional, lacustrine	Marine, marine-terrestrial transitional, lacustrine	Marine, marine-terrestrial transitional, lacustrine
Strata	$E_1/D_3/C_2/P/J_3-K_1/E_2$	$O/D_2/D_3-C_1/P_1/K_2/E_2$	$D_3/T_2-T_3/C_2-P_1/E_2$	$E_1/O_3/S_1/D_3/C_2/P/J_3-K_1/E_2$	$P_1/C/K/E_2$	$D_3/C_2/T/E_2$
Depth (m)	990.00–5193.70/2728.60	362.90–4226.80/2855.90	1087.00–5011.00/2958.70	975.00–4653.00/2538.60	1043.00–4215.30/2920.90	1119.00–4905.00/2549.80
Ro (%)	0.51–3.75/1.49	0.48–2.20/0.97	0.48–2.00/1.18	0.35–3.17/1.51	0.42–2.02/0.75	0.42–2.13/0.86
Kerogen Type	I/II/III	I/II/III	II/III	I/II/III	I/II/III	I/II/III
TOC (%)	0.18–7.97/3.44	0.84–11.20/3.40	0.20–7.00/2.32	0.50–15.90/4.54	0.38–12.87/2.60	0.23–11.44/3.27
Quartz (%)	11.00–63.08/32.72	0.63–80.08/31.89	7.20–41.80/25.10	7.80–51.50/34.14	9.20–54.00/25.29	3.20–38.57/21.47
Feldspar (%)	0.00–64.00/16.14	0.00–30.60/6.84	0.30–14.02/4.04	0.0026.40/7.48	0.00–27.90/9.49	0.50–24/9.12
Carbonate (%)	0.00–53.00/12.17	0.00–83.00/27.46	0.00–62.00/16.60	0.00–75.90/19.83	0.00–68.00/17.40	0.00–74.00/28.24
Clay (%)	2.00–65.60/32.43	3.00–62.90/29.88	15.00–87.00/46.87	1.20–59.10/33.29	16.00–56.00/37.37	6.00–85.00/35.99



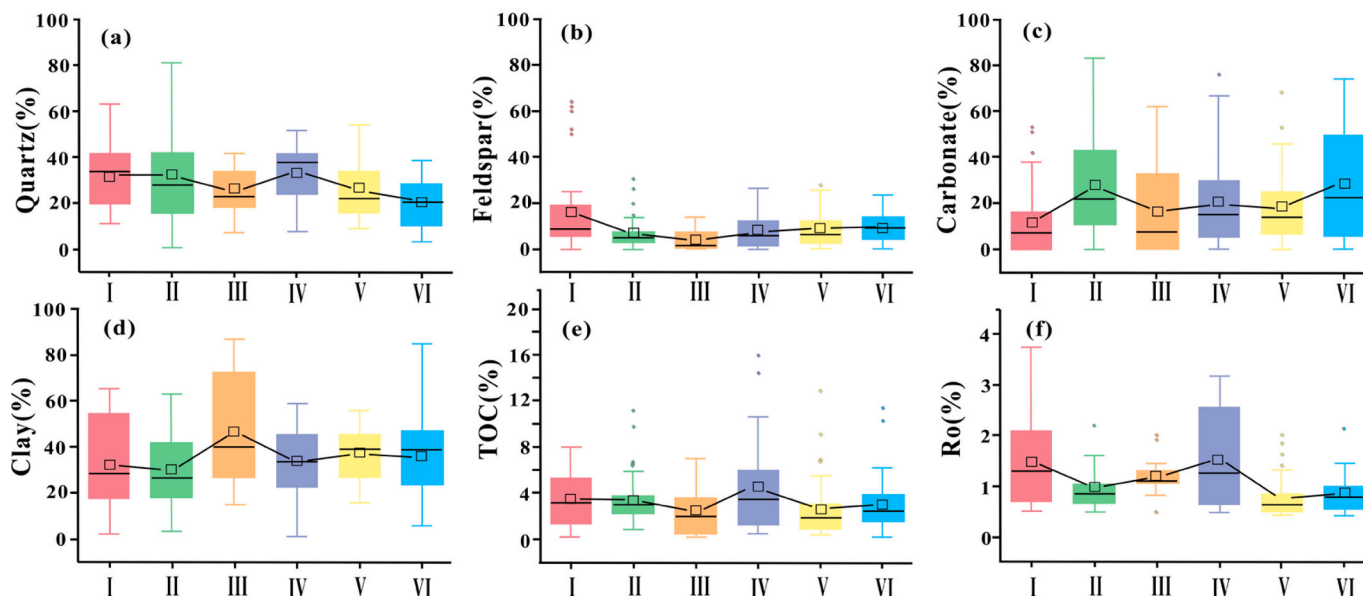


Fig. 21. The comparison of geological characteristics of different shales. The (a)-(f) show the difference of quartz, feldspar, carbonate, clay, TOC, Ro, respectively.

II, and III kerogens are widely developed in the six types of shales, showing weak differences among the shales.

#### 4.4. Random forest model

RF is a powerful method that uses multiple classification trees to distinguish and classify data. While classifying data, it can also give the importance score of each variable (gene) and evaluate the role of each variable in classification. To assess the importance of geological factors for each type of shale, the mean decrease accuracy and mean decrease Gini algorithm is used in this study. The importance of each factor has been assessed as shown in Fig. 22. The RF result shows that Ro is the most important contribution factor, with a score of 0.222, followed by TOC content (0.193) and clay content (0.169). The score of detrital content (0.140) is slightly higher than that of carbonate content (0.139). The higher feature importance indicates that the feature contributes

more in the classification of shale based on the PSD features. The sedimentary facies and kerogen type acquire the lowest scores  $<0.1$ , meaning that they have little differences among these six type shales. The evaluation results show that the Ro, TOC content and clay content have a more significant influence on the classification prediction modeling of shale sediments through PSD features. The sedimentary facies and organic matter type have relatively few contributions.

In order to evaluate the performance of the prediction model, the accuracy of the model and the confusion matrix of the test set were calculated as shown in Fig. 23. The overall accuracy of the RF model synthesizing the six classification is 75%. As shown in the test set confusion matrix heat map (Fig. 23b), the model accuracy of classification I is the highest with the value up to 80%, followed by classification II, III and V with the accuracy of 75%. The accuracy of classification IV is slight lower than that of classification II, III and V, but higher than that of classification VI. In conclusion, the RF prediction

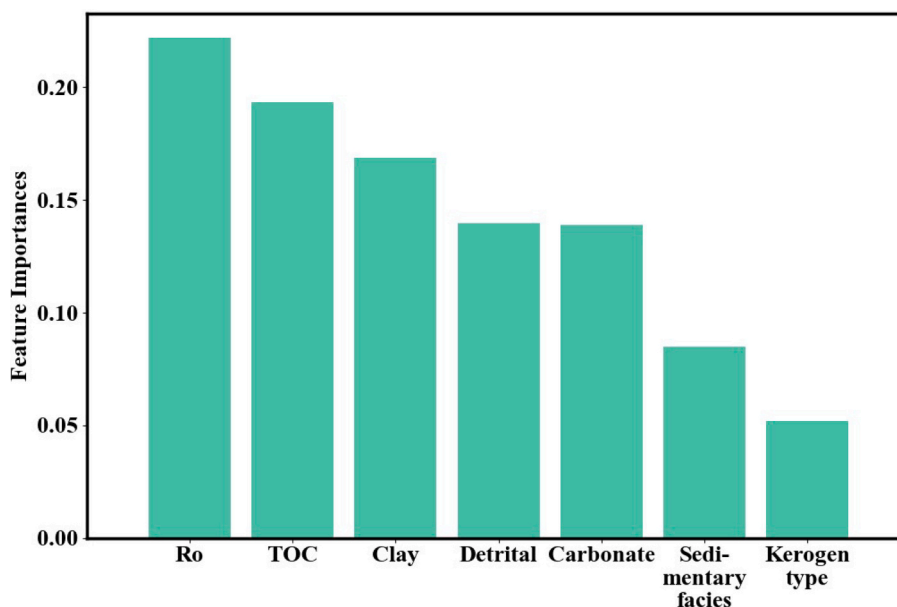


Fig. 22. the importance evaluation of geological features for shale classification by RF machine learning.

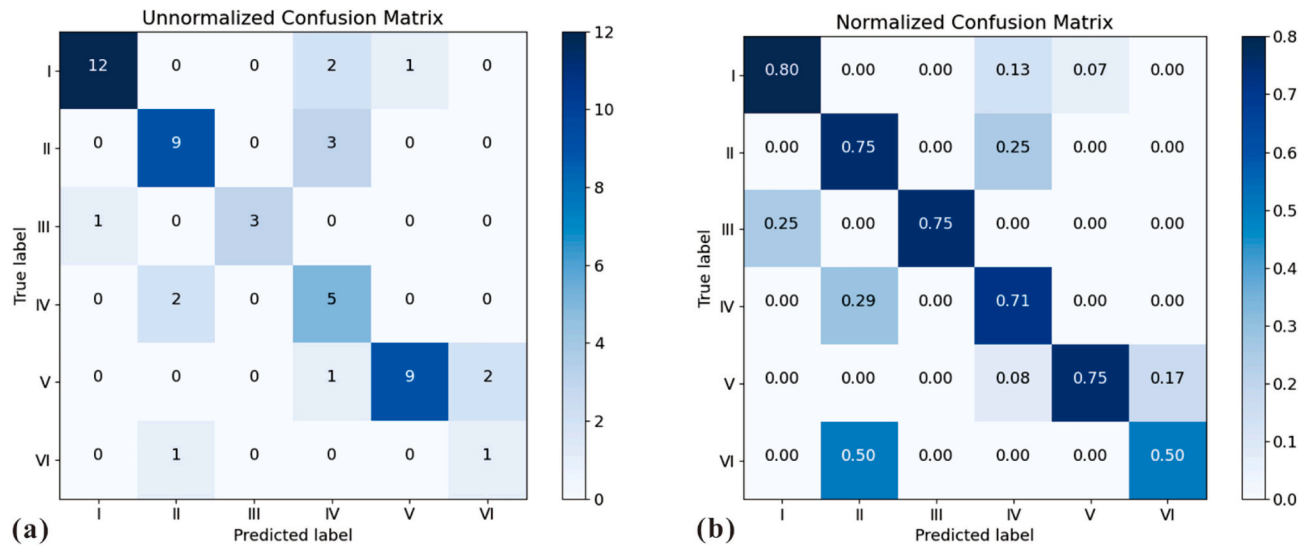


Fig. 23. (a) shows the test set confusion matrix and (b) present the normalized confusion matrix.

model of shale PSD classification is relatively reliable. An important factor affecting the accuracy is the size and imbalance of the data set. In this model, the categories with large data volume tend to have relatively better prediction results. And the model may be more accurate as the further improvement of the data set in the future.

## 5. Discussion

### 5.1. Factors affecting on the PSD

The complex pore structure of shale sediments is the comprehensive outcome of multiple geological factors. The main geological factors affecting the pore structure include  $R_o$ , mineral composition, TOC content, depositional environment, kerogen type, fluid-rock interactions, etc. Among them, the fluid-rock interactions are controlled by fluid properties, mineral properties, temperature and pressure

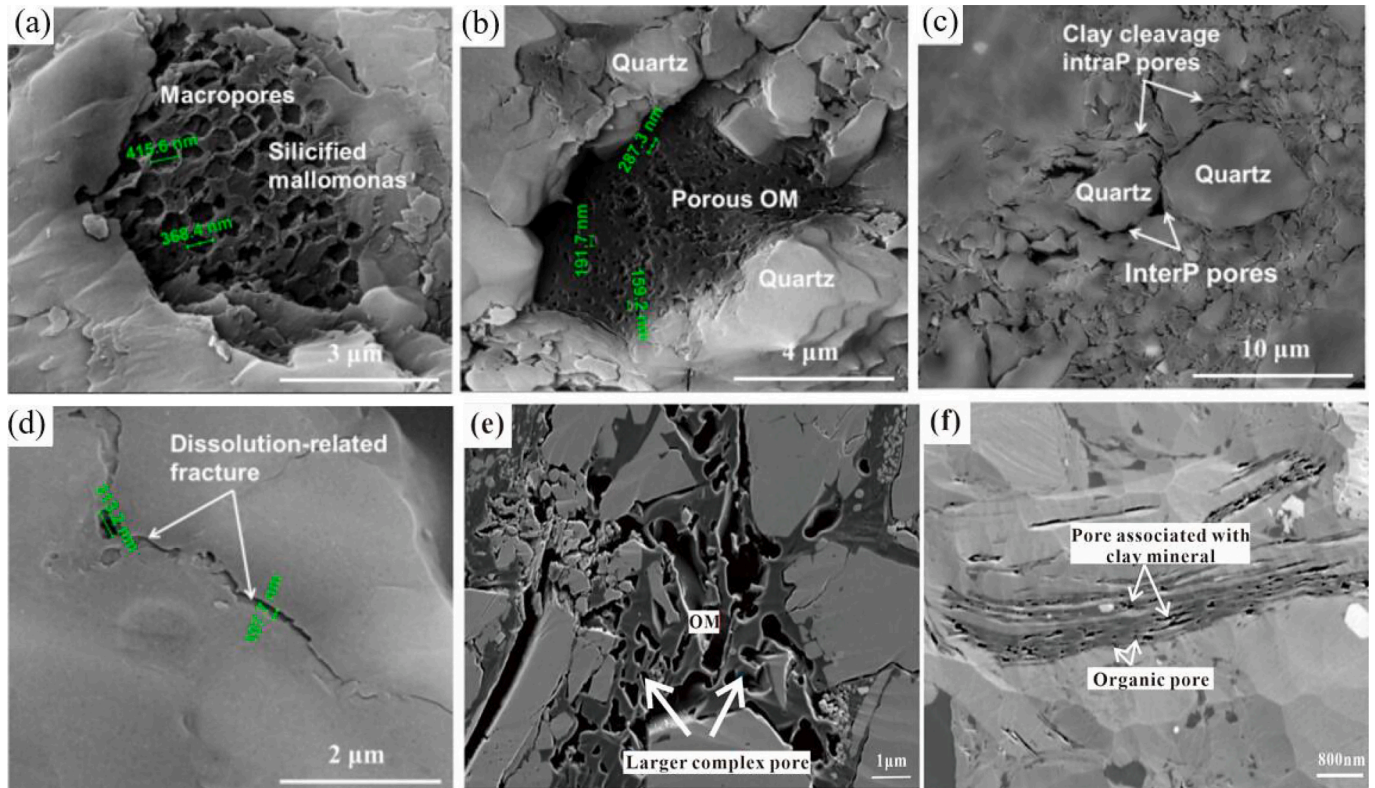


Fig. 24. (a) intergranular pores in silicified mallomonas (b) OMs with intraparticle porosity surrounded by quartz (c) intragranular pores and interparticle pores develop in pressure shadows of rigid grains (d) dissolution-related fracture in carbonate minerals (Yang et al., 2016c) (e) shows the interconnected combination of micropore to larger complex pores in large OM particles. (f) shows the organic-clay aggregates in the Shanxi Shale (Wei et al., 2018; Qiu et al., 2021).

conditions, etc., which are largely limited by the study area, and do not have global universality, with few data (Mastalerz et al., 2013; Liu et al., 2017a; Li et al., 2020; Wang et al., 2022a; Wang et al., 2022e; Zhou et al., 2020a; Zhang et al., 2022). On the other hand, since this paper mainly studies the influence of basic geological characteristics on pore structure, in order to establish a pore structure prediction model based on geological characteristics. Therefore, the factor of fluid and rock reaction was not input when building the prediction model. The statistical results show that the mineral composition, TOC content, and Ro have obvious influences on shale classification by PSD features, while the sedimentary environment and kerogen type contribute little.

### 5.1.1. Mineral compositions

The composition of shale has an important influence on its pore structure through various mechanisms (Li et al., 2016a; Xue et al., 2020). The sedimentary environments will lead to certain differences in composition and pore types of shale sediments (Mao and Guo, 2018). Numerous studies (Yang et al., 2016b; Yang et al., 2016c) have revealed that the pores of marine shale are mainly composed of clay mineral pores, skeleton mineral pores, microfossil intragranular pores and organic pores (Fig. 24). The organic pores could contribute approximately 62% of the total porosity in the Longmaxi marine shale, and skeleton mineral pores (quartz, feldspar, carbonate, etc.) and clay pores contribute 25% and 13%, respectively (Yang et al., 2016c). The rigid particles can prevent pore collapse and are beneficial to the preservation of organic and clay mineral-related pores (Fig. 25a), which are usually observed around rigid particles. The skeleton mineral related pores are mainly related to carbonate dissolution (Figs. 24 and 25c). Organic pores are dominated by nanoscale micropores (Fig. 25b), inducing widely unimodal PSD observed in the OM enriched shales (Fig. 26b). Meanwhile, the meso-macropore formed by the dissolution of carbonate minerals would present bimodal PSD in the carbonate-rich shale sediments (Fig. 26a) (Yang et al., 2016c).

The relatively frequent sea level changes bring strong heterogeneity of pore structure in the marine-terrestrial transitional shale sediments (Yang et al., 2017a; Mao and Guo, 2018). Previous studies have shown that inorganic pores dominate the marine-terrestrial transitional shale and are affected by mineral composition (Fig. 27) (Xue et al., 2020; Wang et al., 2022d). Inorganic pores are mostly mesopore and macropore. Argillaceous siltstone and silty mudstone are important types of marine-terrestrial transitional shale. The storage space in argillaceous siltstone dominated by siliceous minerals is mainly mineral matrix pores, including inorganic mineral intergranular pores and intragranular pores (Xue et al., 2020). Siliceous minerals have stronger supporting capacity than clay minerals and can reduce compaction damage (He, 2019). For silty mudstone with high content of clay minerals, its pore spaces are mainly organic and intergranular pores. The macropore, mesopore and micropore contribute similar pore volumes, and the pore structure is affected by the transformation among clay minerals. Kaolinite is easily transformed into chlorite with small SSA.

The conversion of montmorillonite to illite-smectite mixed layer will consume  $K^+$ , thereby promoting the dissolution of feldspar (Berger et al., 1997; Peltonen et al., 2009). More illite-smectite mixed layers can increase the mesopore volume, and a positive correlation between clay mineral content and pore volume is usually observed in silty mudstone. The influence of inorganic minerals on pore structure in silty mudstone is not obvious.

The lacustrine shale has more complex composition, and its pore types are mainly matrix related pores (Chen et al., 2015a; Jiang et al., 2016; Zhang et al., 2020a; Yang et al., 2021). The pore spaces in different lithofacies of lacustrine shale have significant differences (Shao et al., 2018; Li et al., 2020; Yang et al., 2021). Which are affected by compaction, composition, and thermal evolution (Peltonen et al., 2009; Zhou et al., 2020b; Gu et al., 2021). Before the middle stage of diagenesis, pore spaces are dominated by intergranular pores and clay-related pores. The intensity of compaction and the content of ductile minerals are the main factors affecting the pore structure (Berger et al., 1997; Peltonen et al., 2009; Zhou et al., 2020b). Siliceous and calcareous shales have large meso-macro pore volume, induced by inorganic pores with a diameter of tens of nanometers, including intergranular pores, intragranular pores, dissolution pores and intercrystalline pores. Correspondingly, mixed shale has the smallest mesopore volume, due to the developedly smaller clay interlayer pores and intergranular pores, as well as its strong compressibility (Zhang et al., 2020a; Gu et al., 2021). Authigenic analcime has a positive effect on the formation and preservation of micropores in calcareous shale and siliceous shale, and a negative effect on the micropores of mixed shale (Fig. 28) (Yang et al., 2021). The evolution of calcareous mineral-related pores is affected by thermal evolution and the interaction of minerals and fluids. The contribution of organic pores increases as the degree of thermal evolution increases, and is seriously affected by the organic-inorganic interactions. (Wu et al., 2012; Yang et al., 2013; Kennedy et al., 2014; Jiang et al., 2016; Mao and Guo, 2018; Gu et al., 2021).

### 5.1.2. Abundance of OM

OM is an important component of shale sediments, and affects the pore structure to a great extent (Li et al., 2020). Previous studies have revealed that the 0.34 nm pores formed in the aromatic rings combination of OM kerogen are an important part of micro-nano organic pores in shale sediments (Yang et al., 2019a; Yang et al., 2020). In addition, hydrocarbons are produced as the temperature increases during the OM burial process, accompanied by OM volume shrinkage and the generation of smaller internal pore spaces. Furthermore, a certain amount of organic acids produced in the process will corrode the materials and increase the pore space (Li et al., 2020). However, OM has strong compressibility and extensibility, and the pore spaces in high TOC shale is more easily compressed and reduction during burial.

The Late Permian Dalong marine shale in the Yangtze plate of East Asia has low thermal maturity, with Ro range of 0.60% - 0.81%, and it has similar PSD dominated by macropore space. The micropore in the

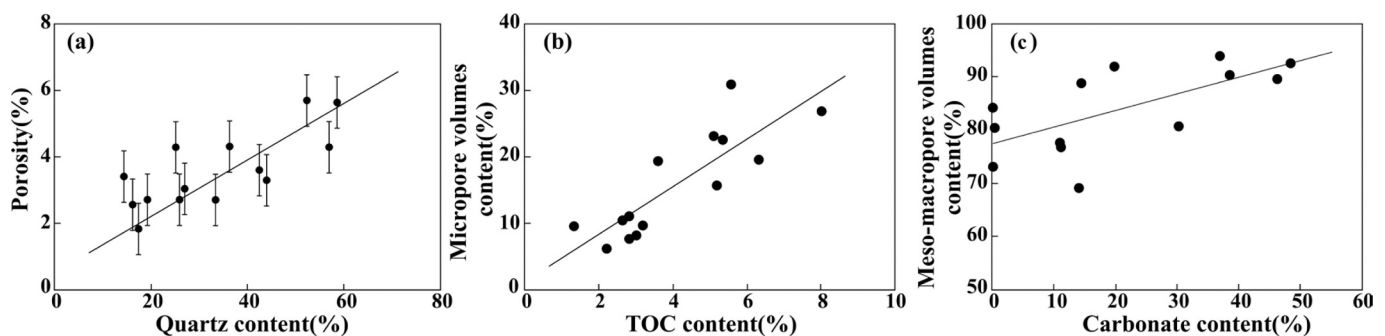


Fig. 25. the relationship between (a)quartz content and porosity (b)TOC and micropore volumes content (c)carbonate minerals content and meso-macropore volume content (Yang et al., 2016c).



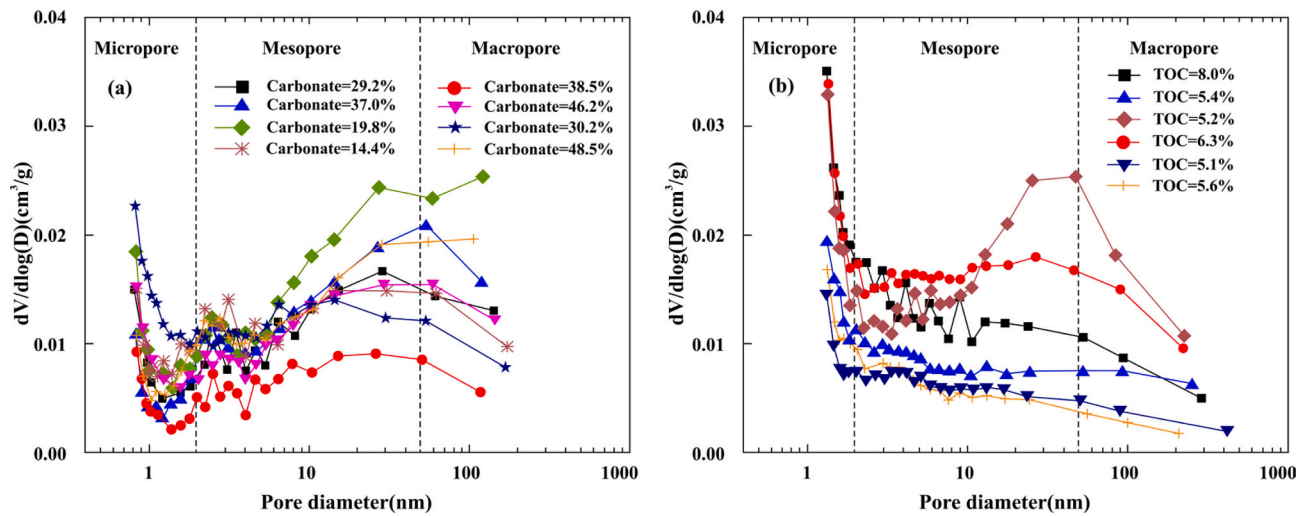


Fig. 26. PSD of shale samples derived from the  $N_2$  adsorption branch of the  $N_2$  isotherms by the BJH method (a) carbonate-rich samples (b) TOC-rich samples (Yang et al., 2016c).

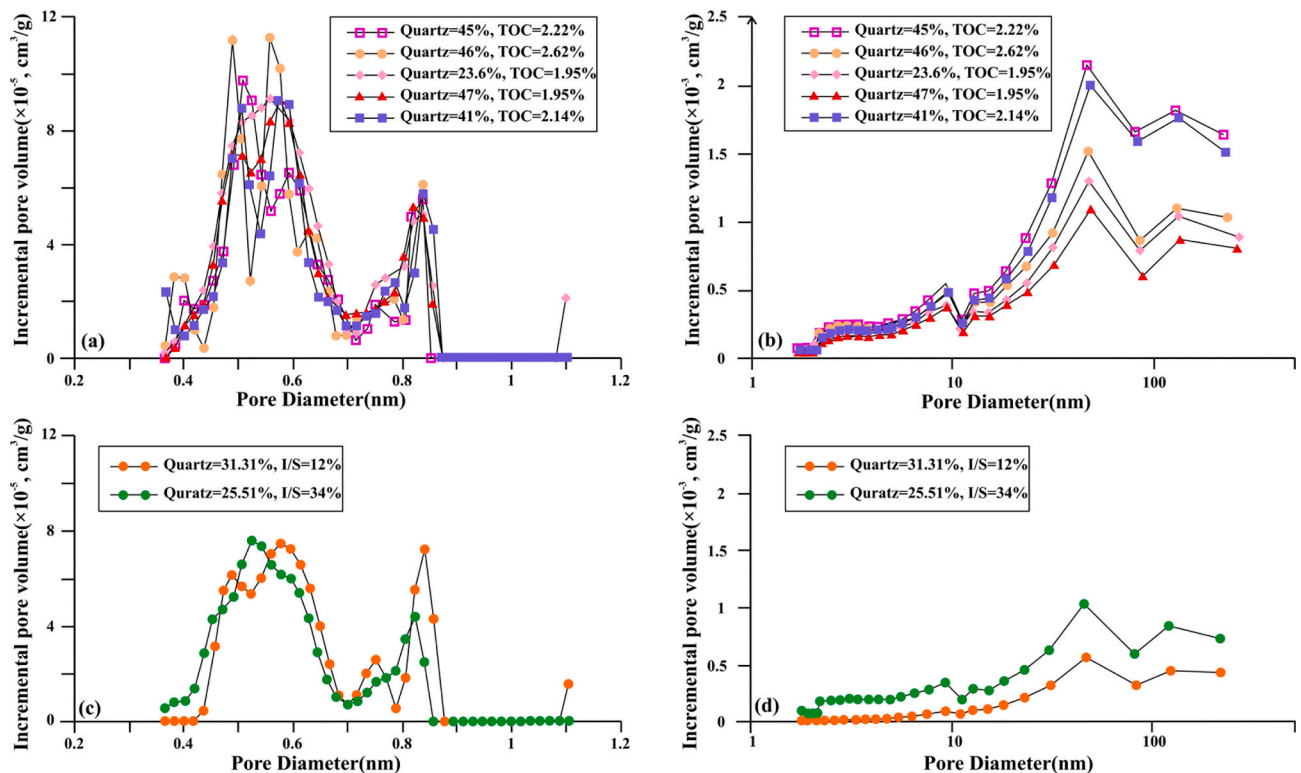


Fig. 27. (a) and (b) show the influence of siliceous content and OM content on the PSD of argillaceous siltstone. Illite-smectite mixed layer also has obvious effect on the PSD of the silty mudstone as shown in (c) and (d) (Xue et al., 2020).

Dalong shale is closely related to TOC content (Wei et al., 2018). Its corresponding PSD curve presents an overall downward trend with increasing TOC content (Fig. 30a), indicating that high TOC content inhibits the development of pore space at low maturity (Fig. 29a) (Wei et al., 2018). In addition, the interconnected combination of micropores during the thermal evolution process is another way to form larger complex pores in large OM particles (Fig. 24e) (Li et al., 2020). Therefore, the high TOC content may lead to a decrease of micropores and an increase of macropores in shale sediments (Figs. 29b, 30b and c), as well as the backward shift of PSD curve. However, this feature may differ from that in the marine-terrestrial transitional shale. Qiu et al., 2021

found that the micropore (PSD of 0.3–0.5 nm) dominated the pore structure in the Permian Shanxi marine-terrestrial transitional shale in the Ordos Basin with TOC content <2.00%. And the Shanxi shale with TOC content higher than 2.00% mainly dominated mesopore with relatively stable PSD (Fig. 30b and c).

In addition, shale sediment contains abundant clays, and its strong adsorption capacity facilitates OM enrichment and the organic-mineral interactions (Macquaker et al., 2010; Kennedy et al., 2014; Milliken et al., 2014; Pommer and Milliken, 2015). The association of OM and clay minerals will form new and more stable nanostructure of OM-clay aggregates (Fig. 24f), which promotes the decomposition of kerogen



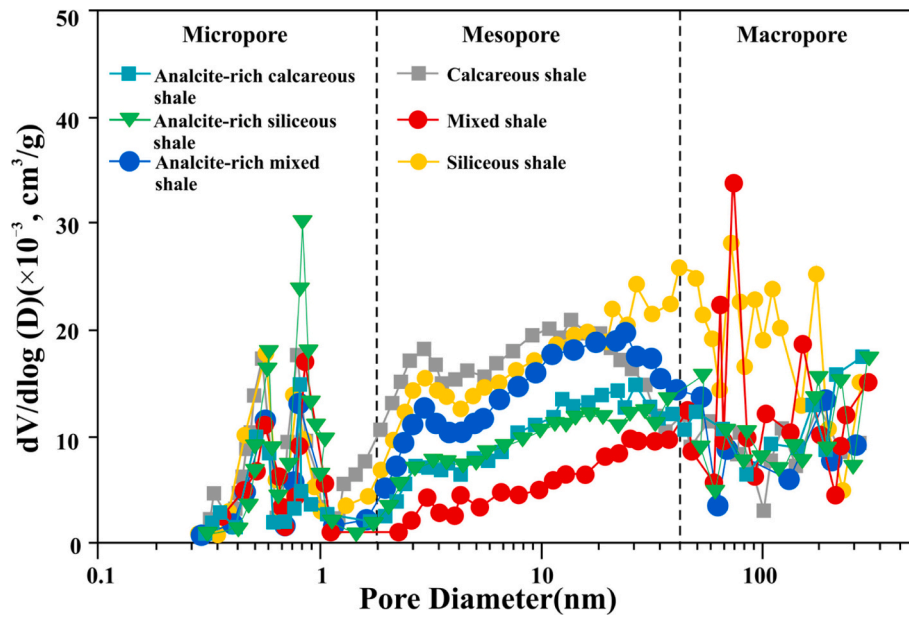


Fig. 28. PSD observed by the combination of CO<sub>2</sub> and N<sub>2</sub> physisorption tests for various shale (Yang et al., 2021).

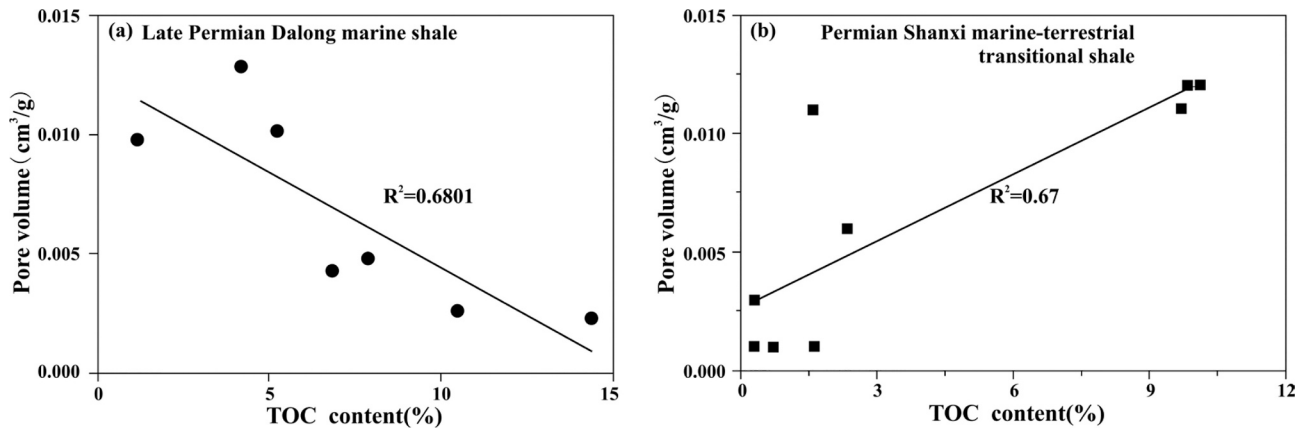


Fig. 29. The correlations of TOC content vs. PV in the Late Permian Dalong shale (a) and Permian Shanxi shale (b) (Wei et al., 2018; Qiu et al., 2021).

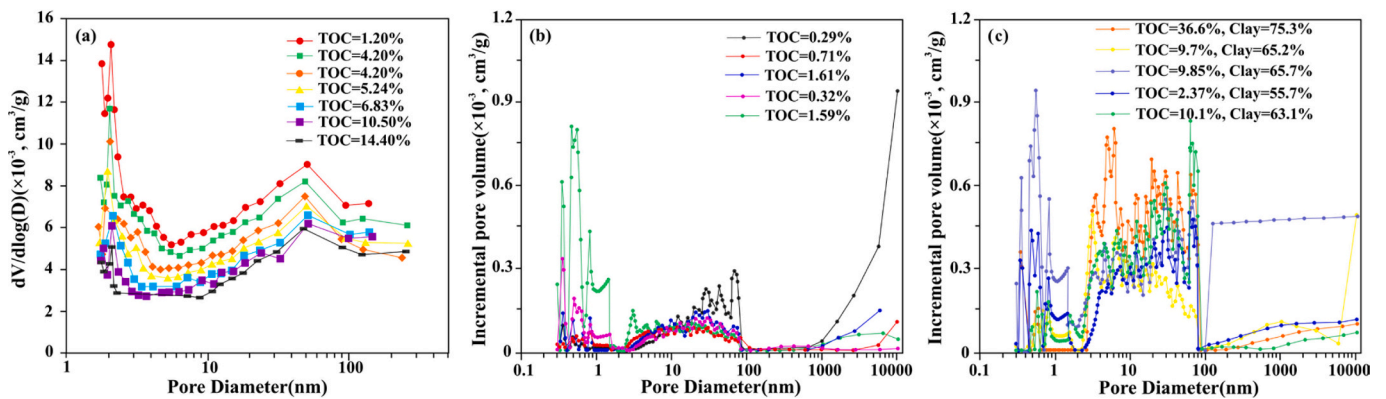


Fig. 30. (a) shows the PSD variation as TOC changes. The PSD difference in the shale with TOC < 2.00% (b) and > 2.00% (c) (Wei et al., 2018; Qiu et al., 2021).

(Kennedy et al., 2002). This complex process is OM-clay interaction function of degree (Zhu et al., 2018). Therefore, mesopore increase significantly with increasing TOC and clay (Fig. 30c). Of course, the small pores will be preferentially clogged and filled by the large particles

or the precipitable fluid during the hydrocarbon generation process (Li et al., 2016a).

### 5.1.3. Thermal maturity

Compared with the shale compositions, the OM thermal maturity has more obvious influences on the pore structure of shale sediments (Curtis et al., 2012a). Inorganic intergranular pores are the main contributor to pore space in low-mature shale, while organic pores dominate in high maturity shale. As the degree of thermal evolution further increases, the micropores will connect to form large and complex pores, which will affect the PSD.

The lacustrine shale in the Xingouzui Formation in the Jiangnan Basin has relatively low maturity ranging of 0.30% Ro–0.60% Ro with an average Ro value of 0.46%, and it contains many inorganic pores dominated by macropores (Li et al., 2016b). The Upper Jurassic Shahezi shale and Lower Cretaceous Yingcheng shale in the Songliao Basin shows that the OM transformation is the core factor affecting pore space evolution in lacustrine shale sediments (Zhou et al., 2020b). With increasing thermal maturity, the micropore, mesopore and macropore present a trend of decreasing first and then increasing, and a saltation at 1.30% Ro was observed (Fig. 31) (Zhou et al., 2020b). The early decline is caused by the filling of inorganic pores by crude oil, and the later enlargement trend is caused by the formation of organic pores (Zhou et al., 2020b).

As the thermal maturity increases to the pyrolysis gas stage, the organic pores will increase rapidly. However, because of the continuous increase of burial depth at this stage, the intergranular pores will be compressed in the plastic shale sediments enriched OM, which will offset the rapidly increasing organic pore space (Lee and Kim, 2019). Furthermore, the thermal simulation also reveals an overall upward trend of the PSD curve as the temperature increases (Sun et al., 2019). The PSD is basically unchanged from unheated to 250 °C (low maturity stage), increases rapidly at 250–400 °C (mature stage), and soars sharply at 400–500 °C (high maturity stage). These three stages correspond to the overhaul, formation and development phases of the pore system

(Fig. 32) (Sun et al., 2019).

### 5.1.4. Fluid-rock interactions

The interaction between rock and fluid is an important factor affecting the pore structure of shale. Clay minerals in shale will swell when exposed to water, which will block the pores space (Lahann et al., 2013; Lu et al., 2016; Yin et al., 2016). The weakly acidic fluid formed under the action of CO<sub>2</sub>–water interaction will cause mineral dissolution, leading to the change of shale pore structure. When shale is exposed to CO<sub>2</sub> and water environments, the porosity of shale will increase from 2.88% to 3.16% as the CO<sub>2</sub> pressure increases, and its connectivity is improved. The micropores and mesopores in shale gradually shift to macropores, and the heterogeneity of pore structure reduces with decreasing fractal dimension (Zhou et al., 2020a). Obviously, the effect of supercritical CO<sub>2</sub> (10 MPa, 14 MPa) on the pore structure is more significant than that of critical CO<sub>2</sub> (6 MPa) (Fig. 33).

In addition, the salting out of sedimentary water also affects the pore structure of shale. Especially for saline lake basins with salt development, the evaporation of salt minerals leads to the blockage of shale pores, affecting the pore structure (Scherer, 2004; Swpu, 2018; Zhang et al., 2019b). The brine evaporation experiment shows that salting out reduces matrix porosity by 23% and absolute permeability by 47% in the hypersaline lacustrine shale of the Qianjiang Formation in Jiangnan Basin (Zhang et al., 2022). Moreover, the salting-out leads to great changes of pore structure, with obvious left-shifting of the PSD (Fig. 34) (Zhang et al., 2022). This phenomenon shows that salt precipitation has a great influence on larger pores and reduces the heterogeneity of the shale pore structure to a certain extent.

### 5.2. Attentions about the random forest prediction model

The average accuracy of the prediction model generated by the RF

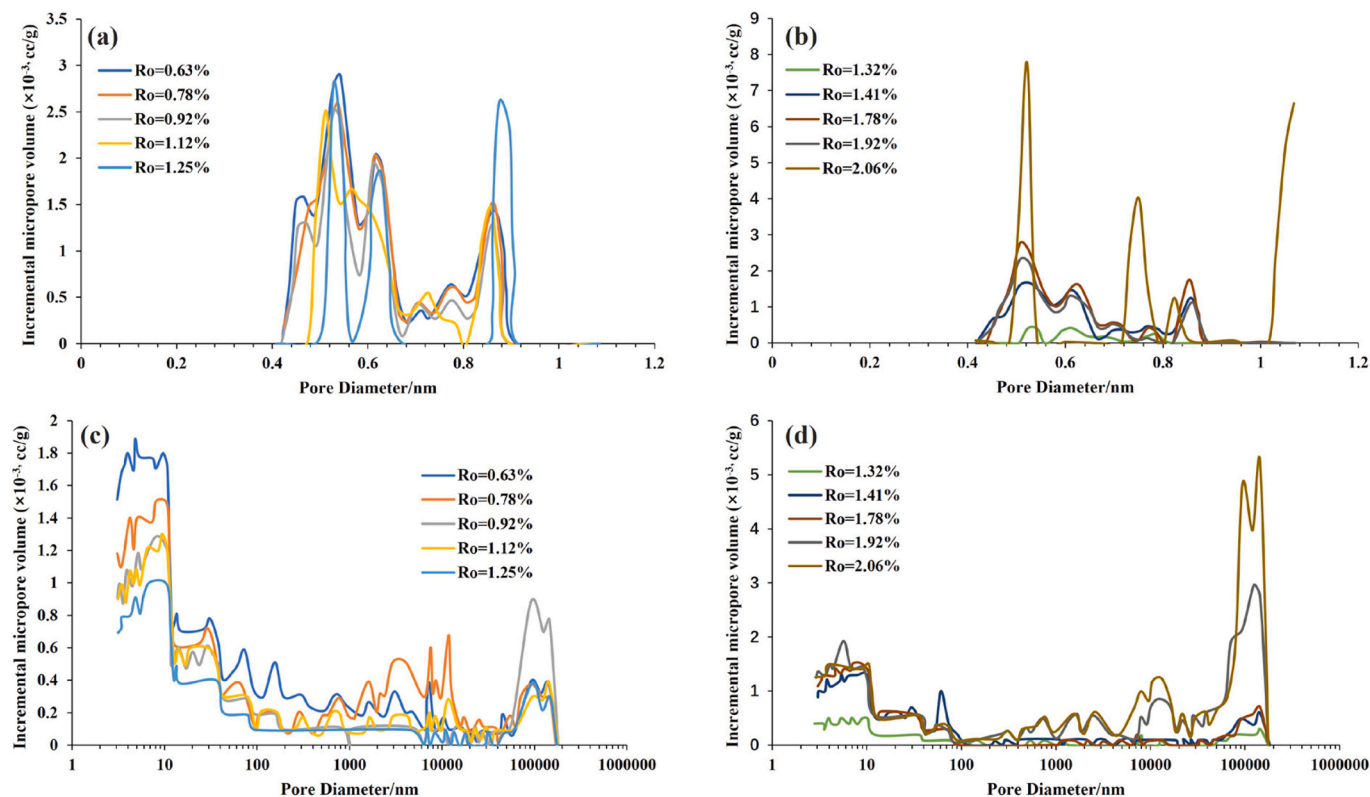


**Fig. 31.** The PSD variation in shale sediment follows its thermal maturity obtained from low-pressure CO<sub>2</sub> adsorption (a) and (b) and mercury intrusion (c) and (d). The Samples are from the Yingcheng Formation (K<sub>1</sub>y) and the underlying Shahezi Formation (K<sub>1</sub>sh) in the Songliao Basin, China. The largest micro-, meso- and macropore volume all occur in the least mature and in the most mature samples. The minimum micropore volumes exist in the status of 1.25%Ro and 1.32%Ro. While the minimum mesopore and macropore volume exist in the status of 1.32% Ro (Zhou et al., 2020b).

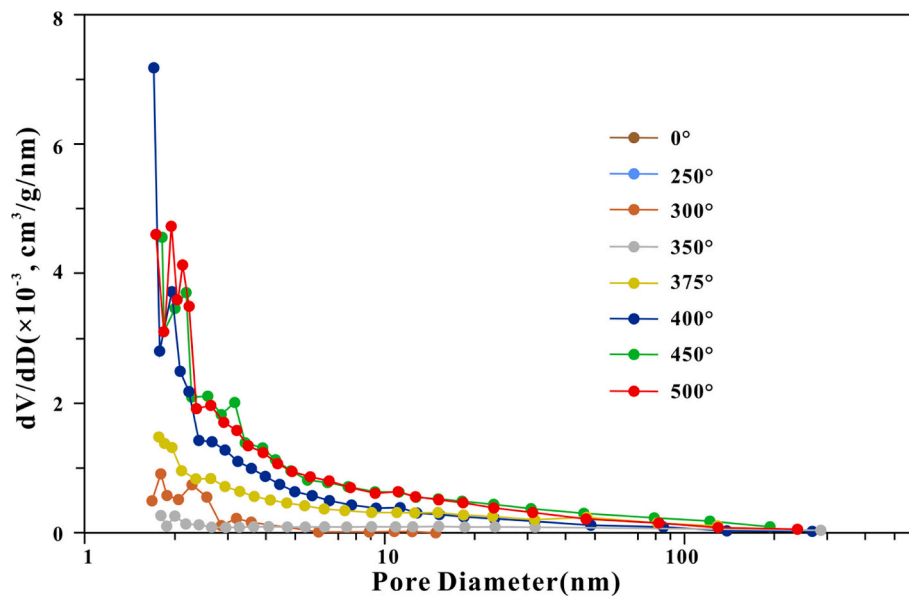


Fig. 32. PSD variations of shale with thermal maturity by thermal simulation experiment (Sun et al., 2019).

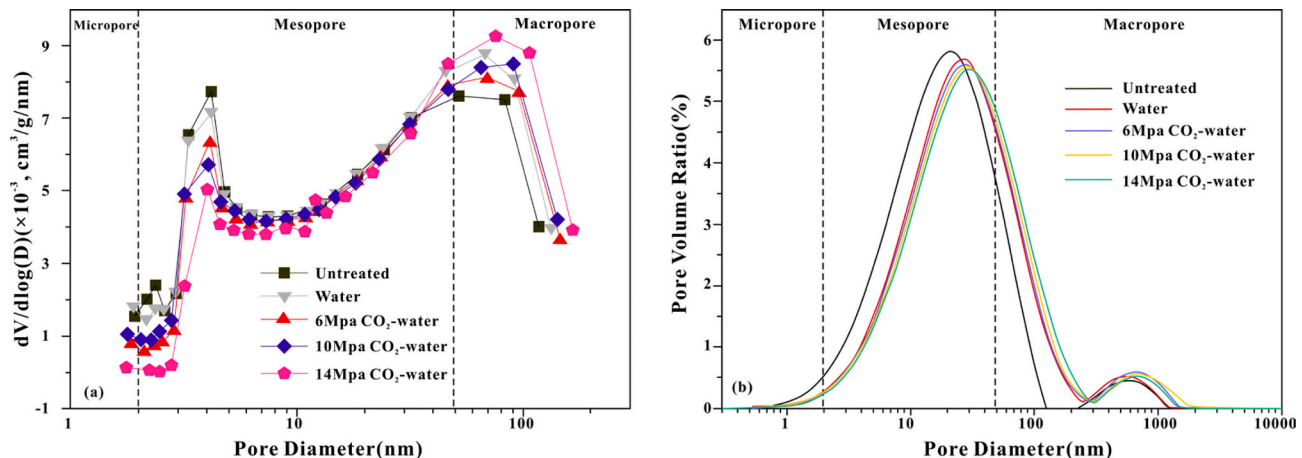


Fig. 33. The influence of CO<sub>2</sub>-water exposure on shale PSD obtained from N<sub>2</sub> adsorption (a) and NMR (b) methods (Zhou et al., 2020a).

method in this study is 75%. As shown in the normalized confusion matrix (Fig. 23), the types of I, II, III and V have the best performance in the RF prediction models, followed by types IV, and VI perform the worst. The data set with larger data volume more likely performs better than the data set with smaller data volume in the RF prediction model.

However, the effective data collected in this study is very limited, resulting in a large difference in the specimen size of different shale types, as well as the accuracy of <80% in the RF prediction model. However, this accuracy is sufficient to effectively predict the PSD type of shale sediment according to its geological characteristics. This study is a bold attempt, providing a new method for the fast prediction of shale pore structure based on geological analysis and ML to reduce cost.

Further research will focus on improving the quality of data sets and algorithm optimization to improve the accuracy of the model (He and Garcia, 2009; Seiffert et al., 2010; Ma et al., 2022). Specifically, the quality of the data set can be improved by increasing the sample size to solve the problem of data set imbalance and the overall sample size is too small; and the algorithm can be optimized by combining with other algorithms to better alleviate the problems caused by unbalanced data sets (Ma et al., 2022). We believe that the expansion of data volume, the optimization of algorithms and the establishment of data cleaning standards in the field of oil and gas exploration are the directions to

improve the accuracy of the model.

## 6. Conclusions

The rapid development of shale oil and gas promotes the rapid development of shale pore structure characterization and accumulates a considerable amount of data about different shales and their pore structure. While, a lot of repeated work in this field present similar pore structure. These works are lack of summary, resulting in a large waste of research time and money. This study reviewed pore structure systematics in marine, marine-terrestrial transitional and continental shale of all key formations and ages. In addition, we investigated the characteristics of pore structure in shale sediments with different geological conditions. We emphasis on the classification of PSD in shale sediments and the influence of geological factors on the PSD types. The PSD of shale is classified into six types based on the morphological characteristics, which show obvious differences in the shale compositions and thermal maturity. The RF ML further shows that thermal maturity has the greatest effect on the PSD classification, followed by TOC content and mineral composition.

Thermal maturation affects the pore structure of pore types and PSD. The high thermal maturation facilitates the generation of organic pores



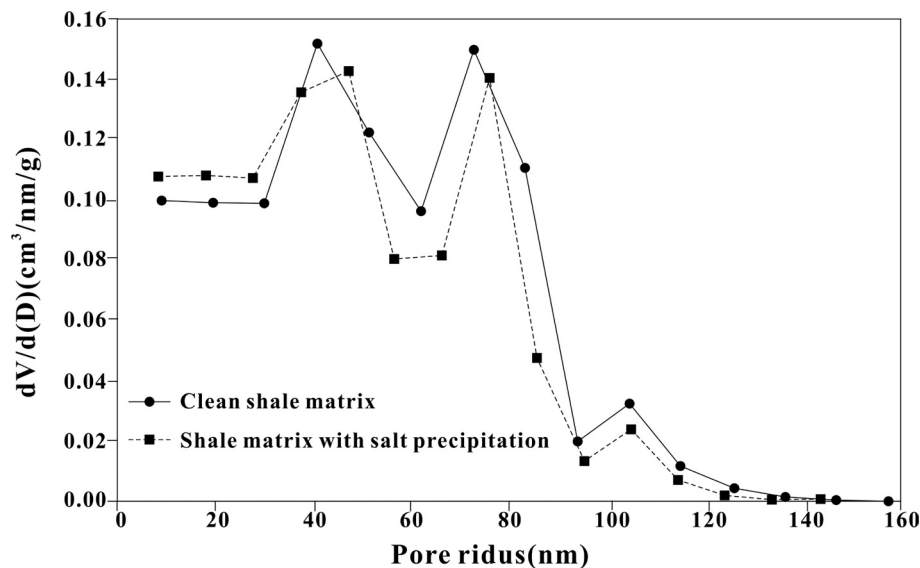


Fig. 34. Salt precipitation affects the change of shale PSD (Zhang et al., 2022).

and the connection of micro-nano micropores to larger pores. In addition, the diagenesis related to thermal maturation will also affect the pore types, especially the dissolution of organic acids formed during hydrocarbon generation, which will form dissolution pores. The OM and minerals in shale affect the shape and type of pores, which are the basis of the pore structure. The TOC content has two negative effects on the shale pore structure. The high TOC content avails to the formation of more micro-nano micropores during the process of hydrocarbons generation. While, the strong plasticity of OM will lead to pore space collapse. Mineral composition mainly affects the pore structure of pore types. Quartz and feldspar are mainly intergranular pores with a few fractures developed. The dissolution pores are mostly developed in carbonate minerals. Interlayer pores are frequently developed in clay minerals. Based on the evaluation from RF ML, we suggest that the sedimentary environment and the OM types have little influence on the shale pore structure than other factors.

Moreover, we proposed a RF machine learning model to forecast the PSD type of shale sediments through the geological conditions. Through the prediction model proposed in this paper, the simple prediction of PSD classification can be implemented quickly and efficiently by inputting only basic geological parameters common in shale research such as mineral content, Ro, TOC content, sedimentary facies and kerogen type of shale samples, which means that pore structure analysis can be realized without additional expensive, time-consuming, and environmentally unfriendly pore characterization experiments. The proposed model based on RF can determine the factors most closely affecting the pore structure, and can quickly obtain the pore structure characteristics of shale samples. This model has guiding significance for geologists to study oil and gas occurrence and flow space of shale sediments, as well as subsequent exploration and production. The supplement of dataset and improvement of algorithm in the further study are the key directions for us to enhance the accuracy of the prediction model and optimize the model.

#### Declaration of Competing Interest

The authors declare that they have no known competing financial interests or personal relationships that could have appeared to influence the work reported in this paper.

#### Data availability

I have uploaded my data and code files at the Attach File step.

#### Acknowledgments

This work was supported by the National Natural Science Foundation of China (NSFC) (41872128), and China Postdoctoral Science Foundation (2022M723487). The opinions expressed in this paper are those of the authors. The insightful reviews by the reviewers significantly improved the manuscript, for which we are grateful.

#### Appendix A. Supplementary data

Supplementary data to this article can be found online at <https://doi.org/10.1016/j.earscirev.2023.104442>.

#### References

- Adeyilola, A., Nordeng, S., Onwumelu, C., Nwachukwu, F., Gentzis, T., 2020. Geochemical, petrographic and petrophysical characterization of the Lower Bakken Shale, Divide County, North Dakota. *Int. J. Coal Geol.* 224 <https://doi.org/10.1016/j.coal.2020.103477>.
- Anderson, T., 2014. Key parameters for liquid-rich unconventional plays: case studies from North America. *AAPG Search Discov.* Article 80354 (80354), 34. <https://www.searchanddiscovery.com/abstracts/html/2014/90186gtw/abstracts/deo.htm>.
- Anovitz, L.M., Cole, D.R., Rother, G., Allard, L.F., Jackson, A.J., Littrell, K.C., 2013. Diagenetic changes in macro-to nano-scale porosity in the St. Peter Sandstone: an (ultra) small angle neutron scattering and backscattered electron imaging analysis. *Geochim. Cosmochim. Acta* 102, 280–305. <https://doi.org/10.1016/j.gca.2012.07.035>.
- Anovitz, L.M., Cole, D.R., 2015. Characterization and Analysis of Porosity and Pore Structures. *Rev. Mineral. Geochem.* 80 (1), 61–164. <https://doi.org/10.2138/rmg.2015.80.04>.
- Anovitz, L.M., Cole, D.R., Jackson, A.J., Rother, G., Littrell, K.C., Allard, L.F., Pollington, A.D., Wesolowski, D.J., 2015. Effect of quartz overgrowth precipitation on the multiscale porosity of sandstone: a (U) SANS and imaging analysis. *Geochim. Cosmochim. Acta* 158, 199–222. <https://doi.org/10.1016/j.gca.2015.01.028>.
- Anovitz, L.M., Lynn, G.W., Cole, D.R., Rother, G., Allard, L.F., Hamilton, W.A., Porcar, L., Kim, M.-H., 2009. A new approach to quantification of metamorphism using ultra-small and small angle neutron scattering. *Geochim. Cosmochim. Acta* 73 (24), 7303–7324. <https://doi.org/10.1016/j.gca.2009.07.040>.
- Bai, B., Elmagati, M., Zhang, H., Wei, M., 2013a. Rock characterization of Fayetteville shale gas plays. *Fuel* 105, 645–652. <https://doi.org/10.1016/j.fuel.2012.09.043>.
- Bai, B., Zhu, R.K., Wu, S.T., Yang, W.J., Zhang, X.X., Su, L., 2013. Multi-scale method of nano(micro)-CT study on microscopic pore structure of tight sandstone of Yanchang Formation, Ordos Basin. *Petrol. Explor. Dev.* 40 (3), 354–358. [https://doi.org/10.1016/S1876-3804\(13\)60042-7](https://doi.org/10.1016/S1876-3804(13)60042-7).
- Bakke, S., Øren, P.-E., 1997. 3-D pore-scale modelling of sandstones and flow simulations in the pore networks. *SPE J.* 2 (02), 136–149. <https://doi.org/10.2118/35479-PA>.
- Bangert, P. (Ed.), 2021. *Machine Learning and Data Science in the Oil and Gas Industry: Best Practices, Tools, and Case Studies*. Gulf Professional Publishing, Cambridge, MA Oxford.
- Berger, G., Lachapagne, J.-C., Velde, B., Beaufort, D., Lanson, B., 1997. Kinetic constraints on illitization reactions and the effects of organic diagenesis in

- sandstone/shale sequences. *Appl. Geochem.* 12 (1), 23–35. [https://doi.org/10.1016/S0883-2927\(96\)00051-0](https://doi.org/10.1016/S0883-2927(96)00051-0).
- Bernard, S., Horsfield, B., 2014. Thermal maturation of gas shale systems. *Annu. Rev. Earth Planet. Sci.* 42, 635–651. <https://doi.org/10.1146/annurev-earth-060313-054850>.
- Bernard, S., Wirth, R., Schreiber, A., Schulz, H.-M., Horsfield, B., 2012. Formation of nanoporous pyrobitumen residues during maturation of the Barnett Shale (Fort Worth Basin). *Int. J. Coal Geol.* 103, 3–11. <https://doi.org/10.1016/j.coal.2012.04.010>.
- Bloch, F., 1946. Nuclear induction. *Phys. Rev.* 70 (7–8), 460. <https://doi.org/10.1103/PhysRev.70.460>.
- Breiman, L., 2001. Random Forests. *Mach. Learn.* 45, 5–32. <https://doi.org/10.1023/A:1010933404324>.
- Broekhoff, J., 1967. Studies on pore systems in catalysts IX. Calculation of pore distributions from the adsorption branch of nitrogen sorption isotherms in the case of open cylindrical pores a. Fundamental equations. *J. Catal.* 9 (1), 8–14. [https://doi.org/10.1016/0021-9517\(67\)90174-1](https://doi.org/10.1016/0021-9517(67)90174-1).
- Bruening, F.A., Cohen, A.D., 2005. Measuring surface properties and oxidation of coal macerals using the atomic force microscope. *Int. J. Coal Geol.* 63 (3–4), 195–204. <https://doi.org/10.1016/j.coal.2005.01.001>.
- Bryant, S.L., King, P.R., Mellor, D.W., 1993. Network model evaluation of permeability and spatial correlation in a real random sphere packing. *Transp. Porous Media* 11 (1), 53–70. <https://doi.org/10.1007/bf00614635>.
- Bustin, R.M., Bustin, A.M., Cui, A., Ross, D., Pathi, V.M., 2008. Impact of shale properties on pore structure and storage characteristics. In: *SPE Shale Gas Production Conference*. OnePetro. <https://doi.org/10.2118/119892-MS>.
- Cao, T.T., Song, Z.G., Liu, G.X., Yin, Q., Luo, H.Y., 2016. Characteristics of shale pores, fractal dimension and their controlling factors determined by nitrogen adsorption and mercury injection methods. *Petrol. Geol. Recov. Effic.* 23 (2), 1–8 (in Chinese with English Abstract).
- Cavelan, A., Boussafir, M., Mathieu, N., Laggoun-Defarge, F., 2020. Impact of thermal maturity on the concomitant evolution of the ultrafine structure and porosity of marine mudstones organic matter; contributions of electronic imaging and new spectroscopic investigations. *Int. J. Coal Geol.* 231 <https://doi.org/10.1016/j.coal.2020.103622>.
- Cavelan, A., Boussafir, M., Rozenbaum, O., Laggoun-Defarge, F., 2019. Organic petrography and pore structure characterization of low-mature and gas-mature marine organic-rich mudstones: Insights into porosity controls in gas shale systems. *Mar. Pet. Geol.* 103, 331–350. <https://doi.org/10.1016/j.marpetgeo.2019.02.027>.
- Cazorla-Amorós, D., Alcaniz-Monge, J., Linares-Solano, A., 1996. Characterization of activated carbon fibers by CO<sub>2</sub> adsorption. *Langmuir* 12 (11), 2820–2824. <https://doi.org/10.1021/la960022s>.
- Chalmers, G.R., Bustin, R.M., Power, I.M., 2012. Characterization of gas shale pore systems by porosimetry, pycnometry, surface area, and field emission scanning electron microscopy/transmission electron microscopy image analyses: examples from the Barnett, Woodford, Haynesville, Marcellus, and Doig units. *AAPG Bull.* 96 (6), 1099–1119. <https://doi.org/10.1306/10171111052>.
- Chalmers, G.R.L., Bustin, R.M., 2008. Lower cretaceous gas shales in northeastern British Columbia, part I: geological controls on methane sorption capacity. *Bull. Can. Petrol. Geol.* 56 (1), 1–21. <https://doi.org/10.2113/gscpgbull.56.1.1>.
- Chandra, D., Vishal, V., 2021. A critical review on pore to continuum scale imaging techniques for enhanced shale gas recovery. *Earth Sci. Rev.* 217 <https://doi.org/10.1016/j.earscirev.2021.103638>.
- Chandra, D., Vishal, V., Bahadur, J., Agrawal, A.K., Das, A., Hazra, B., Sen, D., 2022. Nano-scale physicochemical attributes and their impact on pore heterogeneity in shale. *Fuel* 314. <https://doi.org/10.1016/j.fuel.2021.123070>.
- Chen, D., Pang, X.Q., Jiang, F.J., Liu, G.Y., Pan, Z.H., Liu, Y., 2021. Shale Oil potential and Mobility of Low-Maturity Lacustrine Shales: Implications from NMR Analysis in the Bohai Bay Basin. *Energ. Fuel* 35 (3), 2209–2223. <https://doi.org/10.1021/acs.energyfuels.0c03978>.
- Chen, S.R., Shuai, Q., Gao, Q., Tian, Y., Xu, R.J., Huang, Y.J., 2015a. Analysis of the pore structure of shale in Ordos Basin by SEM with nitrogen gas adsorption-desorption. *Rock Miner. Anal.* 34 (6), 636–642 (in Chinese with English Abstract).
- Chen, Y., Wei, L., Mastalerz, M., Schimmelpenninck, A., 2015b. The effect of analytical particle size on gas adsorption porosimetry of shale. *Int. J. Coal Geol.* 138, 103–112. <https://doi.org/10.1016/j.coal.2014.12.012>.
- Chilingar, G.V., Mannon, R.W., Rieke, I., 1972. *Oil and gas production from carbonate rocks*. Medium: X; Size: Pages, 408. American Elsevier Publishing Company Inc, New York, United States, 2011-2003-2024 pp.
- Clarkson, C.R., Solano, N., Bustin, R.M., Bustin, A.M.M., Chalmers, G.R.L., He, L., Melnichenko, Y.B., Radlinski, A.P., Blach, T.P., 2013. Pore structure characterization of north american shale gas reservoirs using USANS/SANS, gas adsorption, and mercury intrusion. *Fuel* 103, 606–616. <https://doi.org/10.1016/j.fuel.2012.06.119>.
- Cnudde, V., Boone, M.N., 2013. High-resolution X-ray computed tomography in geosciences: a review of the current technology and applications. *Earth Sci. Rev.* 123, 1–17. <https://doi.org/10.1016/j.earscirev.2013.04.003>.
- Coates, G.R., Xiao, L., Prammer, M., 1999. *NMR logging: Principles and applications*. Halliburton Energy Services, Houston.
- Comerio, M., Fernandez, D.E., Rendtorff, N., Cipollone, M., Zalba, P.E., Pazos, P.J., 2020. Depositional and postdepositional processes of an oil-shale analog at the microstructure scale: the lower cretaceous Agrio Formation, Neuquen Basin, northern Patagonia. *AAPG Bull.* 104 (8), 1679–1705. <https://doi.org/10.1306/04082017419>.
- Curtis, M.E., Cardott, B.J., Sondergeld, C.H., Rai, C.S., 2012a. Development of organic porosity in the Woodford Shale with increasing thermal maturity. *Int. J. Coal Geol.* 103, 26–31. <https://doi.org/10.1016/j.coal.2012.08.004>.
- Curtis, M.E., Sondergeld, C.H., Ambrose, R.J., Rai, C.S., 2012b. Microstructural investigation of gas shales in two and three dimensions using nanometer-scale resolution imaging. *AAPG Bull.* 96 (4), 665–677. <https://doi.org/10.1306/0815110188>.
- Daigle, H., Dugan, B., 2011. An improved technique for computing permeability from NMR measurements in mudstones. *J. Geophys. Res.-Sol. Earth* 116 (B8). <https://doi.org/10.1029/2011JB008353>.
- Desbois, G., Urai, J.L., Kukla, P.A., Konstanty, J., Baerle, C., 2011. High-resolution 3D fabric and porosity model in a tight gas sandstone reservoir: a new approach to investigate microstructures from mm-to nm-scale combining argon beam cross-sectioning and SEM imaging. *J. Pet. Sci. Eng.* 78 (2), 243–257. <https://doi.org/10.1016/j.petrol.2011.06.004>.
- Dewers, T.A., Heath, J., Ewy, R., Duranti, L., 2012. Three-dimensional pore networks and transport properties of a shale gas formation determined from focused ion beam serial imaging. *Int. J. Oil, Gas Coal Technol.* 5 (2–3), 229–248. <https://doi.org/10.1504/IJOGCT.2012.046322>.
- Dierolf, M., Menzel, A., Thibault, P., Schneider, P., Kewish, C.M., Wepf, R., Bunk, O., Pfeiffer, F., 2010. Ptychographic X-ray computed tomography at the nanoscale. *Nature* 467 (7314), 436–439. <https://doi.org/10.1038/nature09419>.
- Ding, Y.H., Jiang, X., Ren, H.M., Yin, R.J., Jiang, Y., Deng, X.H., Zhang, P., 2012. Research progress on applications of atomic force microscopy in micro- and nano-mechanics. *Mater. Rep.* 26 (13), 118–124 (in Chinese with English Abstract).
- Dong, H., Sun, J., Arif, M., Golsanami, N., Yan, W., Zhang, Y., 2020. A novel hybrid method for gas hydrate filling modes identification via digital rock. *Mar. Pet. Geol.* 115, 104255. <https://doi.org/10.1016/j.marpetgeo.2020.104255>.
- Dong, T., Harris, N.B., McMillan, J.M., Twemlow, C.E., Nassichuk, B.R., Bish, D.L., 2019. A model for porosity evolution in shale reservoirs: An example from the Upper Devonian Duvernay Formation, Western Canada Sedimentary Basin. *AAPG Bull.* 103 (5), 1017–1044. <https://doi.org/10.1306/10261817272>.
- Dorsch, J., 1995. Determination of effective porosity of mudrocks: a feasibility study. Oak Ridge National Lab.(ORNL), Oak Ridge, TN (United States).
- Douglas, J.R., Curry, K.J., Bennett, R., Head, A., 2013. Marine fine-grained sediment tortuosity derived from the analysis of three-dimensional reconstructions of organo-clay fabric at the nanometer scale. *AAPG Search Discov. Article* 90163. <https://www.searchanddiscovery.com/abstracts/html/2013/90163ace/abstracts/doug.htm>.
- Dubin, M., 1947. The equation of the characteristic curve of activated charcoal. *Dokl. Akad. Nauk SSSR* 327–329.
- Dubin, M., Timofeev, D., 1948. Adsorption and Physicochemical Properties of Vapor Substances. Laws and the Theory of Adsorption potential. *Russ. J. Phys. Chem.* 22, 133–136.
- Dunn, K.-J., Bergman, D.J., LaTorra, G.A., 2002. Nuclear magnetic resonance: Petrophysical and logging applications. Elsevier.
- Fernández-Delgado, M., Cernadas, E., Barro, S., Amorim, D., 2014. Do we need hundreds of classifiers to solve real world classification problems? *J. Mach. Learn. Res.* 15 (1), 3133–3181.
- Fishman, N.S., Hackley, P.C., Lowers, H.A., Hill, R.J., Egenhoff, S.O., Eberl, D.D., Blum, A.E., 2012. The nature of porosity in organic-rich mudstones of the Upper Jurassic Kimmeridge Clay Formation, North Sea, offshore United Kingdom. *Int. J. Coal Geol.* 103, 32–50. <https://doi.org/10.1016/j.coal.2012.07.012>.
- Fleury, M., 2007. NMR surface relaxivity determination using NMR apparent diffusion curves and BET measurements, International Symposium of the Society of Core Analysts. Calgary Canada 10–12.
- Fredrich, J.T., Menendez, B., Wong, T.F., 1995. Imaging the pore structure of geomaterials. *Science* 268 (5208), 276–279. <https://doi.org/10.1126/science.268.5208.276>.
- Friesen, W.I., Mikula, R.J., 1988. Mercury porosimetry of coals: pore volume distribution and compressibility. *Fuel* 67 (11), 1516–1520.
- Jiang, F.J., Huang, R.D., Hu, T., Lv, J.H., Huang, L.L., Jiang, Z.X., Hu, M.L., Zhang, C.X., Wu, G.Y., Wu, Y.P., 2022. Geological characteristics and classification evaluation of shale oil in Fengcheng Formation in Mahu sag, Junggar Basin. *Acta Pet. Sin.* 43 (7), 899–911 (in Chinese with English Abstract).
- Gao, Z.Y., Fan, Y.P., Hu, Q.H., Jiang, Z.X., Cheng, Y., 2020. The effects of pore structure on wettability and methane adsorption capability of Longmaxi Formation shale from the southern Sichuan Basin in China. *AAPG Bull.* 104 (6), 1375–1399. <https://doi.org/10.1306/011222019079>.
- García-Martínez, J., Cazorla-Amorós, D., Linares-Solano, A., 2000. Further evidences of the usefulness of CO<sub>2</sub> adsorption to characterize microporous solids. *Stud. Surf. Sci. Catal.* Elsevier 485–494.
- Garrido, J.J., Linares-Solano, A., Martín-Martínez, J.M., Molina-Sabio, M., Rodríguez-Reinos, F., Torregrosa, R., 1987. The effect of gasification by air (623 K) or CO<sub>2</sub> (1098 K) in the development of microporosity in activated carbons. *J. Chem. Soc. Faraday Trans.* 83, 1081–1088. <https://doi.org/10.1039/F19878301081>.
- Ghanbarian, B., Javadpour, F., 2017. Upscaling pore pressure-dependent gas permeability in shales. *J. Geophys. Res.-Sol. Earth* 122 (4), 2541–2552. <https://doi.org/10.1002/2016jb013846>.
- Giesche, H., 2006. Mercury porosimetry: a general (practical) overview. *Part. Part. Syst. Charact.* 23 (1), 9–19. <https://doi.org/10.1002/ppsc.200601009>.
- Giffin, S., Littke, R., Klaver, J., Urai, J., 2013. Application of BIB-SEM technology to characterize macropore morphology in coal. *Int. J. Coal Geol.* 114, 85–95. <https://doi.org/10.1016/j.coal.2013.02.009>.
- Glatter, O., 1977. A new method for the evaluation of small-angle scattering data. *J. Appl. Crystallogr.* 10 (5), 415–421. <https://doi.org/10.1107/S0021889877013879>.

- Glatter, O., 1979. The interpretation of real-space information from small-angle scattering experiments. *J. Appl. Crystallogr.* 12 (2), 166–175. <https://doi.org/10.1107/S0021889879012139>.
- Gordon, J.B., Sanei, H., Pedersen, P.K., 2022. Predicting hydrogen and oxygen indices (HI, OI) from conventional well logs using a Random Forest machine learning algorithm. *Int. J. Coal Geol.* 249 <https://doi.org/10.1016/j.coal.2021.103903>.
- Gu, Y.T., Li, X.X., Wan, Q., Yang, S.G., 2021. On the Different Characteristics of Organic Pores in Shale and their Influencing Factors: taking typical marine, continental, and transitional facies reservoirs in China as examples. *Acta Sedimentol. Sin.* 39 (4) (in Chinese with English Abstract).
- Guo, Y.C., Fang, X.X., Wang, H.F., Wang, N., 2022. Mineralogy and Pore Structure of Marine-Continental Transitional Shale: A Case Study of the Upper Carboniferous Keluke Formation in the Eastern Qaidam Basin, China. *Front. Earth Sci.* 9 <https://doi.org/10.3389/feart.2021.825173>.
- Han, H., Cao, Y., Chen, S.J., Lu, J.G., Huang, C.X., Zhu, H.H., Zhan, P., Gao, Y., 2016. Influence of particle size on gas-adsorption experiments of shales: an example from a Longmaxi Shale sample from the Sichuan Basin, China. *Fuel* 186, 750–757. <https://doi.org/10.1016/j.fuel.2016.09.018> (in Chinese).
- Handhal, A.M., Al-Abadi, A.M., Chafeet, H.E., Ismail, M.J., 2020. Prediction of total organic carbon at Rumaila oil field, Southern Iraq using conventional well logs and machine learning algorithms. *Mar. Pet. Geol.* 116, 104347 <https://doi.org/10.1016/j.marpetgeo.2020.104347>.
- He, H., Garcia, E.A., 2009. Learning from imbalanced data. *IEEE Trans. Knowl. Data Eng.* 21 (9), 1263–1284. <https://doi.org/10.1109/TKDE.2008.239>.
- He, J.G., 2014. Influence of fluid sensitivity damage on nano-pores of shale reservoir. *J. China Univ. Pet. (Ed. Nat. Sci.)* 38 (1), 98–104 (in Chinese with English Abstract).
- He, Q., 2019. Introduction. In: He, Q. (Ed.), *A Corpus-Based Approach to Clause Combining in English from the Systemic Functional Perspective*. Springer Singapore, Singapore, pp. 1–9. [https://doi.org/10.1007/978-981-13-7391-6\\_1](https://doi.org/10.1007/978-981-13-7391-6_1).
- Hinde, A.L., 2004. PRINSAS—a Windows-based computer program for the processing and interpretation of small-angle scattering data tailored to the analysis of sedimentary rocks. *J. Appl. Crystallogr.* 37 (6), 1020–1024. <https://doi.org/10.1107/S0021889804021260>.
- Horvath, G., Kawazoe, K., 1983. Method for the calculation of effective pore size distribution in molecular sieve carbon. *J. Chem. Eng. Jpn* 16 (6), 470–475. <https://doi.org/10.1252/jcej.16.470>.
- Hosseini, M., Arif, M., Keshavarz, A., Iglauer, S., 2021. Neutron scattering: a subsurface application review. *Earth Sci. Rev.* 221 <https://doi.org/10.1016/j.earscirev.2021.103755>.
- Hu, H.Y., Hao, F., Lin, J.F., Lu, Y.C., Ma, Y.Q., Li, Q., 2017. Organic matter-hosted pore system in the Wufeng-Longmaxi (O3)w-S(1)1 shale, Jiaoshiba area, Eastern Sichuan Basin, China. *Int. J. Coal Geol.* 173, 40–50. <https://doi.org/10.1016/j.coal.2017.02.004>.
- Hu, Q.H., Quintero, R.P., El-Sobky, H.F., Kang, J.H., Zhang, T., 2020. Coupled nanopetrophysical and organic-geochemical study of the Wolfberry Play in Howard County, Texas USA. *Mar. Pet. Geol.* 122 <https://doi.org/10.1016/j.marpetgeo.2020.104663>.
- Hu, T., Pang, X.-Q., Jiang, F.-J., Wang, Q.-F., Wu, G.-Y., Liu, X.-H., Jiang, S., Li, C.-R., Xu, T.-W., Chen, Y.-Y., 2021. Key factors controlling shale oil enrichment in saline lacustrine rift basin: implications from two shale oil wells in Dongpu Depression, Bohai Bay Basin. *Pet. Sci.* 18 (3), 687–711. <https://doi.org/10.1007/s12182-021-00564-z>.
- Hu, T., Pang, X., Jiang, F., Zhang, C., Wu, G., Hu, M., Jiang, L., Wang, Q., Xu, T., Hu, Y., Jiang, S., Wang, W., Li, M., 2022. Dynamic continuous hydrocarbon accumulation (DCHA): existing theories and a new unified accumulation model. *Earth Sci. Rev.* 232, 104109 <https://doi.org/10.1016/j.earscirev.2022.104109>.
- Hu, T., Pang, X.Q., Jiang, F.J., Wang, Q.F., Liu, X.H., Wang, Z., Jiang, S., Wu, G.Y., Li, C. J., Xu, T.W., Li, M.W., Yu, J.W., Zhang, C.X., 2021b. Movable oil content evaluation of lacustrine organic-rich shales: Methods and a novel quantitative evaluation model. *Earth Sci. Rev.* 214 <https://doi.org/10.1016/j.earscirev.2021.103545>.
- Hurlimann, M., Helmer, K.G., Latour, L., Sotak, C.H., 1994. Restricted diffusion in sedimentary rocks. Determination of surface-area-to-volume ratio and surface relaxivity. *J. Magn. Reson. Ser. A* 111 (2), 169–178. <https://doi.org/10.1006/jmra.1994.1243>.
- Ilavsky, J., Jemian, P.R., 2009. Irena: tool suite for modeling and analysis of small-angle scattering. *J. Appl. Crystallogr.* 42 (2), 347–353. <https://doi.org/10.1107/S0021889809002222>.
- Iqbal, M.A., Rezaee, R., Smith, G., Ekundayo, J.M., 2021. Shale lithofacies controls on porosity and pore structure: an example from Ordovician Goldwyer Formation, Canning Basin, Western Australia. *J. Nat. Gas Sci. Eng.* 89 <https://doi.org/10.1016/j.jngse.2021.103888>.
- Jaroniec, M., Solovyov, L.A., 2006. Improvement of the Kruk-Jaroniec-Sayari method for pore size analysis of ordered silicas with cylindrical mesopores. *Langmuir* 22 (16), 6757–6760. <https://doi.org/10.1021/la0609571>.
- Ji, W.M., Song, Y., Rui, Z.H., Meng, M.M., Huang, H.X., 2017. Pore characterization of isolated organic matter from high matured gas shale reservoir. *Int. J. Coal Geol.* 174, 31–40. <https://doi.org/10.1016/j.coal.2017.03.005>.
- Jia, C., 2018. Research on core pore based on NMR measurement. Beijing University of Chemical Technology (in Chinese).
- Jiang, F.J., Chen, D., Wang, Z.F., Xu, Z.Y., Chen, J., Liu, L., Huyan, Y.Y., Liu, Y., 2016a. Pore characteristic analysis of a lacustrine shale: a case study in the Ordos Basin, NW China. *Mar. Pet. Geol.* 73, 554–571. <https://doi.org/10.1016/j.marpetgeo.2016.03.026>.
- Jiang, Z.X., Tang, X.L., Li, Z., Huang, H.X., Yang, P.P., Yang, X., Li, W.B., Hao, J., 2016b. The whole aperture pore structure characteristics and its effect on gas content of the Longmaxi Formation shale in the southeastern Sichuan Basin. *Earth Sci. Front.* 23 (2), 126–134 (in Chinese with English Abstract).
- Jiao, K., Yao, S., Liu, C., Gao, Y., Wu, H., Li, M.C., Tang, Z., 2014. The characterization and quantitative analysis of nanopores in unconventional gas reservoirs utilizing FESEM-FIB and image processing: An example from the lower Silurian Longmaxi Shale, upper Yangtze region, China. *Int. J. Coal Geol.* 128, 1–11. <https://doi.org/10.1016/j.coal.2014.03.004>.
- Jiao, K., Yao, S.P., Liu, C., Gao, Y.Q., Wu, H., Li, M.C., Tang, Z.Y., 2014. The characterization and quantitative analysis of nanopores in unconventional gas reservoirs utilizing FESEM-FIB and image processing: An example from the lower Silurian Longmaxi Shale, upper Yangtze region, China. *Int. J. Coal Geol.* 128, 1–11. <https://doi.org/10.1016/j.coal.2014.03.004>.
- Jiao, K., Yao, S.P., Wu, H., Li, M.C., Tang, Z.Y., 2014c. Advances in characterization of pore system of gas shales. *Geol. J. China U.* 20 (1), 151 (in Chinese with English Abstract).
- Ju, Y., Sun, Y., Tan, J., Bu, H., Han, K., Li, X., Fang, L., 2018. The composition, pore structure characterization and deformation mechanism of coal-bearing shales from tectonically altered coalfields in eastern China. *Fuel* 234, 626–642. <https://doi.org/10.1016/j.fuel.2018.06.116>.
- Kennedy, M., Löhr, S., Fraser, S., Baruch, E., 2014. Direct evidence for organic carbon preservation as clay-organic nanocomposites in a Devonian black shale; from deposition to diagenesis. *Earth Planet. Sci. Lett.* 388, 59–70. <https://doi.org/10.1016/j.epsl.2013.11.044>.
- Kennedy, M.J., Pevear, D.R., Hill, R.J., 2002. Mineral surface control of organic carbon in black shale. *Science* 295 (5555), 657–660. <https://doi.org/10.1126/science.1066611>.
- Klaver, J., Desbois, G., Urai, J.L., Littke, R., 2012. BIB-SEM study of the pore space morphology in early mature Posidonia Shale from the Hils area, Germany. *Int. J. Coal Geol.* 103, 12–25. <https://doi.org/10.1016/j.coal.2012.06.012>.
- Kleinberg, R.L., Kenyon, W.E., Mitra, P.P., 1994a. Mechanism of NMR relaxation of fluids in rock. *J. Magn. Reson. Ser. A* 108 (2), 206–214. <https://doi.org/10.1006/jmra.1994.1112>.
- Kleinberg, R.L., Horsfield, M.A., 1990. Transverse relaxation processes in porous sedimentary rock. *J. Magn. Reson.* 88 (1), 9–19. [https://doi.org/10.1016/0022-2364\(90\)90104-H](https://doi.org/10.1016/0022-2364(90)90104-H).
- Kleinberg, R.L., Kenyon, W.E., Mitra, P.P., 1994b. Mechanism of NMR Relaxation of Fluids in Rock. *J. Magn. Reson.* 108, 206–214. <https://doi.org/10.1006/jmra.1994.1112>.
- Knapp, L.J., Ardakani, O.H., Uchida, S., Nanjo, T., Otomo, C., Hattori, T., 2020. The influence of rigid matrix minerals on organic porosity and pore size in shale reservoirs: Upper Devonian Duvernay Formation, Alberta, Canada. *Int. J. Coal Geol.* 227 <https://doi.org/10.1016/j.coal.2020.103525>.
- Ko, L.T., Loucks, R.G., Ruppel, S.C., Zhang, T.W., Peng, S., 2017. Origin and characterization of Eagle Ford pore networks in the South Texas upper cretaceous shelf. *AAPG Bull.* 101 (3), 387–418. <https://doi.org/10.1306/08051616035>.
- Kruk, M., Jaroniec, M., Sayari, A., 1997. Application of large pore MCM-41 molecular sieves to improve pore size analysis using nitrogen adsorption measurements. *Langmuir* 13 (23), 6267–6273. <https://doi.org/10.1021/la970776m>.
- Kuila, U., Prasad, M., 2013. Application of nitrogen gas-adsorption technique for characterization of pore structure of mudrocks. In: *The Leading Edge*, 32. Society of Exploration Geophysicists, pp. 1478–1485. <https://doi.org/10.1190/tle32121478.1>.
- Kuila, U., Prasad, M., 2013b. Specific surface area and pore-size distribution in clays and shales. *Geophys. Prospect.* 61 (2), 341–362. <https://doi.org/10.1111/1365-2478.12028>.
- Lahann, R., Mastalerz, M., Rupp, J., Drobnik, A., 2013. Influence of CO<sub>2</sub> on New Albany Shale composition and pore structure. *Int. J. Coal Geol.* 108 <https://doi.org/10.1016/j.coal.2011.05.004>.
- Lai, J., Wang, G.W., Wang, Z.Y., Chen, J., Pang, X.J., Wang, S.C., Zhou, Z.L., He, Z.B., Qin, Z.Q., Fan, X.Q., 2018. A review on pore structure characterization in tight sandstones. *Earth Sci. Rev.* 177, 436–457. <https://doi.org/10.1016/j.earscirev.2017.12.003>.
- Lame, O., Bellet, D., Di Michiel, M., Bouvard, D., 2004. Bulk observation of metal powder sintering by X-ray synchrotron microtomography. *Acta Mater.* 52 (4), 977–984. <https://doi.org/10.1016/j.actamat.2003.10.032>.
- Landers, J., Gor, G.Y., Neimark, A.V., 2013. Density functional theory methods for characterization of porous materials. *Colloid. Surf. A* 437, 3–32. <https://doi.org/10.1016/j.colsurfa.2013.01.007>.
- Lastoskie, C., Gubbins, K.E., Quirke, N., 1993. Pore size distribution analysis of microporous carbons: a density functional theory approach. *J. Phys. Chem.* 97 (18), 4786–4796. <https://doi.org/10.1021/j100120a035>.
- Lawal, L.O., Adebayo, A.R., Mahmoud, M., Dia, B., Sultan, A.S., 2020. A novel NMR surface relaxivity measurements on rock cuttings for conventional and unconventional reservoirs. *Int. J. Coal Geol.* 231 <https://doi.org/10.1016/j.coal.2020.103605>.
- Lee, K.S., Kim, T.H., 2019. Chapter 2-Petrophysical characteristics of shale reservoirs. In: Lee, K.S., Kim, T.H. (Eds.), *Transport in Shale Reservoirs*. Gulf Professional Publishing, pp. 7–34. <https://doi.org/10.1016/B978-0-12-817860-7.00002-4>.
- Li, H., Zhu, J., Guo, H., 2008. Methods for calculating pore radius distribution in rock from NMR T<sub>2</sub> spectra. *Chin. J. Magn. Reson.* 25 (2), 273–280.
- Li, J., Zhou, S.X., Li, Y.J., Ma, Y., Yang, Y.A., Li, C.C., 2016. Effect of organic matter on pore structure of mature lacustrine organic-rich shale: A case study of the Triassic Yanchang shale, Ordos Basin, China. *Fuel* 185, 421–431. <https://doi.org/10.1016/j.fuel.2016.07.100>.
- Li, J.J., Yin, J.X., Zhang, Y.N., Lu, S.F., Wang, W.M., Li, J.B., Chen, F.W., Meng, Y.L., 2015. A comparison of experimental methods for describing shale pore features-a



- case study in the Bohai Bay Basin of eastern China. *Int. J. Coal Geol.* 152, 39–49. <https://doi.org/10.1016/j.coal.2015.10.009>.
- Li, J.Z., 1995. Investigation of porosity in ceramic SiC using small-angle neutron scattering. *Annu. Rep. China Inst. Atomic Energy* 1, 197–199 (in Chinese).
- Li, W.H., Lu, S.F., Xue, H.T., Zhang, P.F., Hu, Y., 2016b. Microscopic pore structure in shale reservoir in the argillaceous dolomite from the Jiangnan Basin. *Fuel* 181, 1041–1049. <https://doi.org/10.1016/j.fuel.2016.04.140>.
- Li, W.W., Cao, J., Shi, C.H., Xu, T.W., Zhang, H.G., Zhang, Y.X., 2020. Shale oil in saline lacustrine systems: a perspective of complex lithologies of fine-grained rocks. *Mar. Pet. Geol.* 116 <https://doi.org/10.1016/j.marpetgeo.2020.104351>.
- Li, Z.Q., Shen, X., Qi, Z.Y., Hu, R.L., 2017. Comparisons between mercury intrusion and gas adsorption for pore structure characteristics of shale. *J. Eng. Geol.* 25 (6), 1405–1413 (in Chinese with English Abstract).
- Liu, B., Mastalerz, M., Schieber, J., 2022. SEM petrography of dispersed organic matter in black shales: a review. *Earth Sci. Rev.* 224 <https://doi.org/10.1016/j.earscirev.2021.103874>.
- Liu, K., Ostadhassan, M., Kong, L., 2019a. Fractal and Multifractal Characteristics of Pore Throats in the Bakken Shale. *Transp. Porous Media* 126 (3), 579–598. <https://doi.org/10.1007/s11242-018-1130-2>.
- Liu, K.Q., Ostadhassan, M., Sun, L.W., Zou, J., Yuan, Y.J., Gentzis, T., Zhang, Y.X., Carvajal-Ortiz, H., Rezaee, R., 2019b. A comprehensive pore structure study of the Bakken Shale with SANS, N-2 adsorption and mercury intrusion. *Fuel* 245, 274–285. <https://doi.org/10.1016/j.fuel.2019.01.174>.
- Liu, K.Q., Ostadhassan, M., Zhou, J., Gentzis, T., Rezaee, R., 2017a. Nanoscale pore structure characterization of the Bakken shale in the USA. *Fuel* 209, 567–578. <https://doi.org/10.1016/j.fuel.2017.08.034>.
- Liu, R., Liu, Z.J., Sun, P.C., Yang, X.H., Zhang, C., 2017b. Shale gas accumulation potential of the Upper cretaceous Qingshankou Formation in the southeast Songliao Basin, NE China. *Mar. Pet. Geol.* 86, 547–562. <https://doi.org/10.1016/j.marpetgeo.2017.05.014>.
- Liu, X., Song, D., He, X., Wang, Z., Zeng, M., Deng, K., 2019c. Nanopore structure of deep-burial coals explored by AFM. *Fuel* 246, 9–17. <https://doi.org/10.1016/j.fuel.2019.02.090>.
- Loucks, R.G., Reed, R.M., Ruppel, S.C., Hammes, U., 2012. Spectrum of pore types and networks in mudrocks and a descriptive classification for matrix-related mudrock pores. *AAPG Bull.* 96 (6), 1071–1098. <https://doi.org/10.1306/0817111061>.
- Loucks, R.G., Reed, R.M., Ruppel, S.C., Jarvie, D.M., 2009. Morphology, genesis, and distribution of nanometer-scale pores in siliceous mudstones of the Mississippian Barnett Shale. *J. Sediment. Res.* 79 (12), 848–861. <https://doi.org/10.2110/jsr.2009.092>.
- Lu, Y., Ao, X., Tang, J., Jia, Y., Zhang, X., Chen, Y., 2016. Swelling of shale in supercritical carbon dioxide. *J. Nat. Gas Sci. Eng.* 30 <https://doi.org/10.1016/j.jngse.2016.02.011>.
- Lu, Y., Liu, K., 2021. Pore Structure Characterization of Eocene Low-Permeability Sandstones via Fractal Analysis and Machine Learning: An Example from the Dongying Depression, Bohai Bay Basin, China. *ACS Omega* 6 (17), 11693–11710. <https://doi.org/10.1021/acsomega.1c01015>.
- Lucena, S.M., Paiva, C.A.S., Silvino, P.F., Azevedo, D.C., Cavalcante Jr., C.L., 2010. The effect of heterogeneity in the randomly etched graphite model for carbon pore size characterization. *Carbon* 48 (9), 2554–2565. <https://doi.org/10.1016/j.carbon.2010.03.034>.
- Luo, X.R., Wang, S.Z., Wang, Z.G., Jing, Z.F., Lv, M.M., Zhai, Z.D., Han, T., 2015. Adsorption of methane, carbon dioxide and their binary mixtures on Jurassic shale from the Qaidam Basin in China. *Int. J. Coal Geol.* 150, 210–223. <https://doi.org/10.1016/j.coal.2015.09.004>.
- Ma, K., Pang, X., Pang, H., Lv, C., Gao, T., Chen, J., Huo, X., Cong, Q., Jiang, M., 2022. A novel method for favorable zone prediction of conventional hydrocarbon accumulations based on RUSBoosted tree machine learning algorithm. *Appl. Energy* 326. <https://doi.org/10.1016/j.apenergy.2022.119983>.
- Ma, Y., Pan, Z., Zhong, N., Connell, L.D., Down, D.I., Lin, W., Zhang, Y., 2016. Experimental study of anisotropic gas permeability and its relationship with fracture structure of Longmaxi Shales, Sichuan Basin, China. *Fuel* 180, 106–115. <https://doi.org/10.1016/j.fuel.2016.04.029>.
- Macquaker, J., Keller, M., Davies, S., 2010. Algal Blooms and "Marine Snow": Mechanisms that Enhance Preservation of Organic Carbon in Ancient Fine-Grained Sediments. *J. Sediment. Res.* 80, 934–942. <https://doi.org/10.2110/jsr.2010.085>.
- Mao, W., Guo, S., 2018. Comparison of Factors Influencing Pore size Distributions in Marine, Terrestrial, and Transitional Shales of similar Maturity in China. *Energy Fuel* 32 (8), 8145–8153. <https://doi.org/10.1021/acs.energyfuels.8b01373>.
- Mastalerz, M., Schimmelmann, A., Drobnik, A., Chen, Y., 2013. Porosity of Devonian and Mississippian New Albany Shale across a maturation gradient: Insights from organic petrology, gas adsorption, and mercury intrusion. *AAPG Bull.* 97 (10), 1621–1643. <https://doi.org/10.1306/04011312194>.
- Mayer, J., Giannuzzi, L.A., Kamino, T., Michael, J., 2007. TEM sample preparation and FIB-induced damage. *MRS Bull.* 32 (5), 400–407. <https://doi.org/10.1557/mrs2007.63>.
- Melnichenko, Y.B., He, L., Sakurov, R., Kholodenko, A.L., Blach, T., Mastalerz, M., Radlinski, A.P., Cheng, G., Mildner, D.F., 2012. Accessibility of pores in coal to methane and carbon dioxide. *Fuel* 91 (1), 200–208. <https://doi.org/10.1016/j.fuel.2011.06.026>.
- Menger, S., Prammer, M., 1998. Can NMR porosity replace conventional porosity in formation evaluation?. In: *SPWLA 39th Annual Logging Symposium*. OnePetro.
- Meyer, K., Klobes, P., 1999. Comparison between different presentations of pore size distribution in porous materials. *Fresenius J. Anal. Chem.* 363 (2), 174–178. <https://doi.org/10.1007/s002160051166>.
- Min, C., Dai, B.R., Zhang, X.H., Du, J.P., 2020. A Review of the Application Progress of Machine Learning in Oil and Gas Industry. *J. Southwest Pet. Univ. (Sci. Technol. Ed.)* 42 (06), 1–15 (in Chinese with English Abstract).
- Milliken, K., Ko, L.T., Pommer, M., Marsaglia, K., 2014. Sem Petrography of Eastern Mediterranean Sapropels: Analogue Data for Assessing Organic Matter in Oil and Gas Shales. *J. Sediment. Res.* 84, 961–974. <https://doi.org/10.2110/jsr.2014.75>.
- Milliken, K.L., Rudnicki, M., Awwiller, D.N., Zhang, T., 2013. Organic matter-hosted pore system, Marcellus Formation (Devonian), Pennsylvania. *AAPG Bull.* 97 (2), 177–200. <https://doi.org/10.1306/07231212048>.
- Milliken, K.L., Rudnicki, M., Awwiller, D.N., Zhang, T., 2013. Organic matter-hosted pore system, Marcellus formation (Devonian), Pennsylvania. *AAPG Bull.* 97 (2), 177–200. <https://doi.org/10.1306/07231212048>.
- Monson, P.A., 2008. Contact angles, pore condensation, and hysteresis: insights from a simple molecular model. *Langmuir* 24 (21), 12295–12302. <https://doi.org/10.1021/la801972e>.
- Monson, P.A., 2012. Understanding adsorption/desorption hysteresis for fluids in mesoporous materials using simple molecular models and classical density functional theory. *Microporous Mesoporous Mater.* 160, 47–66. <https://doi.org/10.1016/j.micromeso.2012.04.043>.
- Neimark, A.V., 1995. The method of indeterminate Lagrange multipliers in nonlocal density functional theory. *Langmuir* 11 (10), 4183–4184. <https://doi.org/10.1021/la00010a090>.
- Neimark, A.V., Ravikovitch, P.I., Vishnyakov, A., 2003. Bridging scales from molecular simulations to classical thermodynamics: density functional theory of capillary condensation in nanopores. *J. Phys. Condens. Mat.* 15 (3), 347. <https://doi.org/10.1088/0953-8984/15/3/303>.
- Neimark, A.V., Sing, K.S.W., Thommes, M., 2023. Surface area and porosity. In: *Handbook of Heterogeneous Catalysis*, pp. 721–738. <https://doi.org/10.1002/9783527610044.hetcat0037>.
- Nikolaev, M.Y., Kazak, A.V., 2019. Liquid saturation evaluation in organic-rich unconventional reservoirs: a comprehensive review. *Earth Sci. Rev.* 194, 327–349. <https://doi.org/10.1016/j.earscirev.2019.05.012>.
- Olaremu, A.G., 2015. Physico-Chemical Characterization of Akoko Mined Kaolin Clay. *J. Miner. Mater. Charact. Eng.* 03 (05), 353–361. <https://doi.org/10.4236/jmmce.2015.35038>.
- Olivier, J., Konklun, W., Szombathely, M., 1994. Determination of pore size distribution from density functional theory: a comparison of nitrogen and argon results. *Stud. Surf. Sci. Catal. Elsevier* 81–89.
- Peltonen, C., Marcussen, Ø., Bjørlykke, K., Jahren, J., 2009. Clay mineral diagenesis and quartz cementation in mudstones: the effects of smectite to illite reaction on rock properties. *Mar. Pet. Geol.* 26 (6), 887–898. <https://doi.org/10.1016/j.marpetgeo.2008.01.021>.
- Pommer, M., Milliken, K., 2015. Pore types and pore-size distributions across thermal maturity, Eagle Ford Formation, southern Texas. *AAPG Bull.* 99, 1713–1744. <https://doi.org/10.1306/03051514151>.
- Prisk, T.R., Das, N.C., Diallo, S.O., Ehlers, G., Podlesnyak, A.A., Wada, N., Inagaki, S., Sokol, P.E., 2013. Phases of superfluid helium in smooth cylindrical pores. *Phys. Rev. B* 88 (1). <https://doi.org/10.1103/PhysRevB.88.014521>.
- Purcell, W., 1949. Capillary pressures-their measurement using mercury and the calculation of permeability therefrom. *J. Pet. Technol.* 1 (02), 39–48. <https://doi.org/10.2118/949039-G>.
- Qin, L.Q., Wu, B.L., Wei, M.J., Sun, Z.Y., 2001. Determination of micro-pore size distribution in alumina powder by small-angle X-ray scattering. *Chin. J. Sci. Instrum.* 1 (in Chinese with English Abstract).
- Qiu, Z., Song, D.J., Zhang, L.F., Zhang, Q., Zhao, Q., Wang, Y.M., Liu, H.L., Liu, D.X., Li, S.X., Li, X.T., 2021. The geochemical and pore characteristics of a typical marine-continental transitional gas shale: a case study of the Permian Shanxi Formation on the eastern margin of the Ordos Basin. *Energy Rep.* 7, 3726–3736. <https://doi.org/10.1016/j.egyr.2021.06.056>.
- Radlinski, A., Mastalerz, M., Hinde, A., Hainbuchner, M., Rauch, H., Baron, M., Lin, J., Fan, L., Thiagarajan, P., 2004. Application of SAXS and SANS in evaluation of porosity, pore size distribution and surface area of coal. *Int. J. Coal Geol.* 59 (3–4), 245–271. <https://doi.org/10.1016/j.coal.2004.03.002>.
- Radlinski, A.P., 2006. Small-angle neutron scattering and the microstructure of rocks. *Rev. Mineral. Geochem.* 63 (1), 363–397. <https://doi.org/10.2138/rmg.2006.63.14>.
- Rathousky, J., Thommes, M., 2007. Adsorption properties and advanced textural characterization of novel micro/mesoporous zeolites. In: *From Zeolites to Porous MOF Materials: The 40th Anniversary of International Zeolite Conference, Proceedings of the 15th International Zeolite Conference*, pp. 1042–1047.
- Ravikovitch, P.I., Neimark, A.V., 2006a. Density functional theory model of adsorption on amorphous and microporous silica materials. *Langmuir* 22 (26), 11171–11179. <https://doi.org/10.1021/la0616146>.
- Ravikovitch, P.I., Neimark, A.V., 2006b. Density functional theory model of adsorption on amorphous and microporous silica materials. *Langmuir* 22 (26), 11171–11179.
- Rouquerol, J., Avnir, D., Fairbridge, C., Everett, D., Haynes, J., Pernicone, N., Ramsay, J., Sing, K., Unger, K., 1994. Recommendations for the characterization of porous solids (Technical Report). *Pure Appl. Chem.* 66 (8), 1739–1758. <https://doi.org/10.1351/pac199466081739>.
- Rouquerol, J., Rouquerol, F., 2014. 3-Methodology of Gas Adsorption. In: *Rouquerol, F., Rouquerol, J., Sing, K.S.W., Llewellyn, P., Maurin, G. (Eds.), Adsorption by Powders and Porous Solids, Second edition*. Academic Press, Oxford, pp. 57–104. <https://doi.org/10.1016/B978-0-08-097035-6.00003-6>.
- Rui, J., Zhang, H., Ren, Q., Yan, L., Guo, Q., Zhang, D., 2020. TOC content prediction based on a combined Gaussian process regression model. *Mar. Pet. Geol.* 118 <https://doi.org/10.1016/j.marpetgeo.2020.104429>.

- Saidian, M., Prasad, M., 2015. Effect of mineralogy on nuclear magnetic resonance surface relaxivity: a case study of Middle Bakken and three Forks formations. *Fuel* 161, 197–206. <https://doi.org/10.1016/j.fuel.2015.08.014>.
- Sanei, H., Ardakani, O.H., 2016. Alteration of organic matter by ion milling. *Int. J. Coal Geol.* 163, 123–131. <https://doi.org/10.1016/j.coal.2016.06.021>.
- Scherer, G.W., 2004. Stress from crystallization of salt. *Cem. Concr. Res.* 34 (9), 1613–1624. <https://doi.org/10.1016/j.cemconres.2003.12.034>.
- Seaton, N., Walton, J., 1989. A new analysis method for the determination of the pore size distribution of porous carbons from nitrogen adsorption measurements. *Carbon* 27 (6), 853–861. [https://doi.org/10.1016/0008-6223\(89\)90035-3](https://doi.org/10.1016/0008-6223(89)90035-3).
- Seiffert, C., Khoshgoftaar, T.M., Hulse, J.V., Napolitano, A., 2010. RUSBoost: a Hybrid Approach to Alleviating Class Imbalance. *IEEE Trans. Syst. Man Cybern. Syst. Hum.* 40 (1), 185–197. <https://doi.org/10.1109/TSMCA.2009.2029559>.
- Shao, X.H., Pang, X.Q., Li, H., Hu, T., Xu, T.W., Xu, Y., Li, B.Y., 2018. Pore network characteristics of lacustrine shales in the Dongpu Depression, Bohai Bay Basin, China, with implications for oil retention. *Mar. Pet. Geol.* 96, 457–473. <https://doi.org/10.1016/j.marpetgeo.2018.06.015>.
- Shen, R., Zhang, X., Ke, Y., Xiong, W., Guo, H., Liu, G., Zhou, H., Yang, H., 2021. An integrated pore size distribution measurement method of small angle neutron scattering and mercury intrusion capillary pressure. *Sci. Rep.* 11 (1), 17458. <https://doi.org/10.1038/s41598-021-97027-7>.
- Sing, K., 1982. Reporting Physisorption Data for Gas/Solid Systems with special Reference to the Determination of Surface Area and Porosity. *Pure Appl. Chem.* 54, 2201–2218. <https://doi.org/10.1351/pac198254112201>.
- Sing, K.S., Williams, R.T., 2004. The use of molecular probes for the characterization of nanoporous adsorbents. *Part. Part. Syst. Charact.* 21 (2), 71–79. <https://doi.org/10.1002/ppsc.200400923>.
- Sing, K.S.W., Everett, D.H., Haul, R.A.W., Moscou, L., Pierotti, R.A., Rouquerol, J., Siemieniowska, T., 1985. Reporting Physisorption Data for Gas Solid Systems with special Reference to the Determination of Surface-Area and Porosity (Recommendations 1984). *Pure Appl. Chem.* 57 (4), 603–619. <https://doi.org/10.1351/pac198557040603>.
- Sircar, A., Yadav, K., Rayavarapu, K., Bist, N., Oza, H., 2021. Application of machine learning and artificial intelligence in oil and gas industry. *Pet. Res.* 6 (4), 379–391. <https://doi.org/10.1016/j.ptlrs.2021.05.009>.
- Skalinski, M., Kenter, J., 2013. Pore Typing Workflow for Complex Carbonate Systems. AAPG Annual Convention and Exhibition, Pittsburgh (USA).
- Speiser, J.L., Durkalski, V.L., Lee, W.M., 2015. Random forest classification of etiologies for an orphan disease. *Stat. Med.* 34 (5), 887–899. <https://doi.org/10.1002/sim.6351>.
- Spitzer, Z., 1981. Mercury porosimetry and its application to the analysis of coal pore structure. *Powder Technol.* 29 (1), 177–186. [https://doi.org/10.1016/0032-5910\(81\)85015-2](https://doi.org/10.1016/0032-5910(81)85015-2).
- Stumpf, A., Kerle, N., 2011. Object-oriented mapping of landslides using Random Forests. *Remote Sens. Environ.* 115 (10), 2564–2577. <https://doi.org/10.1016/j.rse.2011.05.013>.
- Sun, L.N., Tuo, J.C., Zhang, M.F., Wu, C.J., Chai, S.Q., 2019. Pore structures and fractal characteristics of nano-pores in shale of Lucaogou formation from Junggar Basin during water pressure-controlled artificial pyrolysis. *J. Anal. Appl. Pyrolysis* 140, 404–412. <https://doi.org/10.1016/j.jaap.2019.04.020>.
- Sun, M., Yu, B., Hu, Q., Yang, R., Zhang, Y., Li, B., 2017a. Pore connectivity and tracer migration of typical shales in South China. *Fuel* 203, 32–46. <https://doi.org/10.1016/j.fuel.2017.04.086>.
- Sun, M., Yu, B., Hu, Q., Zhang, Y., Li, B., Yang, R., Melnichenko, Y.B., Cheng, G., 2017b. Pore characteristics of Longmaxi shale gas reservoir in the Northwest of Guizhou, China: Investigations using small-angle neutron scattering (SANS), helium pycnometry, and gas sorption isotherm. *Int. J. Coal Geol.* 171, 61–68. <https://doi.org/10.1016/j.coal.2016.12.004>.
- Svergun, D.I., 1991. Mathematical methods in small-angle scattering data analysis. *J. Appl. Crystallogr.* 24 (5), 485–492. <https://doi.org/10.1107/S0021889891001280>.
- Swpu, P., 2018. Modeling the effect of water vaporization and salt precipitation on reservoir properties due to carbon dioxide sequestration in a depleted gas reservoir-NC-ND license. *Petroleum*. 4, 385–397. <https://doi.org/10.1016/j.petlm.2017.12.003>.
- Tan, M., Liu, Q., Zhang, S., 2013. A dynamic adaptive radial basis function approach for total organic carbon content prediction in organic shale. *Geophysics* 78 (6), D445–D459. <https://doi.org/10.1190/geo2013-0154.1>.
- Thommes, M., 2004. Physical adsorption characterization of ordered and amorphous mesoporous materials, Nanoporous materials: science and engineering. *World Sci.* 317–364. [https://doi.org/10.1142/9781860946561\\_0011](https://doi.org/10.1142/9781860946561_0011).
- Thommes, M., 2010. Physical adsorption characterization of nanoporous materials. *Chem. Ing. Tech.* 82 (7), 1059–1073. <https://doi.org/10.1002/cite.201000064>.
- Thommes, M., Cychosz, K.A., Neimark, A.V., 2012. Advanced physical adsorption characterization of nanoporous carbons, Novel carbon adsorbents. Elsevier Ltd.
- Thommes, M., Kaneko, K., Neimark, A.V., Olivier, J.P., Rodriguez-Reinoso, F., Rouquerol, J., Sing, K.S.W., 2015. Physisorption of gases, with special reference to the evaluation of surface area and pore size distribution (IUPAC Technical Report). *Pure Appl. Chem.* 87 (9–10), 1051–1069. <https://doi.org/10.1515/pac-2014-1117>.
- Thommes, M., Mitchell, S., Perez-Ramirez, J., 2012b. Surface and pore structure assessment of hierarchical MFI zeolites by advanced water and argon sorption studies. *J. Phys. Chem. C* 116 (35), 18816–18823. <https://doi.org/10.1021/jp3051214>.
- Tian, H., Pan, L., Xiao, X., Wilkins, R.W.T., Meng, Z., Huang, B., 2013. A preliminary study on the pore characterization of lower Silurian black shales in the Chuandong Thrust Fold Belt, southwestern China using low pressure N<sub>2</sub> adsorption and FE-SEM methods. *Mar. Pet. Geol.* 48, 8–19. <https://doi.org/10.1016/j.marpetgeo.2013.07.008>.
- Tian, H., Zhang, S.C., Liu, S.B., Zhang, H., 2012. Determination of organic-rich shale pore features by mercury injection and gas adsorption methods. *Acta Pet. Sin.* 33 (3), 419–427 (in Chinese with English Abstract).
- Toda, Y., Toyoda, S., 1972. Application of mercury porosimetry to coal. *Fuel* 51 (3), 199–201. [https://doi.org/10.1016/0016-2361\(72\)90080-4](https://doi.org/10.1016/0016-2361(72)90080-4).
- Tomutsa, L., Radmilovic, V., 2003. Focused ion beam assisted three-dimensional rock imaging at submicron scale. Lawrence Berkeley National Lab.(LBNL), Berkeley, CA (United States).
- Tomutsa, L., Silin, D., Radmilovic, V., 2007. Analysis of chalk petrophysical properties by means of submicron-scale pore imaging and modeling. *SPE Reserv. Eval. Eng.* 10 (03), 285–293. <https://doi.org/10.2118/99558-PA>.
- Valiullin, R., Naumov, S., Galvosas, P., Karger, J., Woo, H.J., Porcheron, F., Monson, P. A., 2006. Exploration of molecular dynamics during transient sorption of fluids in mesoporous materials. *Nature* 443 (7114), 965–968. <https://doi.org/10.1038/nature05183>.
- Von Rueden, L., Mayer, S., Beckh, K., Georgiev, B., Giesselbach, S., Heese, R., Kirsch, B., Walczak, M., Pfrommer, J., Pick, A., Ramamurthy, R., Garcke, J., Bauckhage, C., Schuecker, J., 2021. Informed Machine Learning - a Taxonomy and survey of Integrating prior Knowledge into Learning Systems. *IEEE Trans. Knowl. Data Eng.* 1–1. <https://doi.org/10.1109/tkde.2021.3079836>.
- Wang, B.Y., Liu, B., Yang, J.G., Bai, L.H., Li, S.C., 2022. Compatibility characteristics of fracturing fluid and shale oil reservoir: A case study of the first member of Qingshankou Formation, northern Songliao Basin, Northeast China. *J. Pet. Sci. Eng.* 211. <https://doi.org/10.1016/j.petrol.2022.110161>.
- Wang, E., Feng, Y., Guo, T., Li, M., 2022b. Oil content and resource quality evaluation methods for lacustrine shale: a review and a novel three-dimensional quality evaluation model. *Earth Sci. Rev.* 232, 104134. <https://doi.org/10.1016/j.earscirev.2022.104134>.
- Wang, E., Guo, T., Li, M., Li, C., Dong, X., Zhang, N., Feng, Y., 2022c. Exploration potential of different lithofacies of deep marine shale gas systems: Insight into organic matter accumulation and pore formation mechanisms. *J. Nat. Gas Sci. Eng.* 102, 104563. <https://doi.org/10.1016/j.jngse.2022.104563>.
- Wang, E., Guo, T., Liu, B., Li, M., Xiong, L., Dong, X., Zhang, N., Wang, T., 2022. Lithofacies and pore features of marine-continental transitional shale and gas enrichment conditions of favorable lithofacies: A case study of Permian Longtan Formation in the Lintanchang area, southeast of Sichuan Basin, SW China. *Pet. Explor. Dev.* 49 (6), 1310–1322. [https://doi.org/10.1016/S1876-3804\(23\)60351-9](https://doi.org/10.1016/S1876-3804(23)60351-9).
- Wang, E., Li, C., Feng, Y., Song, Y., Guo, T., Li, M., Chen, Z., 2022e. Novel method for determining the oil moveable threshold and an innovative model for evaluating the oil content in shales. *Energy* 239, 121848. <https://doi.org/10.1016/j.energy.2021.121848>.
- Wang, H.J., Wu, W., Chen, T., Yu, J., Pan, J.N., 2019. Pore structure and fractal analysis of shale oil reservoirs: A case study of the Paleogene Shahejie Formation in the Dongying Depression, Bohai Bay, China. *J. Petrol. Sci. Eng.* 177, 711–723. <https://doi.org/10.1016/j.petrol.2019.02.081>.
- Wang, H.N., Wan, Y.Z., Li, J., Zhang, S.N., He, F., Huang, Y., Wang, Y.L., 2007. Research and development of nanofibrous scaffolds for tissue engineering and their nanoeffects. *Mater. Rep.* 21 (4), 13–16 (in Chinese with English Abstract).
- Wang, K., Taylor, K.G., Ma, L., 2021a. Advancing the application of atomic force microscopy (AFM) to the characterization and quantification of geological material properties. *Int. J. Coal Geol.* 247. <https://doi.org/10.1016/j.coal.2021.103852>.
- Wang, X.X., Hou, J.G., Li, S.H., Dou, L.X., Song, S.H., Kang, Q.Q., Wang, D.M., 2020. Insight into the nanoscale pore structure of organic-rich shales in the Bakken Formation, USA. *J. Pet. Sci. Eng.* 191. <https://doi.org/10.1016/j.petrol.2020.107182>.
- Wang, Y., Liu, L., Zheng, S., Luo, Z., Sheng, Y., Wang, X., 2019b. Full-scale pore structure and its controlling factors of the Wufeng-Longmaxi shale, southern Sichuan Basin, China: Implications for pore evolution of highly overmature marine shale. *J. Nat. Gas Sci. Eng.* 67, 134–146. <https://doi.org/10.1016/j.jngse.2019.04.020>.
- Wang, Y., Pu, J., Wang, L.H., Wang, J.Q., Jiang, Z., Song, Y.F., Wang, C.C., Wang, Y.F., Jin, C., 2016. Characterization of typical 3D pore networks of Jiulaodong formation shale using nano-transmission X-ray microscopy. *Fuel* 170, 84–91. <https://doi.org/10.1016/j.fuel.2015.11.086>.
- Wang, Y., Zhu, Y.M., Chen, S.B., Li, W., 2014. Characteristics of the Nanoscale Pore Structure in Northwestern Hunan Shale Gas Reservoirs using Field Emission Scanning Electron Microscopy, High-pressure Mercury Intrusion, and Gas Adsorption. *Energy* 78 (2), 945–955. <https://doi.org/10.1021/ef402159e>.
- Wang, Y.D., Blunt, M.J., Armstrong, R.T., Mostaghimi, P., 2021b. Deep learning in pore scale imaging and modeling. *Earth Sci. Rev.* 215. <https://doi.org/10.1016/j.earscirev.2021.103555>.
- Wang, Z.Z., Zhai, S.D., Zhou, L.F., Deng, M.Y., Wang, S.J., 2005. Application of nuclear magnetic resonance logging technology physical property analysis of rock. *Petrol. Geol. Exp.* 27 (6), 619–623 (in Chinese with English Abstract).
- Washburn, E.W., 1921. The dynamics of capillary flow. *Phys. Rev.* 17 (3), 273. <https://doi.org/10.1103/PhysRev.17.273>.
- Wei, M., Zhang, L., Xiong, Y., Li, J., Peng, P.A., 2016. Nanopore structure characterization for organic-rich shale using the non-local-density functional theory by a combination of N<sub>2</sub> and CO<sub>2</sub> adsorption. *Microporous Mesoporous Mater.* 227, 88–94. <https://doi.org/10.1016/j.micromeso.2016.02.050>.
- Wei, Z.F., Wang, Y.L., Wang, G., Sun, Z.P., Xu, L., 2018. Pore characterization of organic-rich late Permian Da-long Formation shale in the Sichuan Basin, southwestern China. *Fuel* 211, 507–516. <https://doi.org/10.1016/j.fuel.2017.09.068>.
- Xiao, L.Z., 1998. Nuclear Magnetic Resonance Imaging Logging and Rock Nuclear Magnetic Resonance and its Application. Science Press, Beijing (in Chinese).

- Xiao, L.Z., Chai, X.Y., Sun, B.X., Lu, D.W., Fu, Y.S., Gao, Q.T., 2001. Introduction to Nuclear Magnetic Resonance Logging Data Interpretation and Application. Petroleum Industry Press, Beijing (in Chinese).
- Xu, H., Zhou, W., Zhang, R., Liu, S., Zhou, Q., 2019. Characterizations of pore, mineral and petrographic properties of marine shale using multiple techniques and their implications on gas storage capability for Sichuan Longmaxi gas shale field in China. *Fuel* 241, 360–371. <https://doi.org/10.1016/j.fuel.2018.12.035>.
- Xu, Y., Li, X.S., 2003. Analysis of nano-micropore in carbon fiber by small angle X-ray scattering. *Phys. Test. Chem. Anal. (Part A Phys. Test)* 39 (1), 28–31 (in Chinese with English Abstract).
- Xue, C.Q., Wu, J.G., Qiu, L.W., Zhong, J.H., Zhang, S.R., Zhang, B., Wu, X., Hao, B., 2020. Lithofacies classification and its controls on the pore structure distribution in Permian transitional shale in the northeastern Ordos Basin, China. *J. Pet. Sci. Eng.* 195 <https://doi.org/10.1016/j.petrol.2020.107657>.
- Yan, X., Zhou, J.C., Deng, X.Y., 2008. Application of the four big effects of nano-CaCO<sub>3</sub>. *China Chem.* 4, 44–47 (in Chinese with English Abstract).
- Yang, C., Xiong, Y., Zhang, J., Liu, Y., Chen, C., 2019a. Comprehensive Understanding of OM-Hosted Pores in Transitional Shale: a Case Study of Permian Longtan Shale in South China based on Organic Petrographic Analysis, Gas Adsorption, and X-ray Diffraction Measurements. *Energ. Fuel* 33 (9), 8055–8064. <https://doi.org/10.1021/acs.energyfuels.9b01410>.
- Yang, C., Xiong, Y.Q., Zhang, J.C., 2020. A comprehensive re-understanding of the OM-hosted nanopores in the marine Wufeng-Longmaxi shale formation in South China by organic petrology, gas adsorption, and X-ray diffraction studies. *Int. J. Coal Geol.* 218 <https://doi.org/10.1016/j.coal.2019.103362>.
- Yang, C., Zhang, J.C., Tang, X., 2013. Microscopic pore types and its impact on the storage and permeability of continental shale gas, Ordos Basin. *Earth Sci. Front.* 20 (04), 240–250 (in Chinese with English Abstract).
- Yang, C., Zhang, J.C., Wang, X.Z., Tang, X., Chen, Y.C., Jiang, L.L., Gong, X., 2017. Nanoscale pore structure and fractal characteristics of a marine-continental transitional shale: A case study from the lower Permian Shanxi Shale in the southeastern Ordos Basin, China. *Mar. Pet. Geol.* 88, 54–68. <https://doi.org/10.1016/j.marpetgeo.2017.07.021>.
- Yang, F., Ning, Z., Wang, Q., Zhang, R., Krooss, B.M., 2016a. Pore structure characteristics of lower Silurian shales in the southern Sichuan Basin, China: Insights to pore development and gas storage mechanism. *Int. J. Coal Geol.* 156, 12–24. <https://doi.org/10.1016/j.coal.2015.12.015>.
- Yang, F., Ning, Z.F., Wang, Q., Liu, H.Q., 2016. Pore structure of Cambrian shales from the Sichuan Basin in China and implications to gas storage. *Mar. Pet. Geol.* 70, 14–26. <https://doi.org/10.1016/j.marpetgeo.2015.11.001>.
- Yang, F., Ning, Z.F., Wang, Q., Zhang, R., Krooss, B.M., 2016c. Pore structure characteristics of lower Silurian shales in the southern Sichuan Basin, China: Insights to pore development and gas storage mechanism. *Int. J. Coal Geol.* 156, 12–24. <https://doi.org/10.1016/j.coal.2015.12.015>.
- Yang, J.H., Li, Y., Wu, X., Wu, P., Han, W.L., Zhao, S.H., 2019b. Study on micro-scale mechanical properties of coal rock based on atomic force microscopy. *Coal Sci. Technol.* 47 (9) (in Chinese with English Abstract).
- Yang, R., Hao, F., He, S., He, C., Guo, X., Yi, J., Hu, H., Zhang, S., Hu, Q., 2017b. Experimental investigations on the geometry and connectivity of pore space in organic-rich Wufeng and Longmaxi shales. *Mar. Pet. Geol.* 84, 225–242. <https://doi.org/10.1016/j.marpetgeo.2017.03.033>.
- Yang, R., Jia, A.Q., He, S., Wang, T., Hu, Q.H., 2021. Pore Structure Characterization and Reservoir Quality Evaluation of Analcite-Rich Shale Oil Reservoir from the Bohai Bay Basin. *Energ. Fuel* 35 (11), 9349–9368. <https://doi.org/10.1021/acs.energyfuels.1c00811>.
- Yao, S., Jiao, K., Zhang, K., Hu, W., Ding, H., Li, M., Pei, W., 2011. An atomic force microscopy study of coal nanopore structure. *Chin. Sci. Bull.* 56 (25), 2706–2712.
- Yao, Y., Liu, D., 2012. Comparison of low-field NMR and mercury intrusion porosimetry in characterizing pore size distributions of coals. *Fuel* 95, 152–158. <https://doi.org/10.1016/j.fuel.2011.12.039>.
- Yao, Y., Liu, D., Che, Y., Tang, D., Tang, S., Huang, W., 2009. Non-destructive characterization of coal samples from China using microfocus X-ray computed tomography. *Int. J. Coal Geol.* 80 (2), 113–123. <https://doi.org/10.1016/j.coal.2009.08.001>.
- Yao, Y., Liu, D., Che, Y., Tang, D., Tang, S., Huang, W., 2010. Petrophysical characterization of coals by low-field nuclear magnetic resonance (NMR). *Fuel* 89 (7), 1371–1380. <https://doi.org/10.1016/j.fuel.2009.11.005>.
- Yin, H., Zhou, J.P., Jiang, Y.D., Xian, X.F., Liu, Q.L., 2016. Physical and structural changes in shale associated with supercritical CO<sub>2</sub> exposure. *Fuel* 184, 289–303. <https://doi.org/10.1016/j.fuel.2016.07.028>.
- Yu, Y.M., Hu, Y.Q., Liang, W.G., Meng, Q.R., Feng, Z.Z., 2012. Study on pore characteristics of lean coal at different temperature by CT technology. *Chin. J. Geophys.* 55 (02), 637–644 (in Chinese with English Abstract).
- Zhang, J.Z., Li, X.Q., Wei, Q., Gao, W.J., Liang, W.L., Wang, Z., Wang, F.Y., 2017. Quantitative characterization of pore-fracture system of organic-rich marine-continental shale reservoirs: A case study of the Upper Permian Longtan Formation, Southern Sichuan Basin, China. *Fuel* 200, 272–281. <https://doi.org/10.1016/j.fuel.2017.03.080>.
- Zhang, J.Z., Tang, Y.J., He, D.X., Sun, P., Zou, X.Y., 2020a. Full-scale nanopore system and fractal characteristics of clay-rich lacustrine shale combining FE-SEM, nano-CT, gas adsorption and mercury intrusion porosimetry. *Appl. Clay Sci.* 196 <https://doi.org/10.1016/j.clay.2020.105758>.
- Zhang, P.F., Lu, S.F., Li, J.Q., 2019. Characterization of pore size distributions of shale oil reservoirs: A case study from Dongying sag, Bohai Bay basin, China. *Mar. Pet. Geol.* 100, 297–308. <https://doi.org/10.1016/j.marpetgeo.2018.11.024>.
- Zhang, Y., Ju, B., Zhang, M., Wang, C., Zeng, F., Hu, R., Yang, L., 2022. The effect of salt precipitation on the petrophysical properties and the adsorption capacity of shale matrix based on the porous structure reconstruction. *Fuel* 310. <https://doi.org/10.1016/j.fuel.2021.122287>.
- Zhang, Y., Zhang, M., Mei, H., Zeng, F., 2019b. Study on salt precipitation induced by formation brine flow and its effect on a high-salinity tight gas reservoir. *J. Pet. Sci. Eng.* 183, 106384 <https://doi.org/10.1016/j.petrol.2019.106384>.
- Zhang, Y.R., Meng, Y.G., 2006. Direct simulation Monte Carlo method on nanoscale effect of gas mean free path. *Lubr. Eng.* 7, 5–7 (in Chinese with English Abstract).
- Zhang, Y.X., Barber, T.J., Hu, Q.H., Bleuel, M., El-Sobky, H.F., 2019c. Complementary neutron scattering, mercury intrusion and SEM imaging approaches to micro- and nano-pore structure characterization of tight rocks: a case study of the Bakken shale. *Int. J. Coal Geol.* 212 <https://doi.org/10.1016/j.coal.2019.103252>.
- Zhang, Y.X., Hu, Q.H., Barber, T.J., Bleuel, M., Anovitz, L.M., Littrell, K., 2020b. Quantifying Fluid-Wettable Effective Pore Space in the Utica and Bakken Oil Shale Formations. *Geophys. Res. Lett.* 47 (14) <https://doi.org/10.1029/2020GL087896>.
- Zhang, Z., Yang, Z., 2013. Theoretical and practical discussion of measurement accuracy for physisorption with micro- and mesoporous materials. *Chin. J. Catal.* 34 (10), 1797–1810. [https://doi.org/10.1016/S1872-2067\(12\)60601-9](https://doi.org/10.1016/S1872-2067(12)60601-9).
- Zhao, J., Jin, Z., Hu, Q., Jin, Z., Barber, T.J., Zhang, Y., Bleuel, M., 2017. Integrating SANS and fluid-invasion methods to characterize pore structure of typical american shale oil reservoirs. *Sci. Rep.* 7 (1), 15413. <https://doi.org/10.1038/s41598-017-15362-0>.
- Zhao, S.H., Li, Y., Wang, Y.B., Ma, Z.T., Huang, X.Q., 2019. Quantitative study on coal and shale pore structure and surface roughness based on atomic force microscopy and image processing. *Fuel* 244, 78–90. <https://doi.org/10.1016/j.fuel.2019.02.001>.
- Zheng, Y.J., Liao, Y.H., Wang, Y.P., Xiong, Y.Q., Peng, P.A., 2018. Organic geochemical characteristics, mineralogy, petrophysical properties, and shale gas prospects of the Wufeng-Longmaxi shales in Sanquan Town of the Nanchuan District, Chongqing. *AAPG Bull.* 102 (11), 2239–2265. <https://doi.org/10.1306/04241817065>.
- Zhou, J.P., Yang, K., Tian, S.F., Zhou, L., Xian, X.F., Jiang, Y.D., Liu, M.H., Cai, J.C., 2020a. CO<sub>2</sub>-water-shale interaction induced shale microstructural alteration. *Fuel* 263. <https://doi.org/10.1016/j.fuel.2019.116642>.
- Zhou, S.D., Yan, D.T., Tang, J.G., Pan, Z.J., 2020b. Abrupt change of pore system in lacustrine shales at oil- and gas-maturity during catagenesis. *Int. J. Coal Geol.* 228 <https://doi.org/10.1016/j.coal.2020.103557>.
- Zhou, X., Wen, H., Zhang, Y., Xu, J., Zhang, W., 2021. Landslide susceptibility mapping using hybrid random forest with GeoDetector and RFE for factor optimization. *Geosci. Front.* 12 (5), 101211 <https://doi.org/10.1016/j.gsf.2021.101211>.
- Zhu, R.K., Bai, B., Cui, J.W., Wu, S.T., Cui, J.G., Wang, T., Niu, L., Li, T.T., 2013. Research advances of microstructure in unconventional tight oil and gas reservoirs. *J. Palaeogeogr. (Chin. Ed.)* 15 (5), 615–623 (in Chinese with English Abstract).
- Zhu, R.K., Wu, S.T., Su, L., Cui, J.W., Mao, Z.G., Zhang, X.X., 2016a. Problems and future works of porous texture characterization of tight reservoirs in China. *Acta Pet. Sin.* 37 (11), 1323 (in Chinese with English Abstract).
- Zhu, X., Cai, J., Wang, G., Song, M., 2018. Role of organo-clay composites in hydrocarbon generation of shale. *Int. J. Coal Geol.* 192, 83–90. <https://doi.org/10.1016/j.coal.2018.04.002>.
- Zhu, Y.M., Wang, Y., Chen, S.B., Zhang, H., Fu, C.Q., 2016b. Qualitative quantitative multiscale characterization of pore structures in shales reservoirs: a case study of Longmaxi Formation in the Upper Yangtze area. *Earth Sci. Front.* 23 (1), 154–163 (in Chinese with English Abstract).
- Zhu, Y.P., 2008. Small angle X-ray scattering, 140. Chemical Industry Press, Beijing (in Chinese).
- Zou, C.N., Zhu, R.K., Wu, S.T., Yang, Z., Tao, S.Z., Yuan, X.J., Hou, L.H., Yang, H., Xu, C., Li, D.H., Bai, B., Wang, L., 2012. Types, characteristics, genesis and prospects of conventional and unconventional hydrocarbon accumulations: taking tight oil and tight gas in China as an instance. *Acta Pet. Sin.* 33 (02), 173–187 (in Chinese with English Abstract).